

DISSERTATION

IMAGING SINGLE BARIUM ATOMS IN SOLID XENON FOR BARIUM TAGGING IN THE  
NEXO NEUTRINOLESS DOUBLE BETA DECAY EXPERIMENT

Submitted by

Timothy Walton

Department of Physics

In partial fulfillment of the requirements

For the Degree of Doctor of Philosophy

Colorado State University

Fort Collins, Colorado

Fall 2016

Doctoral Committee:

Advisor: William M. Fairbank, Jr.

Bruce Berger  
Alan Van Orden  
Robert Wilson

Copyright by Timothy Walton 2016

All Rights Reserved

## ABSTRACT

The nEXO experiment will search for neutrinoless double beta decay of the isotope  $^{136}\text{Xe}$  in a ton-scale liquid xenon time projection chamber, in order to probe the Majorana nature of neutrinos. Detecting the daughter  $^{136}\text{Ba}$  of double beta decay events, called barium tagging, is a technique under investigation which would provide a veto for a background-free measurement. This would involve detecting a single barium ion from within a macroscopic volume of liquid xenon. One proposed barium tagging method is to trap the barium ion in solid xenon at the end of a cold probe, and then detect it by its fluorescence in the solid xenon. In this thesis, new studies on the spectroscopy of deposits of Ba and  $\text{Ba}^+$  in solid xenon are presented. Imaging of barium atoms in solid xenon is demonstrated with sensitivity down to the single atom level. Achievement of this level of sensitivity is a major step toward barium tagging by this method.

## ACKNOWLEDGEMENTS

I thank my adviser William M. Fairbank, Jr. with inadequate words for his inspiring courage, foresight, and intuition as a physicist. The success of this thesis, those to come, and of the experimental method which they work toward belongs foremost to him. Special thanks also to Chris Chambers for tireless help with experiment and analysis, and ambition to continue the work. I thank him and Adam Craycraft for companionship and intellectual input. I thank Shon Cook and Brian Mong for developing the apparatus, pioneering the work, and training me. Thanks to Cesar Benitez and Kendy Hall for training as well. I also thank the nEXO collaboration for their support, and especially their spokesman Giorgio Gratta. I thank my wife for supporting and enduring the physicist lifestyle, and everyone in my family for inspiration and vital support.

This dissertation is typset in L<sup>A</sup>T<sub>E</sub>X using a document class designed by Leif Anderson.

Dedicated to my new son Logan.

## TABLE OF CONTENTS

Abstract .....	ii
Acknowledgements .....	iii
Chapter 1. Introduction .....	1
1.1. Neutrinos .....	2
1.2. Double Beta Decay .....	6
1.3. Enriched Xenon Observatory .....	9
Chapter 2. Theory .....	21
2.1. Ba/Ba <sup>+</sup> Spectroscopy in Vacuum .....	21
2.2. 5-level Rate Equations Model .....	24
2.3. Matrix Isolation Spectroscopy .....	27
2.4. Fluorescence Efficiency .....	30
Chapter 3. Experimental .....	32
3.1. Ion Beam System .....	32
3.2. Ba Getter Source .....	41
3.3. Sample Deposition .....	42
3.4. Laser Excitation .....	44
3.5. Collection Optics .....	48
3.6. Wavelength Calibration .....	50
3.7. Vibrations and Effective Laser Region .....	51
Chapter 4. Method .....	54
4.1. Fitting of Spectra .....	54

4.2. Background Spectra .....	58
Chapter 5. Results: Spectroscopy .....	63
5.1. Excitation and Emission of Ba in SXe.....	63
5.2. 619-nm Peak Assignment .....	66
5.3. Annealing/Temperature Dependence .....	67
5.4. Bleaching .....	71
5.5. Blue Excitation / Candidate Ba <sup>+</sup> Lines .....	77
Chapter 6. Results: Imaging .....	80
6.1. Imaging 577- and 591-nm Fluorescence.....	80
6.2. Imaging 619-nm Fluorescence .....	81
Chapter 7. Conclusions .....	87
7.1. Future Work .....	87
Bibliography .....	90

## CHAPTER 1

### INTRODUCTION

Neutrinos are elusive fundamental particles of great importance in the continuing study of particle physics. Though extremely difficult to study, with tiny yet non-zero masses, no electric charge, and low interaction cross-sections, neutrinos have provided great insight into nuclear physics, geophysics, and astrophysics, and may provide the key to understanding the matter/anti-matter asymmetry of the universe. Neutrinos were first predicted by W. Pauli in 1930. He proposed the existence of a neutral, unobserved particle to explain the apparent violation of energy conservation in beta decay [1]. He admitted that neutrinos (then deemed “neutrons” – what we now know as neutrons had not been discovered yet either) should be difficult to observe experimentally, but also that it seemed unlikely that they would never have been noticed before. As it turns out, they are much more difficult to observe than he predicted. Their probabilities for interaction are extremely small.

A theory formulated in 1933 by E. Fermi for beta decay [2], including the neutrino, was the beginning of weak interaction theory. Eventually, progress led to a unified treatment of electromagnetic, weak and strong forces and the development of the very successful Standard Model (SM) of particle physics. In the SM, neutrinos are massless. The discovery of non-zero neutrino mass via neutrino oscillations in the late 1990s [3] shows that there is more new physics to be discovered beyond the SM, and presents a path to follow.

The See-Saw Mechanism is a theory which explains the extreme lightness of neutrinos compared to other particles, while also predicting very heavy neutrino partners. The existence of heavy neutrinos in the high-energy environment of the early universe, coupled with

the possibility of the violation of CP conservation in decays of these heavy neutrinos, could explain why the universe became dominated by matter [4].

If neutrinos are Majorana particles rather than Dirac particles, the process of neutrinoless double beta decay ( $0\nu\beta\beta$ ) is allowed if the neutrino mass is non-zero. Observation of  $0\nu\beta\beta$  would simultaneously demonstrate that neutrinos are Majorana particles, as well as aid in determining the absolute mass itself [5]. This chapter outlines the current theory for neutrinos, and then describes the  $0\nu\beta\beta$  experiments EXO-200 and nEXO, in order to motivate barium tagging for nEXO.

## 1.1. NEUTRINOS

Neutrinos are chargeless leptons which only interact via the weak force (and gravity). There are three known “flavors” of neutrinos,  $\nu_e$ ,  $\nu_\mu$ , and  $\nu_\tau$ , each corresponding to one of the three known leptons. These are the eigenstates in the basis of the weak force, so they are the states in which a neutrino will interact via the weak force.

### 1.1.1. NEUTRINO OSCILLATION AND MASS

If neutrinos have a mass basis which is different from the flavor basis, the phenomenon of flavor oscillation may occur. Neutrinos, which are produced as pure flavor states, will exhibit a time-dependent oscillation in the probability of measuring the other flavors as well, if the three neutrino masses are different.

The very small mass of a neutrino relative to its momentum lets one write the relativistic Hamiltonian in terms of mass squared differences  $\Delta m_{ij}^2 = m_i^2 - m_j^2$ , where  $i,j = 1,2,3$ , referring to the three mass states. The mixing between the 3-vector mass and flavor bases is defined by a rotation in terms of three mixing angles,  $\theta_{12}$ ,  $\theta_{23}$ , and  $\theta_{13}$ . Transformation

between the flavor and mass bases is done with the following unitary matrix, called the Pontecorvo–Maki–Nakagawa–Sakata (PMNS) matrix [6]:

$$\begin{aligned}
(1) \quad U &= \begin{pmatrix} 1 & 0 & 0 \\ 0 & c_{23} & s_{23} \\ 0 & -s_{23} & c_{23} \end{pmatrix} \begin{pmatrix} c_{13} & 0 & s_{13}e^{-i\delta} \\ 0 & 1 & 0 \\ -s_{13}e^{i\delta} & 0 & c_{13} \end{pmatrix} \begin{pmatrix} c_{12} & s_{12} & 0 \\ -s_{12} & c_{12} & 0 \\ 0 & 0 & 1 \end{pmatrix} \begin{pmatrix} 1 & 0 & 0 \\ 0 & e^{i\alpha_1/2} & 0 \\ 0 & 0 & e^{i\alpha_2/2} \end{pmatrix} \\
&= \begin{pmatrix} c_{12}c_{13} & s_{12}c_{13} & s_{13}e^{-i\delta} \\ -s_{12}c_{23} - c_{12}s_{23}s_{13}e^{i\delta} & c_{12}c_{23} - s_{12}s_{23}s_{13}e^{i\delta} & s_{23}c_{13} \\ s_{12}s_{23} - c_{12}c_{23}s_{13}e^{i\delta} & -c_{12}s_{23} - s_{12}c_{23}s_{13}e^{i\delta} & c_{23}c_{13} \end{pmatrix} \begin{pmatrix} 1 & 0 & 0 \\ 0 & e^{i\alpha_1/2} & 0 \\ 0 & 0 & e^{i\alpha_2/2} \end{pmatrix}
\end{aligned}$$

where  $c_{ij} = \cos \theta_{ij}$  and  $s_{ij} = \sin \theta_{ij}$ .  $\delta$  and  $\alpha_i$  are Dirac and Majorana CP-violating phases, respectively. Transformation between bases is done by Eq. 2:

$$\begin{aligned}
(2) \quad |\nu_\alpha\rangle &= \sum_i U_{\alpha i}^* |\nu_i\rangle, \\
|\nu_i\rangle &= \sum_\alpha U_{\alpha i} |\nu_\alpha\rangle.
\end{aligned}$$

A two-neutrino approximation demonstrates how this results in neutrino oscillation. In this case, there is only one mixing angle  $\theta$  and one mass squared difference  $\Delta$ , and the Hamiltonian  $H$  and mixing matrix  $U$  are as follows:

$$(3) \quad H = \frac{1}{4E} \begin{pmatrix} -\Delta & 0 \\ 0 & \Delta \end{pmatrix}$$

$$U = \begin{pmatrix} \cos \theta & \sin \theta \\ -\sin \theta & \cos \theta \end{pmatrix}.$$

Applying time evolution to a pure electron neutrino state (where the two neutrino flavors here are  $\nu_e$  and  $\nu_\mu$ ) then leads to the following time-dependent state:

$$(4) \quad |\nu(t)\rangle = (e^{it\Delta/4E} \cos^2 \theta + e^{-it\Delta/4E} \sin^2 \theta) |\nu_e\rangle$$

$$+ \cos \theta \sin \theta (-e^{it\Delta/4E} + e^{-it\Delta/4E}) |\nu_\mu\rangle$$

where  $E$  is the neutrino energy. Note that if  $\theta$  is zero, the case where the mass basis is the same as the flavor basis, the state remains pure  $|\nu_e\rangle$ . The same is true if  $\Delta$  is zero. Thus, the discovery of neutrino oscillation was the first (and only, so far) demonstration that neutrinos have a non-zero mass.

Studying oscillations of neutrinos from different kinds of sources, with different energies and path lengths, can isolate sensitivities to the different mixing angles and mass squared differences. For example, the study of solar neutrinos (neutrinos emanating from nuclear fusion reactions in the core of the sun) provides sensitivity to  $\theta_{12}$  and  $\Delta m_{21}^2$ . The oscillation parameters so far measured are shown in Table 1.1.

Since only the absolute value of the atmospheric neutrino oscillation parameter  $\Delta m^2$  is known, there are two possibilities for the hierarchy of the three neutrino masses. These are

TABLE 1.1. Best-fit values for neutrino oscillation parameters, from a global fit to oscillation experiment data. Parameters which depend on the mass hierarchy have separate values for NH (IH). The atmospheric parameter  $\Delta m^2$  is defined as  $\Delta m^2 = \Delta m_{31}^2 - \Delta m_{21}^2/2 > 0$  ( $\Delta m^2 = \Delta m_{31}^2 + \Delta m_{21}^2/2 < 0$ ). [6]

Parameter	Measurement ( $\pm 1\sigma$ )
$\Delta m_{21}^2$	$7.54^{+0.26}_{-0.22} 10^{-5} \text{ eV}^2$
$ \Delta m^2 $	$2.43 \pm 0.06$ ( $2.38 \pm 0.06$ ) $10^{-3} \text{ eV}^2$
$\sin^2 \theta_{12}$	$0.308 \pm 0.017$
$\sin^2 \theta_{23}$	$0.437^{+0.033}_{-0.023}$ ( $0.455^{+0.039}_{-0.031}$ )
$\sin^2 \theta_{13}$	$0.0234^{+0.0020}_{-0.0019}$ ( $0.0240^{+0.0019}_{-0.0022}$ )
$\delta/\pi$ ( $2\sigma$ range)	$1.39^{+0.38}_{-0.27}$ ( $1.31^{+0.29}_{-0.33}$ )



FIGURE 1.1. The two possible hierarchies of neutrino masses. The colors depict the mixing between the mass and flavor bases.

called the Normal Hierarchy (NH) and Inverted Hierarchy (IH), as shown in Fig. 1.1. The actual mass hierarchy remains unknown, but next-generation neutrino experiments, possibly including nEXO, may be able to discern this.

Neutrino oscillation demonstrates that neutrinos have non-zero mass, and though oscillation experiments measure the mass squared differences, the absolute masses of the three neutrinos remain unknown. Cosmology puts limits on the sum of the three neutrino masses. The Planck collaboration reports an upper bound on this sum at  $\sum_i m_i < 0.23 \text{ eV}$  [7]. The



FIGURE 1.2. Two-neutrino (left) and neutrinoless (right) double beta decay.

KATRIN experiment is expected to have a sensitivity of  $m_{\bar{\nu}_e} < 0.2$  eV (90% CL) for absolute neutrino mass from a careful measurement of tritium beta decay very near the maximal decay energy (Q-value) [8].

## 1.2. DOUBLE BETA DECAY

Double beta decay is the simultaneous decay of two neutrons in a nucleus into two protons and two electrons. It is observable in even-even nuclei only if beta decay is energetically forbidden or highly suppressed. Two-neutrino double beta decay ( $2\nu\beta\beta$ ), shown in Fig. 1.2(left), is allowed by the Standard Model and has been observed in about a dozen isotopes with half-lives around  $10^{19}$ - $10^{21}$  years. Similar to beta decay, an anti-neutrino accompanies each electron in this decay, broadening the spectrum of the summed electron energy. This is a second-order process, and very rare, requiring low background to measure.

Neutrinoless double beta decay, shown in Fig. 1.2(right), is a postulated and yet unobserved mode of double beta decay. In this case, the neutrino is exchanged as a virtual particle (which would require that it is its own anti-particle, i.e. a Majorana particle), and



FIGURE 1.3. Majorana neutrino mass (including  $2\sigma$  uncertainty on neutrino oscillation parameters) vs. the minimum of the three neutrino masses. Red regions correspond to at least one of the Majorana phases ( $\alpha_1, \alpha_2$ ) having a CP-violating value, while blue and green regions correspond to CP-conserving Majorana phases. [6]

there are no neutrinos in the final products. If discovered, neutrinos would be determined to be Majorana particles. The decay would also demonstrate violation of lepton number conservation, as the final and initial states have lepton numbers of 2 and 0, respectively. The measured  $0\nu\beta\beta$  half-life would also aid in determining absolute neutrino mass according to Eq. 5:

$$(5) \quad T_{1/2}^{0\nu} = (G^{0\nu}(Q, Z)|M^{0\nu}|^2 \langle m_\nu \rangle^2)^{-1}$$

where  $T_{1/2}^{0\nu}$  is the  $0\nu\beta\beta$  half-life,  $G^{0\nu}$  is a known phase space factor, and  $M^{0\nu}$  is a model-dependent nuclear matrix element.  $\langle m_\nu \rangle$  is the effective Majorana neutrino mass:

$$(6) \quad \langle m_\nu \rangle = \sum_i U_{ei}^2 m_i.$$

The terms  $U_{ei}$  contain the measured mixing angles  $\theta_{12}$  and  $\theta_{13}$ , as well as the unknown CP-violating phases  $\delta$ ,  $\alpha_1$ , and  $\alpha_2$ . The effective Majorana mass is plotted vs. the minimum of the three neutrino mass eigenvalues in Fig. 1.3 [6]. The region above  $\langle m_\nu \rangle \approx 0.1$  eV, where the NH and IH overlap, is referred to as the quasi-degenerate (QD) region. If  $\langle m_\nu \rangle$  lies below the QD region, its measurement could also determine the correct neutrino mass hierarchy.

The sum of the energies of the emitted electrons in double beta decay will serve as the distinction between the two-neutrino and zero-neutrino modes, shown in Fig. 1.4. In the two-neutrino mode, the total decay energy is shared probabilistically between the electrons and the neutrinos (the nuclear recoil energy is negligible), resulting in a broad distribution in the summed electron energy. (Recall the similarly broad electron energy in single beta decay, which ultimately led to discovery of the neutrino involved.) But in the zero-neutrino mode, essentially all of the decay energy is carried away by the two electrons, resulting in effectively a single allowed value for the total electron energy – a peak in the summed electron energy spectrum at the Q-value.

The rarity of double beta decay requires very low backgrounds, especially around the Q-value for the  $0\nu\beta\beta$  search. The next sections describe the experiments EXO-200 and its next-generation successor, nEXO, and how the barium tagging method studied in this work could be critical in obtaining essentially zero background in the second phase of nEXO operation.



FIGURE 1.4. Conceptual two-neutrino (blue) and zero-neutrino (red) double beta decay spectra.

### 1.3. ENRICHED XENON OBSERVATORY

EXO-200 and nEXO (EXO standing for Enriched Xenon Observatory) are a progression of two experiments, each a liquid xenon (LXe) time projection chamber (TPC) designed to study the double beta decay of the isotope  $^{136}\text{Xe}$ , and ultimately to search for the zero-neutrino mode.  $^{136}\text{Xe}$  is unique among the double beta decay isotopes in that it can be studied in a gas or liquid TPC instead of solid crystals, foils, or liquid scintillators. The 3D event position reconstruction abilities of a TPC have advantages in background reduction, as described in section 1.3.1. Purification of Xe is straightforward and can be done continuously in the detector. LXe is transparent, and produces substantial ionization and scintillation at 178 nm when energy is deposited in the LXe [9]. Xe is easy to isotopically enrich in centrifuges. A liquid TPC approach also offers the opportunity to identify, or “tag”, the daughter  $^{136}\text{Ba}^{++}$  ion at the site of the double beta decay event, which would provide a method for background-free identification of  $0\nu\beta\beta$  [10]. Barium tagging is the focus of our group at CSU and is the subject of this thesis. The following sections describe the EXO-200 experiment, as well as nEXO, the next-generation tonne-scale LXe TPC, which is now in the



FIGURE 1.5. Drawing of the EXO-200 TPC Vessel with the surrounding cryostat, lead walls, and muon veto panels.

research and development stage. EXO-200 does not have barium tagging implemented, but it is hoped that nEXO will incorporate barium tagging in the second phase of operation.

### 1.3.1. EXO-200

Located about half a mile underground in the Waste Isolation Pilot Plant (WIPP) near Carlsbad, NM, EXO-200 has been operational since 2011. It is a TPC containing around 170 kg of LXe enriched to  $80.672 \pm 0.14\%$   $^{136}\text{Xe}$  [9]. It is designed to probe Majorana neutrino masses down to around 100 meV [11]. The WIPP mine is in a salt basin, which contains lower levels of Uranium and Thorium than rock in a typical mine.

A schematic diagram of the TPC in the class 100 cleanroom is shown in Fig. 1.5. Several layers of lead wall surround the copper cryostat, which is filled with HFE-7000, a cryogenic



FIGURE 1.6. EXO-200 TPC cutaway view [9].

fluid which keeps the TPC cooled to LXe temperatures. The HFE also provides shielding for the detector. The TPC vessel is made of low-radioactivity copper, and is kept as thin as possible to minimize backgrounds. Scintillating panels on the outside of the cleanroom provide a cosmic ray muon veto.

A cut-away view of the EXO-200 detector is shown in Fig. 1.6. It is two mirrored TPCs which share a cathode. The detection planes are a combination of ionized charge



FIGURE 1.7. View of the detection plane in one of the two EXO-200 TPCs.

induction/collection wires and large area avalanche photodiodes (LAAPDs), which detect scintillation light [12].

A view into one of the TPCs is shown in Fig. 1.7. On the detection plane, holes for the LAAPDs can be seen below the cross-hatched u- and v-wires. The white material on the inner wall is the Teflon reflector. When a double beta decay event occurs in the LXe, the energetic electrons ionize many surrounding Xe atoms, and also produce a scintillation signal.

The cathode is set to -8 kV, providing an electric field of 374 V/cm across the 19.2 cm drift length of each TPC. The drift velocity for electrons is  $1.71 \text{ mm}/\mu\text{s}$ , while ions will drift at  $\sim 1\text{-}2 \text{ mm}/\text{s}$  [13]. Ionized electrons drift from the decay site, first passing the v-wires, which receive an induction signal as depicted in Fig. 1.8, and are then collected by the



FIGURE 1.8. EXO-200 event topology. [11]

u-wires, which are set at a  $60^\circ$  angle from the v-wires. An electric field of 778 V/cm between the u- and v-wires ensures 100% v-wire transparency. The charge collection provides an energy measurement. Together, the u- and v-wires give an x/y position measurement for the event. The time between the initial scintillation detection and the charge collection gives a z position. Thus a 3D position can be reconstructed for the event if u-wire, v-wire, and scintillation signals are detected [9].

Due to variable recombination of ionized electrons, ionization and scintillation signals of individual events in LXe are anti-correlated [14]. This anti-correlation is exploited in EXO-200 to improve the energy resolution. Energies measured by ionization and scintillation of events produced by the  $^{228}\text{Th}$  gamma source, one of the sources used to calibrate the EXO-200 detector, are plotted in Fig. 1.9. The tilt of the full absorption ellipse of the 2615 keV gamma line demonstrates the anti-correlation. A “rotated energy” is defined according to this tilt in order to optimize energy resolution.

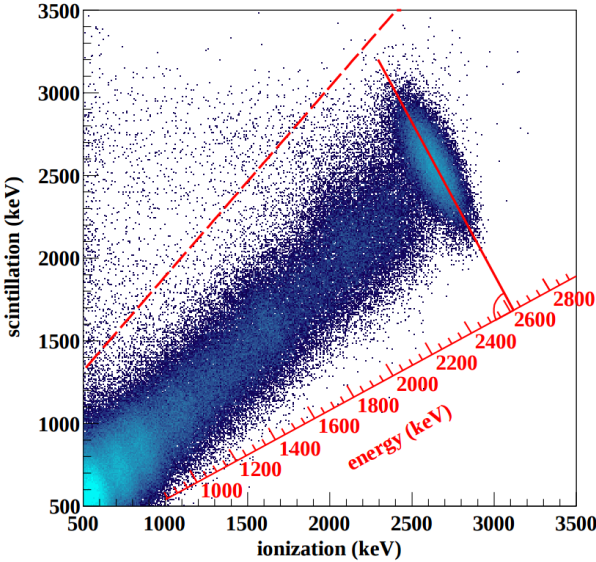


FIGURE 1.9. Anti-correlation between ionization and scintillation in events from the  $^{228}\text{Th}$  calibration source in EXO-200. The dashed red line defines a cut on non-reconstructed events. [15]

Having a reconstructed 3D event position is important in several ways. First, position-based corrections to scintillation and charge collection can be applied. For charge, electronegative impurities in the LXe will absorb the drifting charge, requiring a drift-length (z-position) correction. High purity levels, measured in terms of electron lifetime, of 2-5 ms and higher are maintained in EXO-200, resulting in a correction of a few percent for maximal drift lengths. For scintillation, a 3D correction is applied, as some regions have more efficient light collection by the LAPPDs. A 3D position also allows a fiducial volume to be defined. A standoff distance from detector surfaces aids in distinction between gamma ray events and double beta decay events. Gamma backgrounds, which mostly come from detector materials, exhibit some attenuation in the LXe volume. Double beta decay events are uniformly distributed in the LXe. Finally, 3D reconstruction allows the distinction between single-site (SS) and multi-site (MS) events. A MS event is one where two spatially separated events occur in the same 2048- $\mu\text{s}$  time window. These are mostly caused by gamma events,

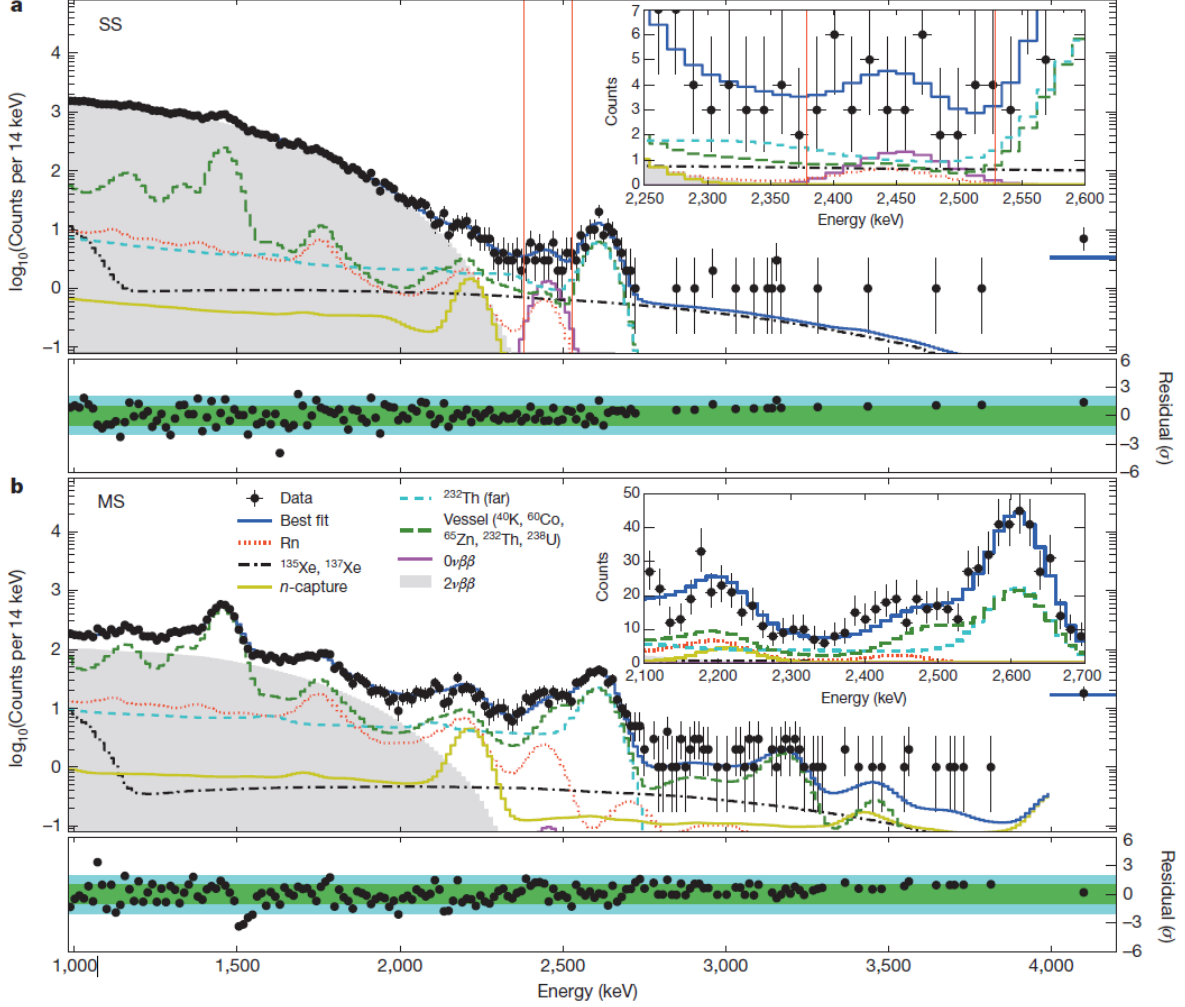


FIGURE 1.10. EXO-200 energy spectrum of (a) single-site, and (b) multi-site events from the latest  $0\nu\beta\beta$  search analysis. The insets show a zoom into the region of interest around the  $2\nu\beta\beta$  end point. [16]

which can Compton-scatter one or more times in the LXe. Rejecting MS events further aids in separating gamma events from double beta decay events [9]. Barium tagging will also benefit from a 3D reconstructed event position in nEXO.

The final data set is fit using a combination of probability distribution functions (PDFs) for  $0\nu\beta\beta$ ,  $2\nu\beta\beta$ , and background components. Fits to the final energy spectrum data for (a) SS events, and (b) MS events are shown in Fig. 1.10 for the most recent  $0\nu\beta\beta$  analysis from 2014. The green bands beneath each plot show the residuals vs. energy. The  $2\nu\beta\beta$

spectrum, in gray, dominates the signal in the SS spectrum below the Q-value. The vertical red lines in the SS spectrum outline the  $\pm 2\sigma$  region of interest around the Q-value, where the  $0\nu\beta\beta$  peak will lie. The insets are a zoom into this region. The best fit value for  $0\nu\beta\beta$  in this dataset is non-zero, but it is consistent with the null hypothesis at  $1.2\sigma$ . This data set reaches a half-life sensitivity of  $1.9 \times 10^{25}$  yr, and sets an upper limit on the  $0\nu\beta\beta$  half-life at  $T_{1/2}^{0\nu\beta\beta} > 1.1 \times 10^{25}$  yr (90% CL), which corresponds to  $\langle m_{\nu_e} \rangle < 190\text{-}450$  meV depending on nuclear matrix element calculations [16]. The half-life sensitivity and limit reported by the KamLAND-ZEN experiment are  $1.0 \times 10^{25}$  yr and  $T_{1/2}^{0\nu\beta\beta} > 1.9 \times 10^{25}$  yr (90% CL), respectively [17]. The  $2\nu\beta\beta$  half-life has also been measured in EXO-200 as  $T_{1/2}^{2\nu\beta\beta} = 2.165 \pm 0.016(\text{stat}) \pm 0.059(\text{sys}) \times 10^{21}$  yr [9]. This is the most precise  $2\nu\beta\beta$  measurement to date and is consistent with previous measurements by EXO-200 in 2011 [18] and KamLAND-ZEN in 2012 [19].

### 1.3.2. nEXO

The next-generation successor to EXO-200 is nEXO, a  $\sim 5$  ton LXe TPC which will probe Majorana neutrino masses down to the 10 meV scale. A schematic diagram of the nEXO detector in the SNOLAB cryopit, one of the possible locations for nEXO, is shown in Fig. 1.11. Similar to EXO-200, the copper-housed TPC will be submerged in HFE fluid, inside a copper cryostat. The cryostat will be insulated and submerged in a large volume of water shielding, in which photo-multiplier tubes will provide a muon veto by observing Cherenkov radiation. nEXO will be a single TPC. Rather than wires, nEXO will use tile electrodes for charge readout, shown in Fig. 1.12. Silicon photo-multipliers on the sides of the detector will be used for light detection.



FIGURE 1.11. nEXO TPC in the SNOLAB cryopit, with a 6-foot person for scale.

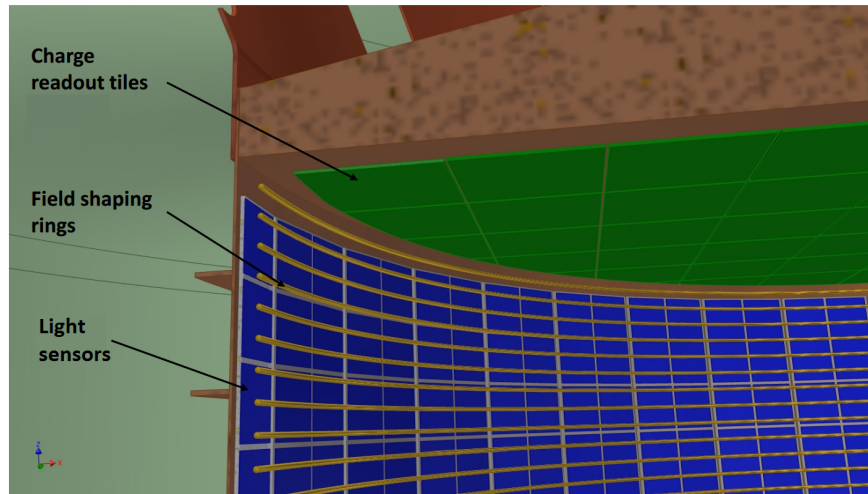


FIGURE 1.12. nEXO readout.



FIGURE 1.13. Projected nEXO sensitivity to the effective Majorana neutrino mass, overlaid on  $\langle m_\nu \rangle$  vs. the minimum of the three neutrino masses for both NH and IH. The solid lines enclose the 90% confidence region for the neutrino oscillation measurements, and the dotted lines allow for uncertainty on the CP-violating phases.

The sensitivity projections for nEXO are shown in Fig. 1.13, along with those of EXO-200. EXO-200 probes the QD region down to about 0.1 eV. nEXO will reach the non-degenerate region where the two possible mass hierarchies split, and will probe the full inverted hierarchy. The addition of barium tagging would be a very significant advance, as it would push the mass sensitivity down into the region allowed only by the NH.

### 1.3.3. BARIUM TAGGING

The ability to observe the daughter of each  $0\nu\beta\beta$  event is the ultimate background rejection technique. No background events generate a Ba daughter except  $2\nu\beta\beta$  of  $^{136}\text{Xe}$  [10]. Several possible barium tagging techniques have been proposed for nEXO. The original and most natural concept is to direct one or more lasers at the decay site to induce fluorescence

of the barium daughter. This technique was explored by our group, and has been abandoned for now because  $\text{Ba}^+$  fluorescence was not unambiguously identified in LXe [20].

A few barium tagging techniques continue to be explored. One of these is to grab the daughter on a surface, brought to the decay site by a probe. It would then be moved to a location where it can be desorbed from that surface by an infrared laser, and subsequently resonantly ionized by two lasers in order to detect it by time-of-flight spectroscopy. The apparatus for the study of this method is described in [21], along with some initial results.

The other leading technique for barium tagging in LXe, now the focus of our group and the subject of this thesis, is barium tagging in solid xenon (SXe). In this method, a cold probe would be inserted to the site of the candidate  $0\nu\beta\beta$  event, and additional cooling would be applied to trap the Ba or  $\text{Ba}^+$  daughter in a small amount of SXe at the end of the probe. The single Ba/ $\text{Ba}^+$  would be observed by laser-induced fluorescence in the SXe, a technique more generally called matrix isolation spectroscopy.

A concept for a probe is shown in Fig. 1.14. The SXe layer is formed on a sapphire window at the end of the probe. Sapphire is a good candidate for a substrate because it has good thermal conductivity at low temperature and is highly transparent. An excitation laser may be brought into the probe through a fiber, and scanned across the sapphire to excite the Ba/ $\text{Ba}^+$  in the SXe. A return fiber could collect the laser reflection to measure the SXe thickness via interference fringes. The Ba/ $\text{Ba}^+$  fluorescence would then be collected by a lens/filter system and imaged onto a CCD. Additional components, not shown, would be required for cooling the sapphire, either by liquid He or by a Joule-Thompson nozzle.

Whether the daughter Ba will neutralize or remain ionized in SXe is not yet known. It is expected that a  $\text{Ba}^{++}$  daughter of  $0\nu\beta\beta$  will neutralize rapidly to  $\text{Ba}^+$  by charge transfer

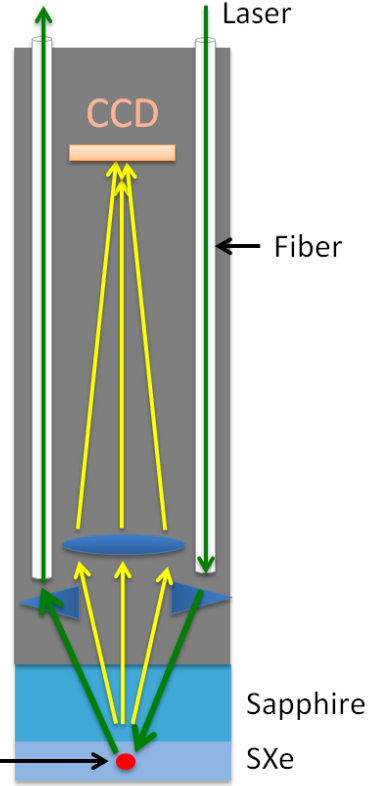


FIGURE 1.14. Concept for a cryoprobe for  $^{136}\text{Ba}^+$  daughter ion capture and detection in SXe, and a concept for internal collection optics.

in LXe, since the LXe conduction band gap is slightly less than the ionization potential for  $\text{Ba}^+$  [10]. Further neutralization by recombination with the electron cloud could also occur. However, a study of neutralization of  $^{214}\text{Bi}$  daughters of  $^{214}\text{Pb}$  beta decay in EXO-200 has observed a high percentage,  $76.4 \pm 5.7\%$ , of ionized daughters, and negligible subsequent neutralization in many minutes [13]. This provides an expectation of a high percentage of ionized  $^{136}\text{Ba}$  daughters of  $0\nu\beta\beta$  in LXe in the singly ionized state.

## CHAPTER 2

### THEORY

Theory relevant to the spectroscopy of single Ba atoms and Ba<sup>+</sup> ions in SXe matrices is discussed, beginning with the spectroscopy of Ba and Ba<sup>+</sup> in vacuum in Sec. 2.1, with a numerical solution to a 5-level rate equations model in Sec. 2.2. Matrix isolation spectroscopy of metal species in solid noble gas matrices is discussed in Sec. 2.3. Finally, fluorescence efficiency and cross section calculations are presented in Sec. 2.4.

TABLE 2.1. Transition rates for the lowest-lying energy levels of Ba and Ba<sup>+</sup> in vacuum.

	Transition	Rate ( $s^{-1}$ )	
Ba	$6s6p \ ^1P_1^o \rightarrow 6s^2 \ ^1S_0$	$1.19 \times 10^8$	[23]
	$6s6p \ ^1P_1^o \rightarrow 6s5d \ ^1D_2$	$2.50 \times 10^5$	[23]
	$6s6p \ ^1P_1^o \rightarrow 6s5d \ ^3D_2$	$1.1 \times 10^5$	[23]
	$6s6p \ ^1P_1^o \rightarrow 6s5d \ ^3D_1$	$3.1 \times 10^3$	[23]
	$6s5d \ ^1D_2 \rightarrow 6s^2 \ ^1S_0$	4	[24]
	$6s5d \ ^3D_2 \rightarrow 6s^2 \ ^1S_0$	$1.45^{-2}$	[25]
	$6s5d \ ^3D_1 \rightarrow 6s^2 \ ^1S_0$	$1.7^{-2}$	[24]
Ba <sup>+</sup>	$6p \ ^2P_{3/2}^o \rightarrow 6s \ ^2S_{1/2}$	$1.11 \times 10^8$	[23]
	$6p \ ^2P_{1/2}^o \rightarrow 6s \ ^2S_{1/2}$	$9.53 \times 10^7$	[23]
	$6p \ ^2P_{3/2}^o \rightarrow 5d \ ^2D_{5/2}$	$4.12 \times 10^7$	[23]
	$6p \ ^2P_{3/2}^o \rightarrow 5d \ ^2D_{3/2}$	$6.00 \times 10^6$	[23]
	$6p \ ^2P_{1/2}^o \rightarrow 5d \ ^2D_{3/2}$	$3.10 \times 10^7$	[23]
	$5d \ ^2D_{5/2} \rightarrow 6s \ ^2S_{1/2}$	$3.8 \times 10^{-2}$	[26]
	$5d \ ^2D_{3/2} \rightarrow 6s \ ^2S_{1/2}$	$1.3 \times 10^{-2}$	[27]

#### 2.1. BA/Ba<sup>+</sup> SPECTROSCOPY IN VACUUM

Some of the low-lying energy levels for Ba in vacuum are shown in Fig. 2.1. Transition rates for the lowest-lying Ba energy levels in vacuum are shown in Table 2.1. The main transition is between the ground  $6s^2 \ ^1S_0$  state to the excited  $6s6p \ ^1P_1^o$  state. Decays from the  $^1P_1^o$  state to three metastable D states have a branching ratio of about 1 in 330 excitations. Decays back to ground from the D states are parity-forbidden, resulting in very low decay

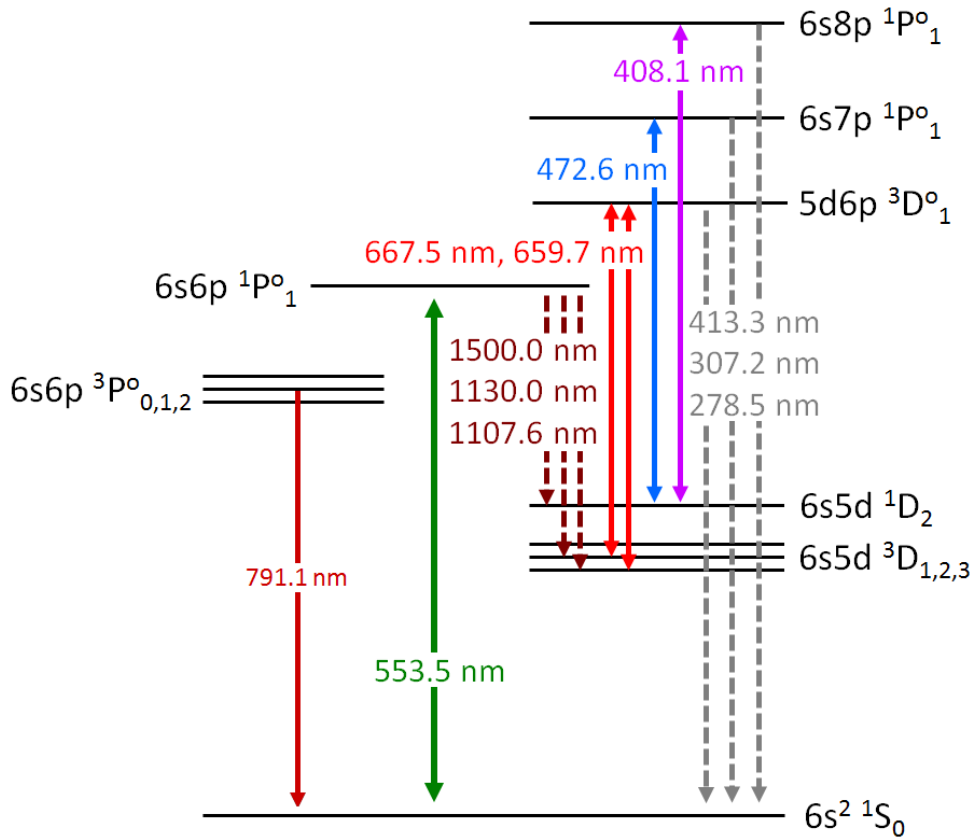


FIGURE 2.1. Ba energy levels in vacuum.

rates of around  $4 \text{ s}^{-1}$  for the  ${}^1\text{D}_2$  state, and around  $0.01 \text{ s}^{-1}$  for the  ${}^3\text{D}$  states. This can lead to significant optical pumping of these states during multiple cycles of excitation of the  ${}^1\text{S}_0 \rightarrow {}^1\text{P}_1^\circ$  transition.

The low-lying energy levels of  $\text{Ba}^+$  in vacuum are shown in Fig. 2.2. Two strong transitions exist between the ground  $6s \ ^2\text{S}_{1/2}$  state and the  $6p \ ^2\text{P}_{1/2}$  and  $6p \ ^2\text{P}_{3/2}$  excited states. Branching ratios to the two metastable  ${}^2\text{D}$  states result in a decay into a  ${}^2\text{D}$  state after about 4 excitations. Decay out of the  ${}^2\text{D}$  states takes tens of seconds. Transition rates between these levels are listed in Table 2.1.

Single atom/ion detection by fluorescence requires many excitation/emission cycles in order to detect an observable number of photons from a single atom/ion. For Ba and  $\text{Ba}^+$ ,

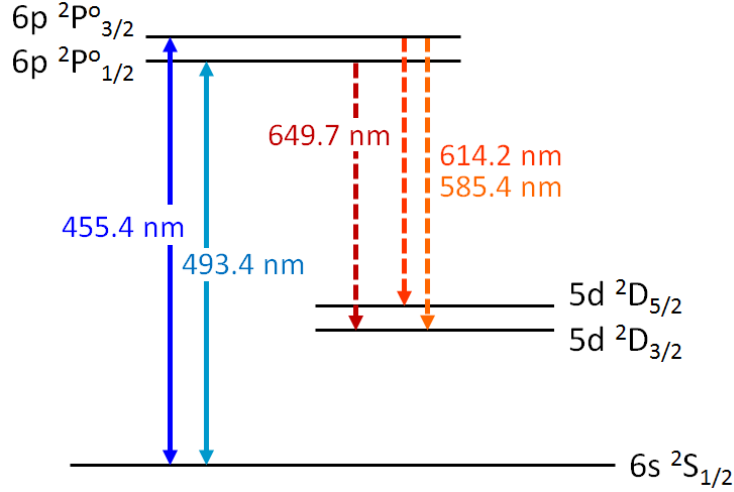


FIGURE 2.2.  $\text{Ba}^+$  energy levels in vacuum.

in addition to the main excitation laser, lasers may be needed to depopulate the metastable D states once the atom/ion becomes optically pumped into one of them. This recovery is called re-pumping. For Ba atoms in vacuum, re-pumping can be accomplished via three infrared lasers at wavelengths 1107.6 nm, 1130.0 nm, and 1500.0 nm for the direct transitions back to the  $6s6p\ ^1P_1^o$  state. An alternative re-pumping scheme is via excitation to higher-level states which have paths back to the ground state or the  $6s6p\ ^1P_1^o$  state. A few such higher-level re-pump transitions are shown in Fig. 2.1, including two red transitions to the  $5d6p\ ^3D_1^o$  state, and blue and violet transitions to the  $6s7p\ ^1P_1^o$  and  $6s8p\ ^1P_1^o$  states. Trapping and detection of Ba atoms in vacuum in a magneto-optical trap (MOT) was achieved in [28]. This was done with two separate re-pumping schemes: by incorporating three infrared re-pump transitions, as well as two infrared re-pump transitions and a 659.7-nm laser re-pumping the  $6s5d\ ^3D_1$  state via the  $5d6p\ ^3D_1^o$  state. Observation of trapped single  $\text{Ba}^+$  ions in vacuum has been achieved using 493.4 nm along with one re-pump laser at 649.7 nm [29, 30].

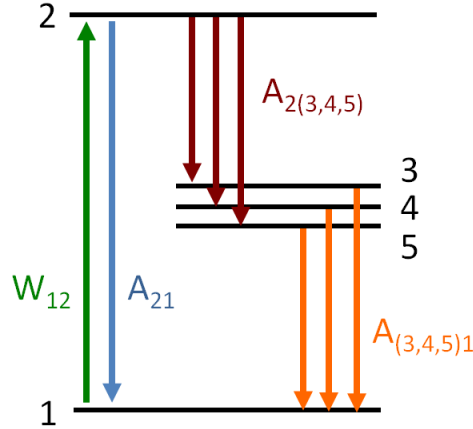


FIGURE 2.3. 5-level system diagram with excitation rate  $W_{12}$  and decay rates  $A_{ij}$ .

## 2.2. 5-LEVEL RATE EQUATIONS MODEL

A 5-level rate equations model for Ba transitions in vacuum, with excitation to the  $6s6p$   $^1P_1^o$  state, is shown schematically in Fig. 2.3. States 1 and 2 represent the  $6s^2$   $^1S_0$  and  $6s6p$   $^1P_1^o$  states, respectively, and states 3, 4 and 5 represent the  $6s5d$   $^1D_2$ ,  $6s5d$   $^3D_2$ , and  $6s5d$   $^3D_1$  states, respectively. The rate equations for this system, neglecting stimulated emission, are given in Eq. 7:

$$\begin{aligned}
 \frac{dN_1}{dt} &= -W_{12}N_1 + A_{21}N_2 + A_{31}N_3 + A_{41}N_4 + A_{51}N_5 \\
 \frac{dN_2}{dt} &= W_{12}N_1 - N_2(A_{21} + A_{23} + A_{24} + A_{25}) \\
 (7) \quad \frac{dN_3}{dt} &= A_{23}N_2 - A_{31}N_3 \\
 \frac{dN_4}{dt} &= A_{24}N_2 - A_{41}N_4 \\
 \frac{dN_5}{dt} &= A_{25}N_2 - A_{51}N_5
 \end{aligned}$$

where  $N_i$  is the population in state  $i$ ,  $A_{ij}$  is the spontaneous decay rate from state  $i$  to state  $j$ , and  $W_{12}$  is the excitation rate:

$$(8) \quad W_{12} = \frac{\sigma I}{h\nu}$$

where  $\sigma$  is the cross section for excitation,  $I$  is the laser intensity, and  $h\nu$  is the excitation photon energy.

Under some experimental conditions, the assumption can be made that  $W_{12}$  is small compared to the rates out of the  ${}^1\text{P}_1{}^\circ$  state. In this case the population in the excited state  $N_2$  is small compared to the populations of the other states. Except for very short times,  $dN_2/dt$  is also small compared to  $W_{12}N_1$  and  $N_2A_{21}$ . For these conditions, there is an effective pumping rate for the D states:

$$(9) \quad W_{1i} = W_{12} \frac{A_{2i}}{A_{21} + A_{23} + A_{24} + A_{25}}$$

where  $i = 3, 4, 5$ . The fraction in Eq. 9 is the respective branching ratio from the excited state 2. With this definition, the rate equations for states 3, 4, and 5 can be re-written as:

$$(10) \quad \begin{aligned} \frac{dN_3}{dt} &= W_{13}N_1 - A_{31}N_3 \\ \frac{dN_4}{dt} &= W_{14}N_1 - A_{41}N_4 \\ \frac{dN_5}{dt} &= W_{15}N_1 - A_{51}N_5 \end{aligned}$$

where  $N_1 = 1 - N_3 - N_4 - N_5$  by conservation of total population.

For a numerical solution of these equations, initially all population is in the ground state ( $N_3 = N_4 = N_5 = 0$ ). The model calculates the state populations  $N_i$  at the end of each iterative time step,  $t_{\text{step}}$ , as:

$$(11) \quad N_i = N_{i,\text{previous}} + \frac{dN_i}{dt} t_{\text{step}}$$

where  $i = 3, 4, 5$ , and  $dN_i/dt$  is determined at the beginning of each time step according to Eq. 10. Time steps of  $t_{\text{step}} = 1 \mu\text{s}$  were used. In order to model data, which is taken in exposure time ( $t_{\text{exp}}$ ) frames, the model iterates through  $t_{\text{exp}}/t_{\text{step}}$  steps in each frame, accumulating fluorescence photons emitted at each step ( $\Delta S_{\text{step}}$ ) according to the fluorescence rate times  $t_{\text{step}}$ :

$$(12) \quad \Delta S_{\text{step}} = W_{12} N_1 \frac{A_{21}}{A_{21} + A_{23} + A_{24} + A_{25}} t_{\text{step}}$$

To incorporate camera readout time, where laser exposure continues but fluorescence is not observed, populations and derivatives are iterated without adding to total counts.

Examples of modeled normalized photons emitted vs. time are shown in Fig. 2.4 for three values of  $W_{12}$ , using the transition rates of Ba in vacuum from Table 2.1. Decay of fluorescence occurs as atoms are optically pumped into the metastable D states. For long times the curves reach a steady state value. This model is compared to bleaching data of Ba in SXe in Sec. 5.4.1.



FIGURE 2.4. Modeled photons emitted in 0.5-s exposure frames for three values of  $W_{12}$ , using vacuum Ba transition rates, normalized to the first point. A readout time of 0.1 s is used between frames.

### 2.3. MATRIX ISOLATION SPECTROSCOPY

In the matrix isolation technique, a species of interest is trapped in a crystal, or “matrix,” of inert atoms/molecules such that it can be studied at leisure. To be effective, the temperature must be low enough to prevent diffusion of guest atoms, and the guest concentration must be low enough to prevent guest-guest interaction. The technique was originally proposed and demonstrated in [31], where otherwise short-lived species were studied by isolating them in various solid matrices. The proposed method of Ba tagging in SXe is a unique application of matrix isolation spectroscopy. In order to understand the spectroscopic effects which may be encountered due to interaction between the guest Ba atoms and Ba<sup>+</sup> ions and the host Xe atoms, some effects encountered in systems of metal atoms in rare-gas matrices are discussed.

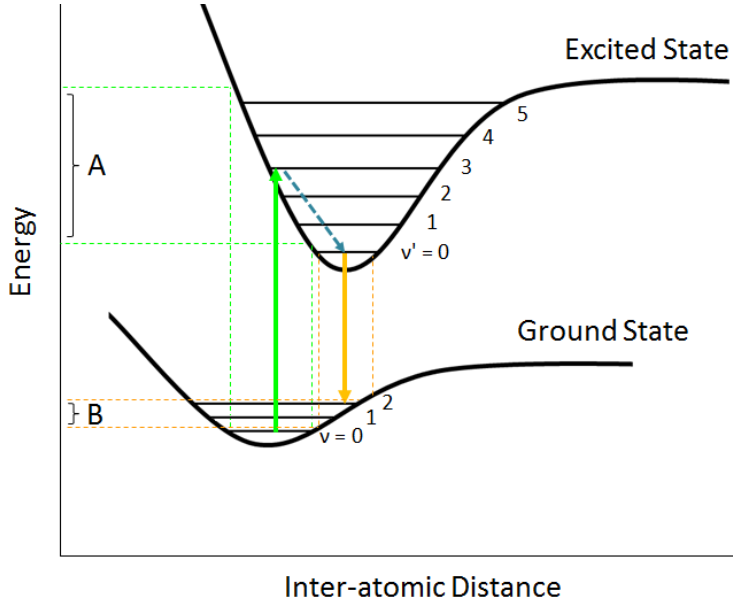


FIGURE 2.5. Illustration of the Franck-Condon Principle resulting in redshifted emission as well as broadening in absorption (A) and emission (B) due to vibrational modes  $\nu$  ( $\nu'$ ) in the ground (excited) state.

The leading interaction between a guest atom and the host noble gas atoms is an induced dipole-dipole Van der Waals force. For a metal atom of group I or II, this interaction is quite different when the atom is in the excited P state vs. the ground S state, resulting in general in different shaped potential energy curves [32]. To illustrate the concept, guesses at the ground and excited state potentials for a BaXe molecule are shown in Fig. 2.5. In a cold matrix, the system will be mainly in the ground lattice vibrational state ( $\nu = 0$ ) before excitation. According to the Franck-Condon principle, the strongest electronic excitation will occur to vibrational states whose wavefunctions overlap that of the ground state. Because this occurs for a band of vibrations, the absorption is broadened. The peak absorption energy is determined by the difference in potential energy between the ground state and the median vibrational state excited, which in general is not the same as the absorption energy of atoms in vacuum. In the excited state, rapid decay occurs to the lowest vibrational state, and then a similar broadening in the spontaneous emission energy occurs. A redshift in the emission



FIGURE 2.6. Excitation and emission spectra of Na atoms in SAr, SKr, and SXe. [34]

is observed relative to the excitation. Additionally, splitting of orbital degeneracy in the P state can produce triplet structures in the absorption according to the Jahn-Teller effect [33]. These features depend on the specific configuration of atoms surrounding the guest, and thus different spectra can be observed from guest atoms occupying different matrix “sites.” Annealing a matrix after deposition can reveal the relative stability of various matrix sites [32].

As an example, the spectroscopy on Na atoms in solid rare-gas matrices was studied in [34]. Spectral features are exemplified in Fig. 2.6 for Na atoms in SAr, SKr, and SXe. Excitation and emission are broadened to tens of nm. Two or three different matrix sites are observed in the three matrices, with the largest red-shift in emission observed in SXe. The triplet structures in excitation spectra are attributed to the Jahn-Teller effect. The specific

matrix configuration associated with each excitation triplet is identified in this paper through theoretical modeling of the Na-matrix interactions.

## 2.4. FLUORESCENCE EFFICIENCY

The fluorescence efficiency ( $\epsilon_f$ ) is the ratio of total fluorescence photons emitted to photons absorbed. This can be calculated by Eq. 13:

$$(13) \quad \epsilon_f = \frac{f}{W_{12}N_1\epsilon_{\text{tot}}}$$

where  $f$  is the number of fluorescence photons observed per atom per second,  $W_{12}N_1$  is the excitation rate ( $N_1 \approx 1$  for short times), and  $\epsilon_{\text{tot}}$  is the photon detection efficiency of the system.  $W_{12}$  can be calculated by Eq. 8. The cross section can be calculated using the shape of an excitation spectrum according to Eq. 14:

$$(14) \quad \sigma(\nu) = A_{21} \frac{g_2}{g_1} \frac{c^2}{8\pi\nu^2} g(\nu)$$

where  $A_{21}$  is the atomic transition rate,  $g_1$  and  $g_2$  are the ground and excited state degeneracies, respectively, and  $\nu$  is the photon frequency. Here we have assumed that the integrated cross section is unchanged in the solid matrix as compared to in vacuum. The normalized line shape  $g(\nu)$  must satisfy:

$$(15) \quad \int_0^\infty g(\nu)d\nu = 1$$

Integrating Eq. 14 then yields:

$$(16) \quad \int_0^\infty \sigma(\nu) \nu^2 d\nu = A_{21} \frac{g_2}{g_1} \frac{c^2}{8\pi}$$

Since the cross section  $\sigma(\nu)$  is proportional to the excitation spectrum  $E(\nu)$ , we can finally write the cross section as a function of  $\nu$  according to Eq. 17:

$$(17) \quad \sigma(\nu) = \frac{A_{21} E(\nu)}{\int_0^\infty E(\nu') \nu'^2 d\nu'} \frac{g_2}{g_1} \frac{c^2}{8\pi}$$

## CHAPTER 3

# EXPERIMENTAL

In this chapter the apparatus at Colorado State University that was used for producing and observing deposits of Ba and Ba<sup>+</sup> in SXe is presented. The main barium source, a Ba<sup>+</sup> ion beam, is first described in Sec. 3.1, and then a neutral Ba getter source is discussed in Sec. 3.2. The co-deposit of Ba or Ba<sup>+</sup> with Xe gas onto a cold sapphire window is described in Sec. 3.3. The technique for focusing the laser into the SXe is outlined in Sec. 3.4, and imaging of the laser region is described in Sec. 3.5, with attention to the effect of vibrations in Sec. 3.7.

### 3.1. ION BEAM SYSTEM

The Colutron [35] ion beam system is a clean mass-selected source of Ba<sup>+</sup> which, with the added capability of pulsing, can do a very wide range of deposit sizes, from billions of ions in a focused laser region all the way down to the single-ion level and below. The different components of this system are shown in Fig. 3.1 and described in the following subsections. Ions produced in a Colutron ion source are accelerated and collimated for passage through the mass filter. Several sets of deflection plates are available for steering, and Einzel lenses focus the beam near the final Faraday cup. A set of pulsing plates can be used to deposit 1- $\mu$ s ion pulses in SXe on the cold sapphire window, or continuous ion current can be used in depositing larger numbers of ions.

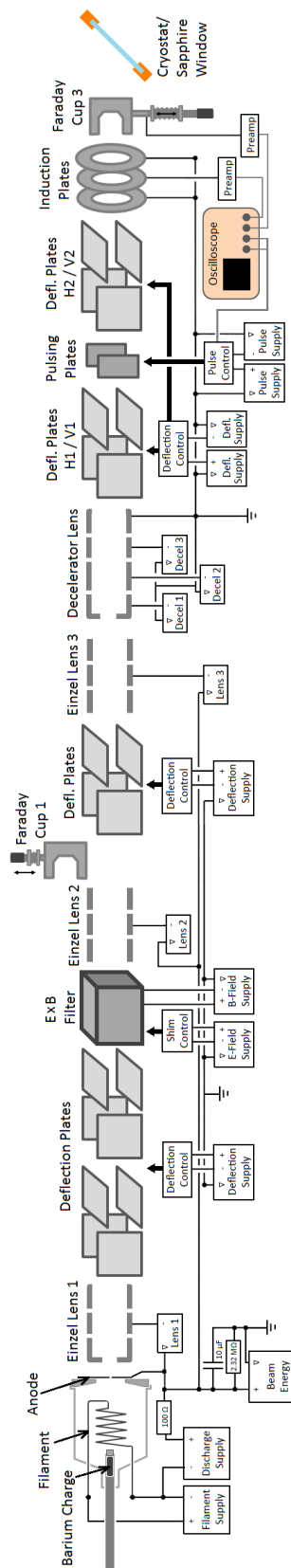


FIGURE 3.1.  $\text{Ba}^+$  ion beam system.



FIGURE 3.2. Colutron  $\text{Ba}^+$ /Ar<sup>+</sup> ion source.

### 3.1.1. ION SOURCE

$\text{Ba}^+$  ions are produced in the source of a Model DCIS-101 Colutron ion gun [36]. It is shown in Fig. 3.2. A solid Ba charge is placed into the hollowed end of a stainless steel rod, which is capped by a loose screw. The source rod is inserted into the discharge chamber, where it is heated by a filament, vaporizing the Ba. The source is designed to produce a discharge between the anode plate and the filament cathode, through an argon buffer gas leaked into the source chamber. This controlled discharge also ionizes Ba atoms in the vapor to produce the desired  $\text{Ba}^+$  ion beam. In the present work, to avoid contamination of the SXe matrix with residual Ar gas, the buffer gas was not used. It has been found that, with care, the discharge can be maintained with Ba vapor alone. The longevity of ion current from a single charge is at least several tens of hours. This suggests that Ba is coating the inner walls of the source chamber, and is heated enough to provide sufficient Ba pressure to support a discharge.

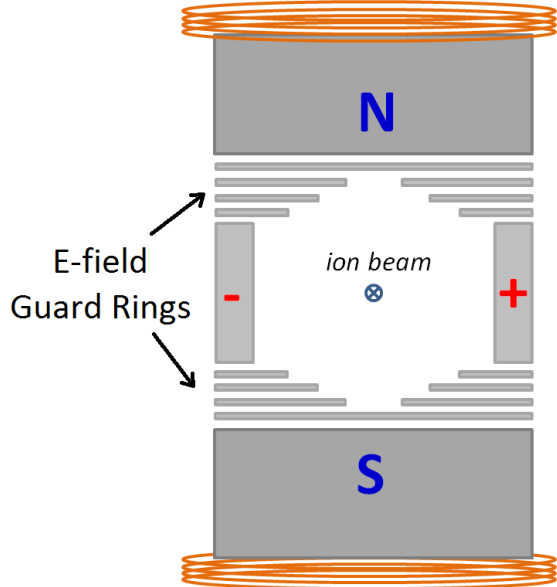


FIGURE 3.3. Colutron  $E \times B$  ion velocity filter.

The discharge produces a plasma that contains barium ions. The application of a 2 kV acceleration potential between the ion source anode and the first element of Einzel lens 1 (L1) draws  $Ba^+$  ions from the plasma. The potential of this lens is adjusted to collimate the ion beam for passage through the  $E \times B$  velocity filter.

### 3.1.2. $E \times B$ VELOCITY FILTER

The  $E \times B$  velocity filter selects  $Ba^+$  by creating perpendicular electric and magnetic fields, which produce opposing forces on charged particles moving through the filter. The opposing forces will be equal for ions with velocity  $v = \frac{E}{B}$ . Since ion velocity is determined by mass ( $m$ ), charge ( $q$ ) and beam potential ( $V$ ), the filter selects ions satisfying Eq. 18:

$$(18) \quad \frac{m}{q} = \frac{2VB^2}{E^2}$$

where  $B$  and  $E$  are the magnetic and electric fields, respectively. Those fields are chosen such that  $\text{Ba}^+$  ions pass straight through. Other ions, e.g.  $\text{Ar}^+$ , will be deflected.

The  $E \times B$  filter is shown in Fig. 3.3. Electromagnets provide a vertical magnetic field. Electrode plates and field-shaping guard rings provide a horizontal electric field. The guard rings prevent lensing and astigmatism from the fringe fields of the plates [36].

### 3.1.3. OTHER BEAM COMPONENTS

The first three sets of deflection plates shown in Fig. 3.1 can be used for beam diagnostics, and are set to 0 V during normal operation. The fourth set of deflection plates, H1 and V1, located just before the pulsing plates, are set to constant values of +50 V and 0 V, respectively. These voltages have been selected such that the beam, in both pulsing and continuous modes, can be deposited at the sapphire window for reasonable settings on the final deflection plates, H2 and V2. As described in Section 3.1.5, different settings in H2/V2 are required for peak ion current in Faraday cup 3 vs. peak deposit at the window.

Einzel lens 2 (L2) focuses the beam to pass through the aperture in the first element of the decelerator lens. Einzel lens 3 (L3) is set to zero in this setup. If desired, the decelerator lens can be used to vary the  $\text{Ba}^+$  deposit energy, which was done in [37], but in this work it acts as an Einzel lens with only the second element (D2) at non-zero voltage. It focuses the beam near the sample and Faraday cup 3 (there is no Faraday cup 2 in this setup).

Faraday cup 3 measures the ion current during experiments, and is retracted when deposits are being made. Calibration of deposits using Faraday cup 3 is described in Section 3.1.5. Faraday cup 1 can be used for beam diagnostics, and is usually retracted. An additional Faraday cup, cup W, can be attached to the coldfinger, in place of the sapphire



FIGURE 3.4. Pulsing circuit.  $R_1 = R_2 = 470 \Omega$ ,  $R_3 = R_4 = 20 \text{ k}\Omega$ , and  $C_1 = C_2 = 680 \text{ nF}$ . [37]

window, for determining optimum deflection plate voltages for depositing  $\text{Ba}^+$  on the sapphire window and for calibrating ion deposits. This is described further in Sec. 3.1.5.

To align the ion beam, L1 was first tuned to maximize ion current in Faraday cup 3, with L2, L3, and D2 set to zero. Since cup 3 is about 2 m away from L1, this approximately collimates the beam for passage through the  $E \times B$  filter. The optimal value for L1 was found to be around -400 V relative to the 2000 V beam energy. Next, L2 and D2 were fine-tuned together to achieve maximal current in cup 3. Finally, the straightness of the beam was checked by peaking the ion current with the final four deflection plates on cup 3 and cup W.

### 3.1.4. ION BEAM PULSING

To deposit small numbers of ions, it is desirable to be able to pulse the ion beam with short pulses. To achieve pulsed beams, the pulsing plates, normally set to 200 V and -200 V

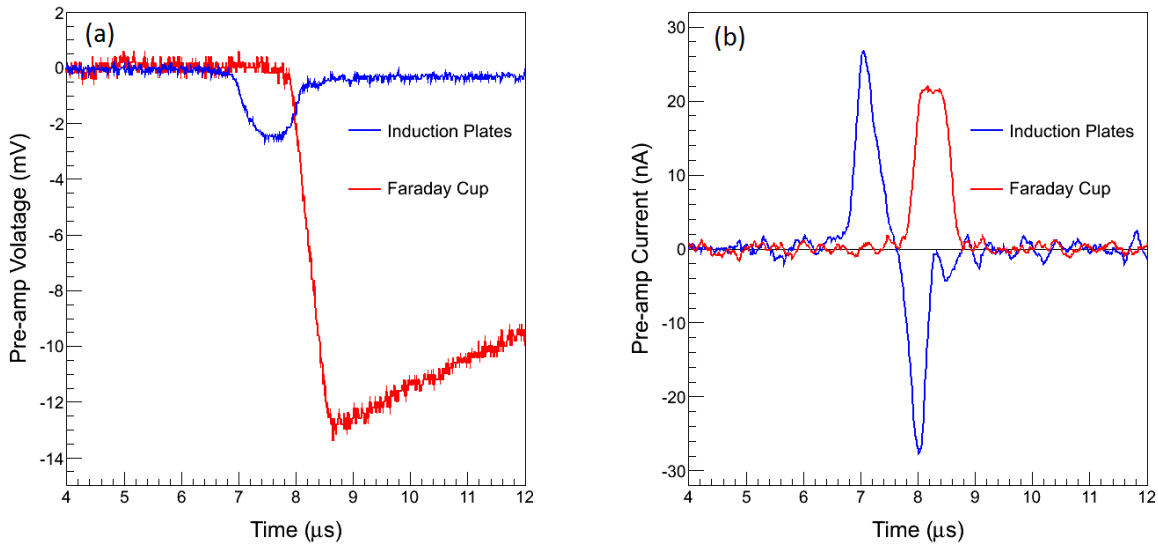


FIGURE 3.5. (a) Raw voltage and (b) calculated current pulse signals from the induction plates and cup 3. The raw induction signal appears small because it has a less sensitive pre-amp (accounted for in calculating the current).

to deflect the beam, are pulsed to 0 V for 1  $\mu$ s to pass a short pulse of ions straight forward. The pulsing circuit is shown in Fig. 3.4. Square waves, triggered by LabVIEW at 500 Hz, enter the circuit at (a). A transformer isolates a MOSFET switch from ground. Upon a trigger pulse the MOSFET switch shorts the pulsing plates for the period of the pulse.

The pulsing plates are followed by three induction plates, the middle plate of which provides a measure of the ion pulses. Just prior to a deposit, the charge in the pulses can be directly measured on cup 3. Pre-amplifiers made by eV Products convert the ion current in the induction plates and cup 3 (or cup W) to voltage signals, which are recorded on a digital oscilloscope. An example of raw oscilloscope traces of Faraday cup 3 and induction plate signals are shown in Fig. 3.5a. The input current is related to the pre-amp output voltage according to Eq. 19:

$$(19) \quad I = \frac{-(V_{out} + R_1 C \frac{dV_{out}}{dt})}{R_1 M}$$

where  $R_1 C$  and  $R_1 M$  are determined by putting a known square pulse of current into the pre-amp through a large resistor. First, the time constant of an exponential fit to the signal decay after the pulse determines  $R_1 C$ . Then  $R_1 M$  is determined by matching the amplitude of the calculated current signal to the original square-pulse input current. The actual currents in the induction plates and cup 3 calculated using Eq. 19 are shown in Fig. 3.5b. The induction current is positive as ions are approaching the middle plate, and an equal but negative current is seen after the ions pass this plate. The Faraday cup stops the ions, so it produces only a positive induction current as ions approach it.

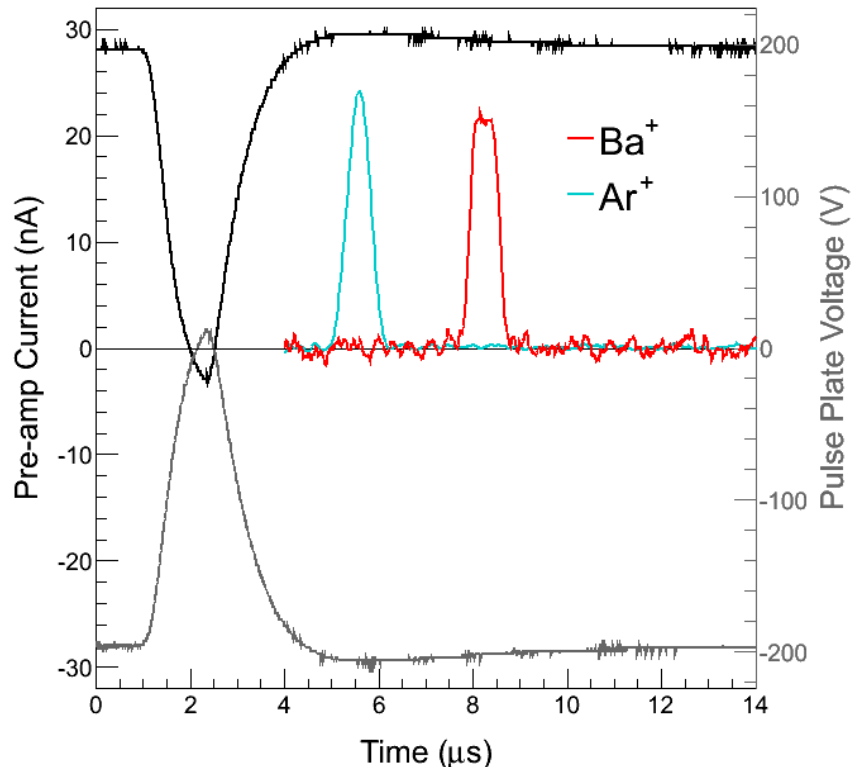


FIGURE 3.6. Arrival time of pulses at cup 3 vs. time of pulsing plate signal (black (+) and gray (-)) for  $\text{Ar}^+$  and  $\text{Ba}^+$  ions at 2000 eV.

Pulsing data also provide confirmation that the beam is composed of  $\text{Ba}^+$ . The time between the pulsing plate voltage peak and the center of the pulse measured by the Faraday cup, along with the known distance traveled, determines the velocity of the ions. The distance from the center of the pulsing plates to the Faraday cup was measured to be  $31.5 \pm 0.5$  cm. Time-of-flight data, e.g. Fig. 3.6, give  $39.8 \pm 3.4$  amu for  $\text{Ar}^+$  ions and  $136.8 \pm 6.3$  amu for  $\text{Ba}^+$  ions, including an uncertainty on the time of flight of  $\pm 0.1 \mu\text{s}$ . These agree with the known atomic masses.

### 3.1.5. CALIBRATION OF ION DEPOSITS

The ratio between the continuous ion currents in cup 3 and cup W was typically measured to be  $r_w = 0.5$ . As the ion beam at cup W is significantly wider than the cup diameter and is thought to be fairly uniform, the ion density per pulse at the sapphire window is given by:

$$(20) \quad \frac{\text{ions}}{\text{pulse} \times m^2} = \frac{Qr_w}{eA}$$

where  $Q$  is the charge/pulse at cup 3,  $A$  is the area of cup W, and  $e$  is the elementary charge. The radius of the opening in cup W is 1.4 mm. Each time cup W is inserted, the voltages on the final deflection plates H2 and V2 that optimize the signal in cup W, in pulsed and in continuous mode, are determined. In the latest imaging experiments, these differed from the values for maximum cup 3 signal by about 70 V in H2 and 60 V in V2, corresponding to a displacement of the undeflected beam of about 4 mm in x and y position at cup W relative to the center line from cup 3.

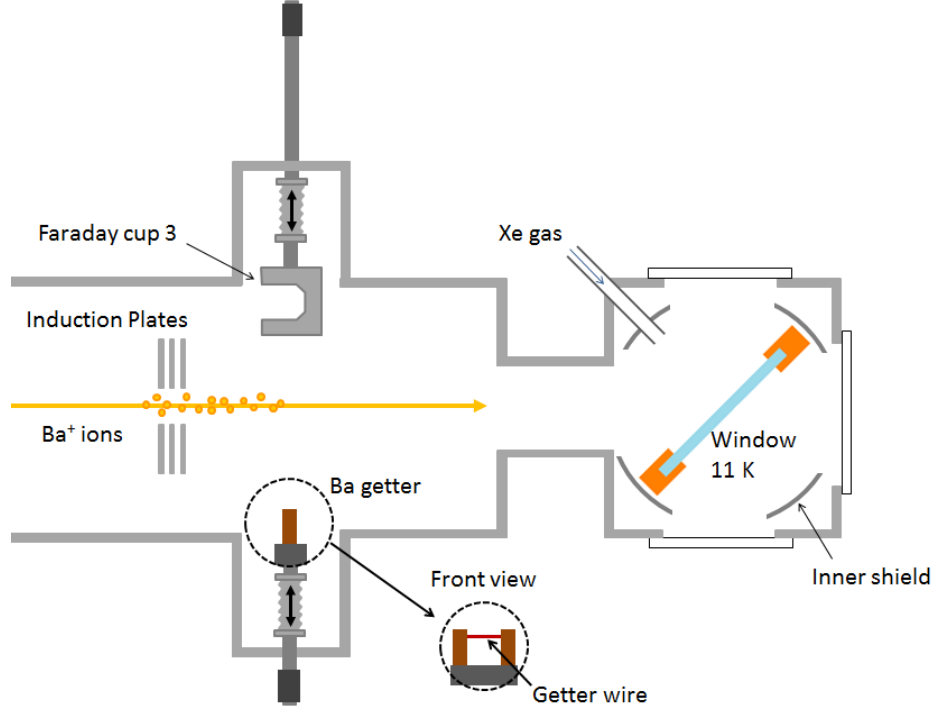


FIGURE 3.7. Apparatus near the sapphire window, including induction plates, Ba getter, Faraday cup 3, Xe gas inlet, and sapphire window at 11 K.

The number of ions being observed is then determined by multiplying the ion density from Eq. 20 by the area of the sapphire window being observed, defined either by the area of a focused excitation laser beam or by the number of pixels being used in an image of a defocused excitation laser beam. An additional factor of 0.8 was applied to this final number of ions to account for the angle between the optical axis of the laser and the horizontal ion path. The area of the focused laser beam is discussed further in Sec. 3.7.

### 3.2. BA GETTER SOURCE

A BaAl<sub>4</sub> getter (SAES with part number ST 2/F/WIRE), can be inserted on a bellows to emit Ba atoms toward the sapphire window, as shown in Fig. 3.7. When heated, the getter emits neutral Ba with minimal Ba<sup>+</sup> content due to the low temperature ( $\sim 800^\circ \text{ C}$  determined by observing brick red color temperature). Getters were used extensively in previous work

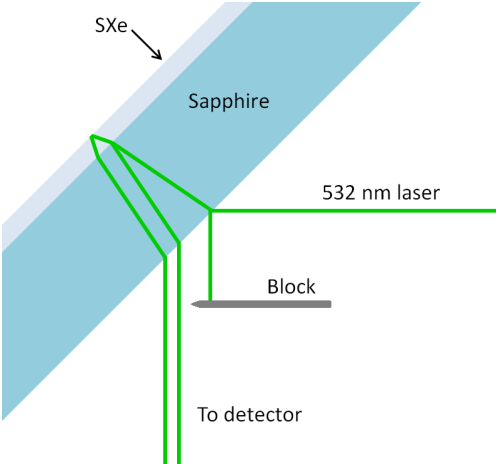


FIGURE 3.8. Setup for measuring SXe deposition rate by interference fringes.

[38] for measuring the absorption and emission spectra of Ba in SXe with large Ba deposits. A getter was used briefly in this work in verifying that the 619-nm fluorescence peak, that is used for single Ba imaging, is actually a neutral Ba peak, as described in Section 5.2. The barium getters used in [38] were exothermic BaAl<sub>4</sub>-Ni flash getters. The getter used here is an endothermic BaAl<sub>4</sub> type, designed for more controlled Ba emission.

### 3.3. SAMPLE DEPOSITION

The Ba<sup>+</sup>/Ba is co-deposited with 99.995% purity Xe gas onto a cold sapphire window. Sapphire has good thermal conductivity at low temperature and good optical transparency in the visible. The window is held in a copper mount attached to a coldfinger and is tilted at 45° to allow access of the ion beam and Xe gas, as well as the excitation laser and collection optics. To begin a deposit, Xe gas is flowed toward the window via a leak valve, through an inlet system designed and built by Brian Mong and Shon Cook [38, 37]. Cup 3 is then retracted and the pulsing plates are pulsed to zero volts, depositing 1-μs pulses of Ba<sup>+</sup> ions into the SXe matrix as it grows. Cup 3 is then replaced, and the Xe leak stopped.

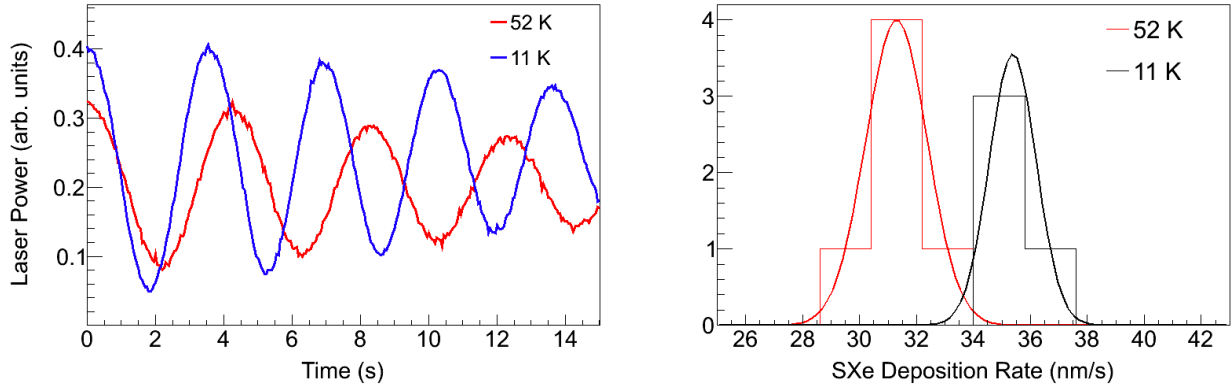


FIGURE 3.9. (a) Interference fringes for the same Xe gas leak rate deposited on the sapphire window at 11 K and at 52 K, and (b) distribution of SXe deposition rates calculated from fringe period of several measurements.

The SXe matrix deposition rates have been measured by interference fringes in a 532-nm laser reflected from the front surface of the sapphire window and the SXe surface, as shown in Fig. 3.8. Fringes for SXe deposition at 52 K and 11 K are shown in Fig. 3.9a for the typical leak rate used in this work. The refractive index of SXe has a negligible dependence on temperature between 50 and 30 K [39], so these rates can be compared directly. A distribution of SXe deposition rate measurements from several deposits is shown in Fig. 3.9b. A rate of  $31.2 \pm 0.9$  nm/s is measured for deposits at 52 K, and a somewhat higher rate of  $35.6 \pm 0.9$  nm/s is measured for deposits at 11 K.

To evaporate a sample, the window is heated to 100 K. Fringes appear during this process as well. The full set of fringes for a deposit at 52 K and during its evaporation when heated is shown in Fig. 3.10, along with the window temperature. It is observed that the SXe evaporates between 73 K and 78 K. The same number of fringes appear in the deposit and the evaporation, indicating that the lower deposition rate at around 50 K is not due to simultaneous evaporation, but perhaps it is due to a different sticking coefficient. The variation in temperature during the deposit is due to the heater cycle. These Xe deposits

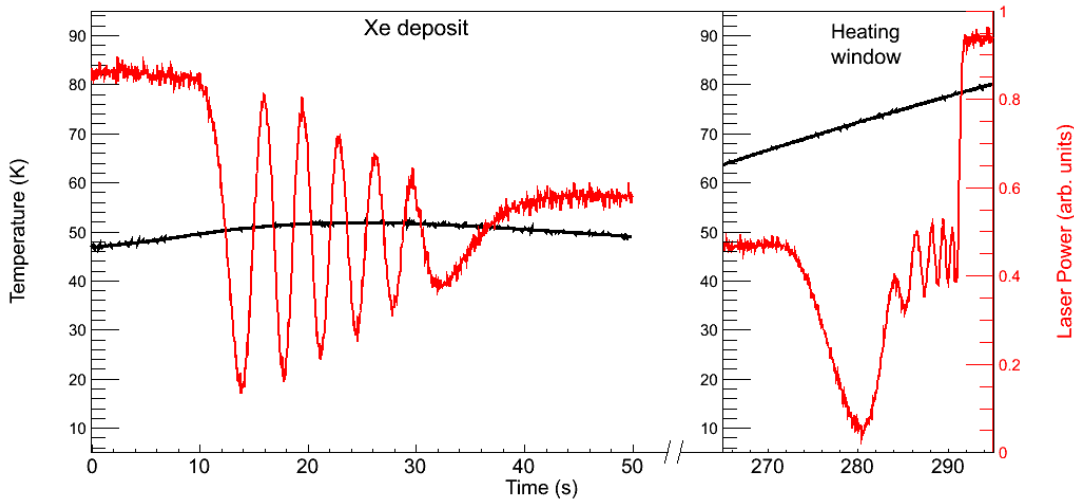


FIGURE 3.10. Interference fringes (red) of a SXe deposit at 52 K and of its subsequent evaporation when heating the sapphire window, and temperature (black) vs. time.

were for a longer time than in a typical deposit during a fluorescence experiment, in order to observe several fringes.

### 3.4. LASER EXCITATION

Green to yellow laser excitation is done with a Coherent 599 dye laser, pumped by the 514-nm line of a Lexel 3500 Ar ion laser. Rhodamine 110 (R110) dye is used for the 542 - 566 nm wavelength range, and Rhodamine 6G (R6G) for the 567 - 590 nm range. Another Coherent 599 dye laser with Coumarin 480 (C480) dye, pumped by a Kr ion laser, is used for blue excitation. The Coherent 599 dye lasers are used with birefringent filters for wavelength tuning, but without etalons or single frequency stabilization, since the broad absorption of Ba and Ba<sup>+</sup> in SXe does not require narrow band laser excitation.

The optics for these experiments is shown in Fig. 3.11. In initial work, including spectroscopy (Chapter 5) and some imaging (Chapter 6), a bi-convex lens was used. This lens had a little spherical aberration, resulting in blurring of the laser focus. This aberration

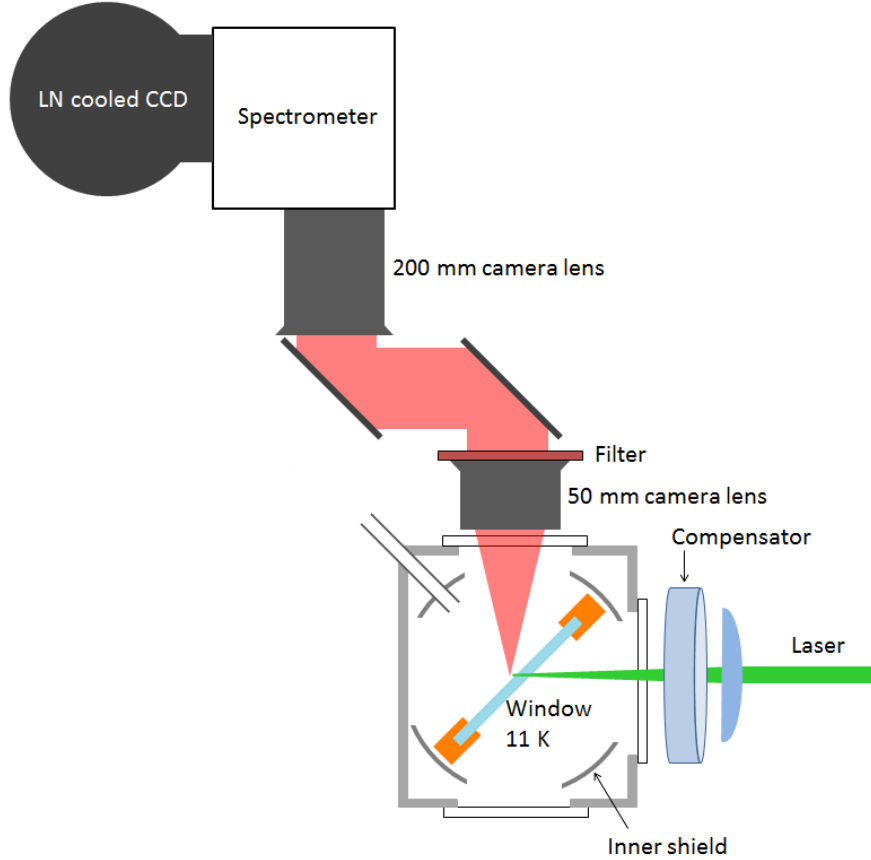


FIGURE 3.11. Apparatus in the spectroscopy region, including optics for excitation, fluorescence collection, spectroscopy and detection.

does not affect the spectroscopy results in Chapter 5, where semi-focused beam  $1/e^2$  radii of 100-1000  $\mu\text{m}$  were used. However, spherical aberrations caused the minimum beam radius to be about 5  $\mu\text{m}$ . To approach the diffraction limit in imaging small numbers (Chapter 6), a 7.9-cm focal length aspherical lens was used. A comparison of the minimum spot sizes for these two lenses, calculated by David Fairbank of Thorlabs with OpticStudio software, is shown in Fig. 3.12.

The tilted sapphire window introduces astigmatism to the focused laser. To correct for this, compensating astigmatism is introduced by a fused silica optical flat of 1 cm thickness, placed after the lens with the normal to its surface tilted in the horizontal xz plane (the laser

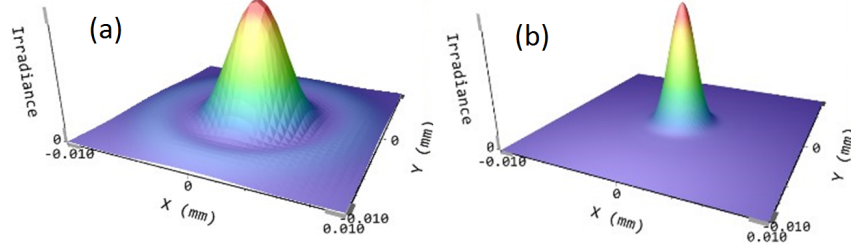


FIGURE 3.12. Calculated minimum laser spot size distributions, with wavelength 570 nm and laser radius  $w = 7$  mm incident on the lens, for (a) bi-convex  $f = 7$  cm lens, and (b) aspherical  $f = 7.9$  cm lens. [40]

is along the z-direction, and the normal to the sapphire window is tilted in the vertical yz plane). The proper angle for the compensator was determined to be about  $10^\circ$  from normal by a ray matrix calculation [41]. The effect of astigmatism of the SXe layer is negligible since its thickness is only about half a micron in a typical fluorescence experiment. With the compensator, overlapping minimum spot sizes of  $2.06 \mu\text{m}$  and  $2.66 \mu\text{m}$  in the plane of the SXe deposit are calculated for x and y, respectively.

To observe the astigmatism and the effect of the compensator, the relative positions in z of the x and y foci were observed by imaging 619-nm Ba fluorescence from a large deposit of  $\text{Ba}^+$  in SXe with varying z-position of the laser focusing lens. For each z, an image was taken, and a 2D Gaussian fit determined the  $1/e^2$  x- and y- radii,  $w_x$  and  $w_y$ , of the image. Although these radii are significantly larger than that of the laser beam due to SXe surface scattering and collection optics imperfections, the z-position of the best focus can be accurately determined. Example fits to the 619-nm fluorescence images for three laser focus positions, using the astigmatism compensator at  $10 \pm 1^\circ$ , are shown in Fig. 3.13(a,b,c). Gaussian fit values for  $w_x$  and  $w_y$  are plotted vs. laser lens position with (d) no compensator, and with the compensator at (e)  $10 \pm 1^\circ$ , (f)  $11 \pm 1^\circ$ , and (g)  $13 \pm 1^\circ$ . With no compensator (d), the focal positions for x and y are measured to be  $127.6 \pm 2.5 \mu\text{m}$  apart. Compensation angles  $10 \pm 1^\circ$  (e) and  $13 \pm 1^\circ$  (g) can be seen to under- and over-shoot the optimal angle,

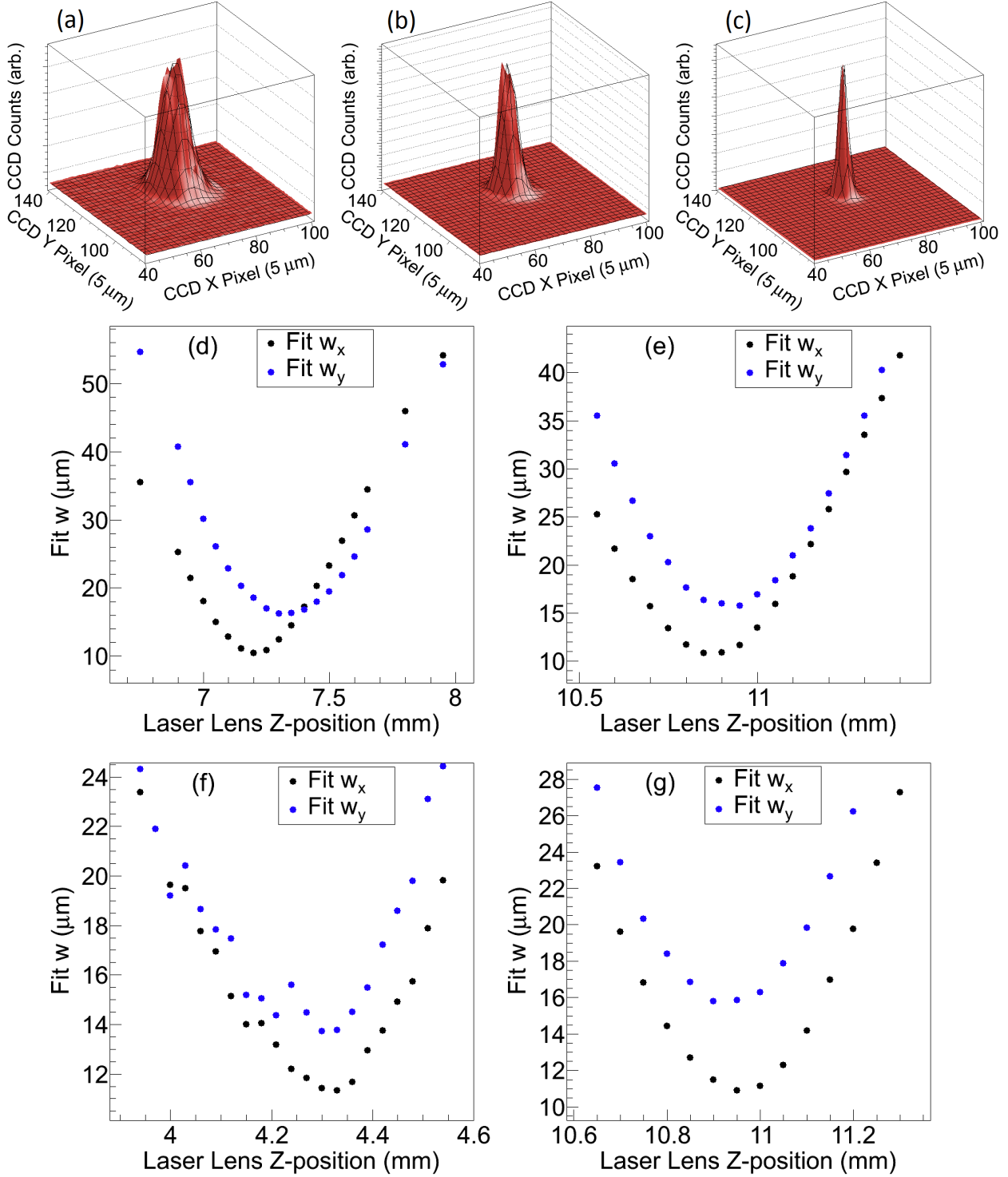


FIGURE 3.13. Example 2D Gaussian fits (black grid lines) with varying laser z position (a,b,c), and fit radii  $w_x$  (black) and  $w_y$  (blue) vs. laser focus lens position with (d) no compensator, and with compensator at about (e) 10°, (f) 11°, and (g) 13°.

respectively. The angle  $11\pm1^\circ$  (f), which was used in imaging experiments, is near optimal, i.e. the x and y focal positions are consistent to within  $45 \mu\text{m}$ .

The laser spot size ( $A_{\text{laser}}$ ) in the plane of the SXe is defined as the area enclosed within the radii of the laser beam at  $1/e$  of peak intensity, according to Eq. 21:

$$(21) \quad A_{\text{laser}} = \frac{\pi w_x w_y}{2}$$

where  $w_{x,y}$  are the  $x$  and  $y$   $1/e^2$  radii of the focused laser in the SXe. In the case of the bi-convex lens,  $w_x \approx w_y \equiv w$ .

TABLE 3.1. Factors contributing to optical collection efficiency.

Component	Efficiency
Solid Angle	0.015
Cryostat Window	0.99
Camera Lens 50 mm	0.89
Camera Lens 200 mm	0.91
Steering Mirrors ( $\times 2$ )	0.95
CCD Quantum Efficiency	0.90
Filter	0.98
Counts per Photoelectron (CCD)	0.467
Spectrometer	0.5
	$\epsilon_c(\text{w/o spectrom.}) = 4.5 \times 10^{-3}$
	$\epsilon_c(\text{w/ spectrom.}) = 2.2 \times 10^{-3}$

### 3.5. COLLECTION OPTICS

Fluorescence is collected above the cryostat, as shown in Fig. 3.11. A 50 mm Nikon camera lens collimates the light, and one or more fluorescence filters sit on top of it. A band-pass filter is used for imaging, and a Raman filter is used for spectroscopy. The fluorescence is then guided by two steering mirrors, and is imaged by a 200 mm Nikon camera lens onto a Roper Scientific liquid-nitrogen-cooled CCD, with a net magnification of 4. The CCD has a specified quantum efficiency of 90% in the visible, and in its medium gain mode and 50 kHz

digitization rate, records one count per 2.14 photoelectrons collected [42]. At the set point of -100 °C, dark counts are negligible.

For spectroscopy, the 200 mm camera lens focuses the light onto the inlet slit of an Acton SP-2150i imaging spectrometer, which images the light onto the CCD after reflecting off a diffraction grating. The 0-order reflection of the grating provides an image for alignment when a wide slit is used, and the grating is used in 1<sup>st</sup>-order with a narrow slit to disperse the spectrum across the horizontal CCD pixels for doing spectroscopy.

When a 1" diameter filter is used, the imaging system has a solid angle of light collection of 1.5%. Each additional component in the collection optics, listed in Table 3.1, contributes some loss, resulting in a total collection efficiency ( $\epsilon_c$ ) of  $2.2 \times 10^{-3}$  with the spectrometer, and  $4.5 \times 10^{-3}$  without. The spectrometer f-number of 4 is not limiting in this setup.

To avoid unnecessary fluorescence bleaching (bleaching is described in Sec. 5.4), a laser shutter was linked to the camera shutter with a LabVIEW program. This program also recorded laser power via a Si photo-detector and a calibrated pickoff plate, as well as the temperature of the coldfinger near the sapphire window during observation.

Although the imaging spectrometer can produce spatial images with the 0-order grating reflection, better collection efficiency and imaging quality are achieved by removing the spectrometer and imaging directly onto the CCD. Band-pass filters were used to pass the desired Ba fluorescence peak(s) while greatly attenuating laser scatter and sapphire fluorescence.

An example raw image of the focused 570 nm dye laser on a Ba<sup>+</sup> deposit using the 619-nm fluorescence peak is shown in Fig. 3.14. With 4× magnification, each pixel corresponds to 5 μm × 5 μm on the window. The laser's path through the window is faintly visible by the residual broad Cr<sup>3+</sup> fluorescence that is passed by the 620-nm band-pass filter. The

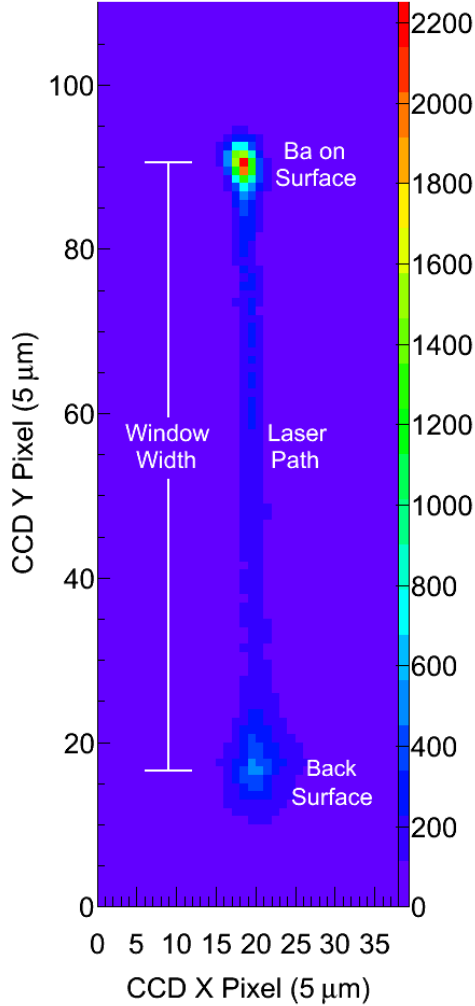


FIGURE 3.14. Example image of a  $\text{Ba}^+$  deposit on a c-plane sapphire window of 0.5 mm thickness excited by a focused laser, using a 620-nm fluorescence band-pass filter.

laser is focused at the top surface of the window, which faces the ion beam. The surface background is seen on the back surface, and the 619-nm Ba fluorescence stands out above both backgrounds on the top surface. The imaging resolution results in a  $1/e^2$  radius of about 12  $\mu\text{m}$  when imaging the  $2.06 \mu\text{m} \times 2.66 \mu\text{m}$   $1/e^2$  laser spot.

### 3.6. WAVELENGTH CALIBRATION

Wavelength calibration of the spectrometer was done using three lasers whose wavelengths were first measured with a Burleigh Wavemeter: a red diode laser at 656.99 nm, a doubled

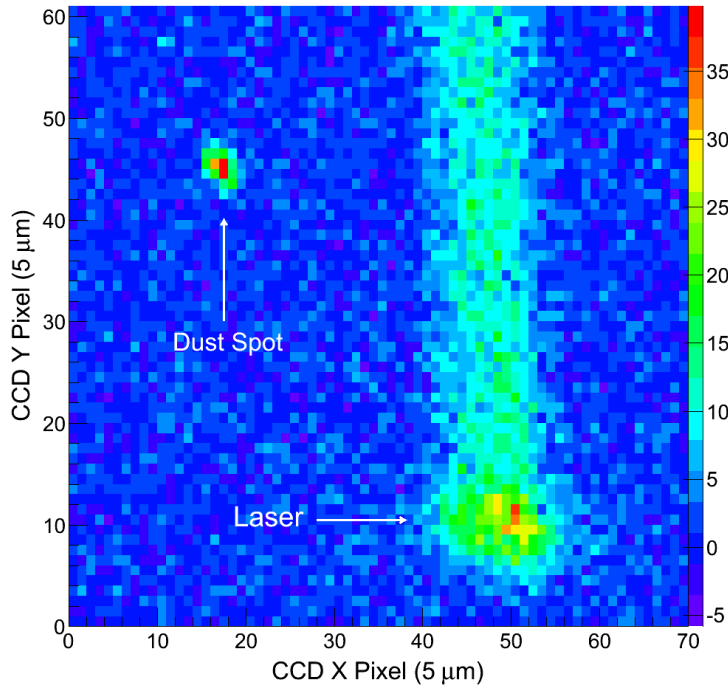


FIGURE 3.15. Example image of a dust spot and the laser during observation of cryostat vibrations.

Nd:YAG laser at 532.23 nm, and the C480 blue dye laser typically around 475 nm. These lasers were directed at the same position on the sapphire window, and their scatter was imaged along the same path as the Ba fluorescence. The WinSpec software applies the diffraction grating equation to calibrate each CCD pixel to a wavelength.

### 3.7. VIBRATIONS AND EFFECTIVE LASER REGION

Relative vibrations between the laser and the sapphire window could occur on the micron scale from a few sources. First, the laser is on a separate optical table from the cryostat and collection optics. Second, the cryostat vibrates due to its He pump cycles. Vibrations increase the total number of Ba atoms exposed during a measurement, but not the instantaneous number of Ba atoms in the laser beam area.

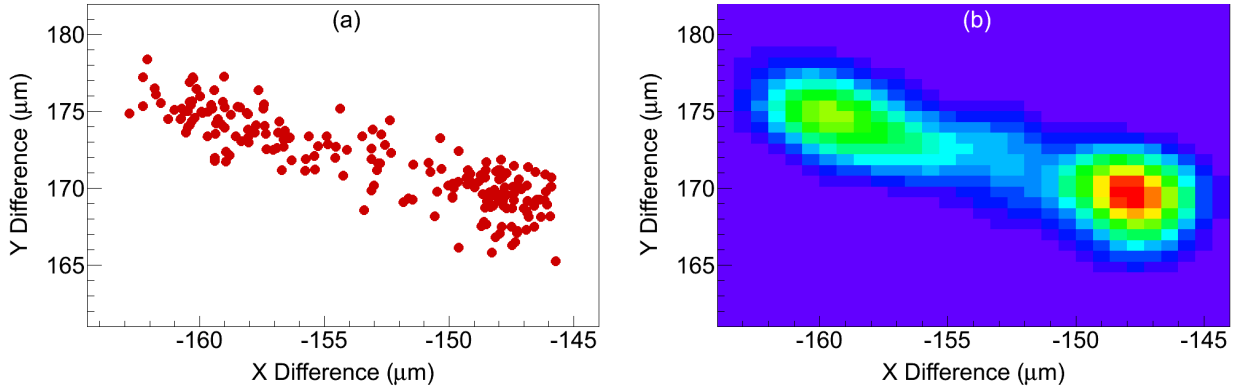


FIGURE 3.16. Cryostat vibration measurements based on the relative position between the dust spot and the laser on the sapphire window in 50-ms snapshots (a), with 2D Gaussians of  $w_x \times w_y = 2.06 \mu\text{m} \times 2.66 \mu\text{m}$  overlaid on each point and summed to represent total laser exposure vs. position (b).

Vibrations were observed by determining the position of a “dust spot” (a highly scattering feature on a sapphire window) relative to the position of the laser in an image on time scales down to 50 ms. An example of an image from this experiment is shown in Fig. 3.15. The dust spot was illuminated by a defocused 657 nm diode laser, and the 570-nm dye laser was somewhat defocused in order to optimally defocus the red laser with the same focusing lens. For each frame, 2D Gaussian functions with variable widths and magnitudes were fit to locate the center of the laser spot and the dust spot in order to measure their relative position. The fit range for the laser spot was restricted in y so that it was not affected by the bulk sapphire fluorescence path. The distances in x and y between the dust spot and laser are plotted for each 50-ms snapshot in Fig. 3.16a. CCD readout and shutter compensation time occur for about 877 ms between frames. The distribution shows a correlation between x and y, indicating vibration in a particular direction. Sinusoidal motion results in a collection of data points at the two ends. The amplitude of the vibration is about 15  $\mu\text{m}$  from this data.

To calculate an effective laser area with this vibration, each difference  $(x,y)$  between laser and dust spot was used as the center of a 2D Gaussian, each with  $w_x = 2.06 \mu\text{m}$  and  $w_y = 2.66 \mu\text{m}$  to represent the laser spot. Such Gaussian functions were summed for all points to produce a distribution of summed laser exposure, shown in Fig. 3.16b. The area enclosed by a  $1/e$  contour then is a measure of the effective total exposed area. On the other hand, signal at a given moment is still emitted only from the instantaneous laser area. There are then two possible definitions for the number of ions in the laser region, which provides the upper limit on the number of atoms. In the absence of signal bleaching (described in Sec. 5.4), the instantaneous number of atoms exposed is a reasonable definition for the number of atoms observed. If there is large bleaching, the more conservative estimate is more appropriate. Note that the factor between instantaneous and total exposure areas depends on the laser spot size. The factor is about 4.7 for  $w_x \times w_y = 2.06 \mu\text{m} \times 2.66 \mu\text{m}$  (astigmatism compensation and aspherical lens), and about 3 for  $w_x \times w_y = 5 \mu\text{m} \times 5 \mu\text{m}$  (biconvex lens).

For imaging of single Ba atoms, the relative vibration is the measure of most concern. The vibration of the laser itself was seen to be small in this study. Vibration of the collection optics will affect the imaging resolution, but not the number of atoms being observed, or the resolution of a single atom image in a laser raster scan. The amplitude of these vibrations was minimized by stable mounting of the collection optics on large diameter posts.

## CHAPTER 4

# METHOD

Some of the methods used to produce the results in Chapters 5 and 6 are discussed in this chapter. Spectra fitting, used for separating contributions of semi-resolved fluorescence peaks, is discussed in Sec. 4.1. Background signals are discussed in Sec. 4.2 with the purpose of optimizing signal-to-background for imaging of small numbers of Ba atoms.

### 4.1. FITTING OF SPECTRA

The spectra of Ba<sup>+</sup> deposits in SXe are described in detail for green excitation (~540-590 nm) in Sec. 5.1, and for blue excitation (~460-490 nm) in Sec. 5.5. Chi-square fitting to these spectra using ROOT is described in this section. In most circumstances, the different fluorescence peaks in a spectrum overlap somewhat. Thus it was necessary to fit the fluorescence spectra with a sum of peak-specific fit functions in order to extract peak heights and integrals. Gaussians, Lorentzians and asymmetric functions were used, depending on the best match to a specific peak. Fit function parameters are not intended to determine physical properties in this thesis. Rather, fits are used to track fluorescence peak amplitudes under various circumstances, e.g., in excitation spectra (Sec. 5.1, 5.5), annealing (Sec. 5.3), and bleaching (Sec. 5.4), where components overlap spectrally. When extracting fluorescence peak amplitudes from spectra, shape parameters (centers and widths) were fixed, and amplitudes were allowed to float. Determination of those fixed shape parameters was done prior, by fitting spectra where the peak of interest is strong and letting all parameters float.

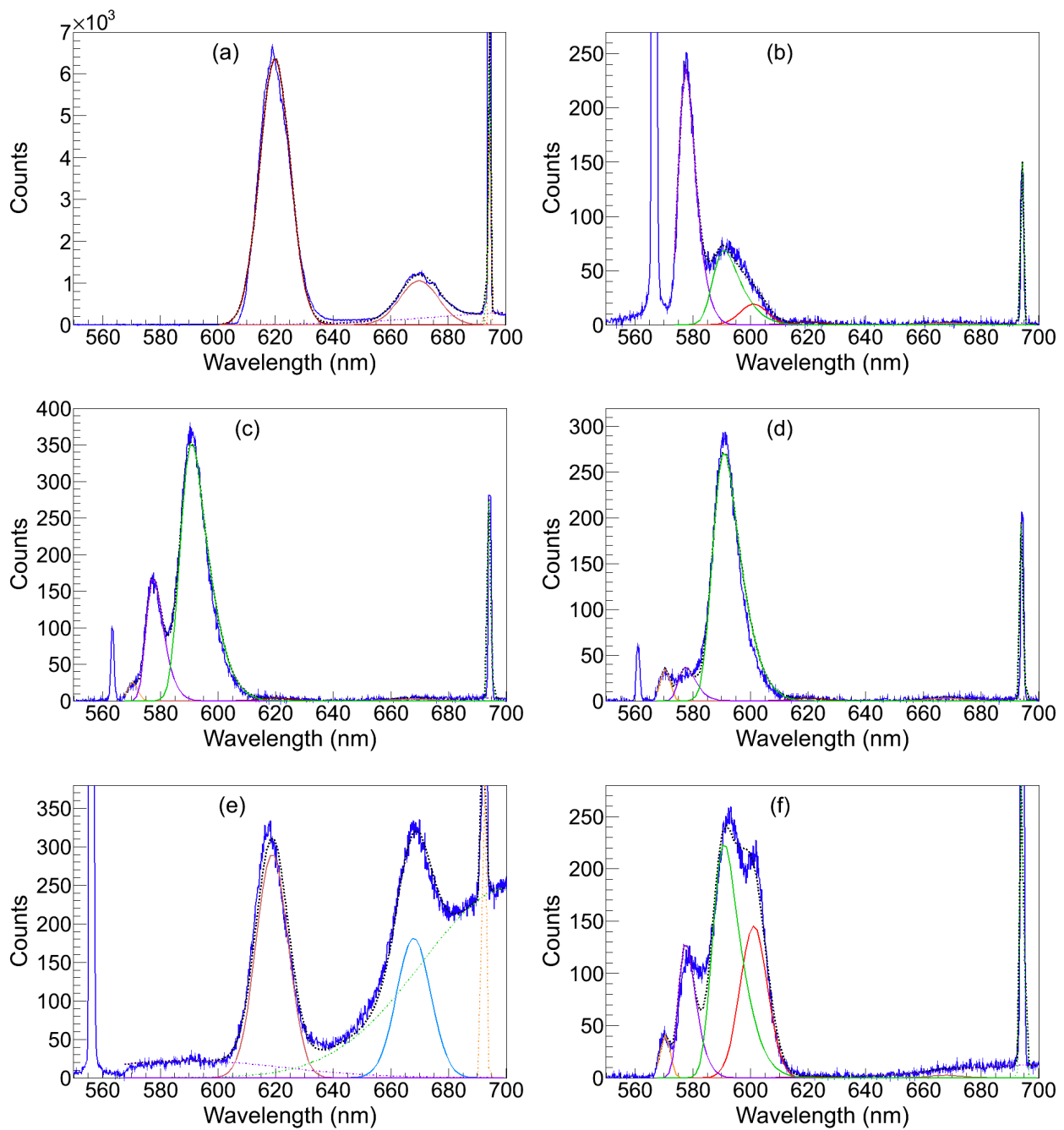


FIGURE 4.1. Example fits to spectra of  $\text{Ba}^+$  deposits with green excitation at (a) 567.3 nm, (b) 566.6 nm, (c) 563.4 nm, (d) 561.0 nm, (e) 555.9 nm (bleached), and (f) 546.3 nm. Laser scatter can be seen in the lower wavelengths for some figures, especially in (b) where it is on the edge of the Raman filter cutoff.

#### 4.1.1. FITTING SPECTRA WITH GREEN EXCITATION

Example fits to spectra for several different green excitation wavelengths are shown in Fig. 4.1. In the spectrum in Fig. 4.1e, the 570-, 577-, 591-, and 601-nm peaks have been bleached away by 165 s of 548 nm laser exposure at 3.5 mW, with laser beam radius  $w = 1000 \mu\text{m}$ , leaving the 619- and 670-nm peaks dominant (bleaching is described in Sec. 5.4). To incorporate the tail in the shape of the 577- and 591-nm peaks, an asymmetric function of the form  $A(1+\text{erf}(\frac{x-a}{\sigma_1})(1-\text{erf}(\frac{x-a}{\sigma_2}))$  was used, where  $a$  is the fixed center-defining parameter,  $\sigma_1$  and  $\sigma_2$  are fixed left and right width parameters, and  $A$  is the free amplitude parameter. The function  $\text{erf}()$  is an error function. The 570-, 601-, 619-, and 670-nm peaks were fit with Gaussian functions with fixed standard deviation ( $\sigma$ ) of 1.7 nm, 4.7 nm, 5.3 nm, and 6.7 nm, respectively. Rather than attempting frame-by-frame background subtractions, additional Gaussians were fit to the broad and sharp background fluorescence. Two broad Gaussians centered at around 590 nm and 702 nm, and one sharp Gaussian near 693 nm, were chosen by fitting spectra of Xe-only deposits. These backgrounds and their excitation spectra are discussed in Sec. 4.2. The full fit, i.e. the sum of each contributing peak fit, is the dotted black line. Though the shapes do not match perfectly for all excitation wavelengths, the fits still follow the peak amplitudes well. Ba emission and excitation spectra results are discussed in Sec. 5.1.

#### 4.1.2. FITTING SPECTRA WITH BLUE EXCITATION

Example fits to spectra for several different blue excitation wavelengths are shown in Fig. 4.2. Gaussian functions were used for the 532-, 568-, and 575-nm peaks with standard deviations ( $\sigma$ ) of 2.4 nm, 5.0 nm, and 0.7 nm, respectively. Lorentzian functions were used for the 553-, 592-, 635-, and 669-nm peaks with half width at half maxima ( $\gamma$ ) of 1.7 nm,

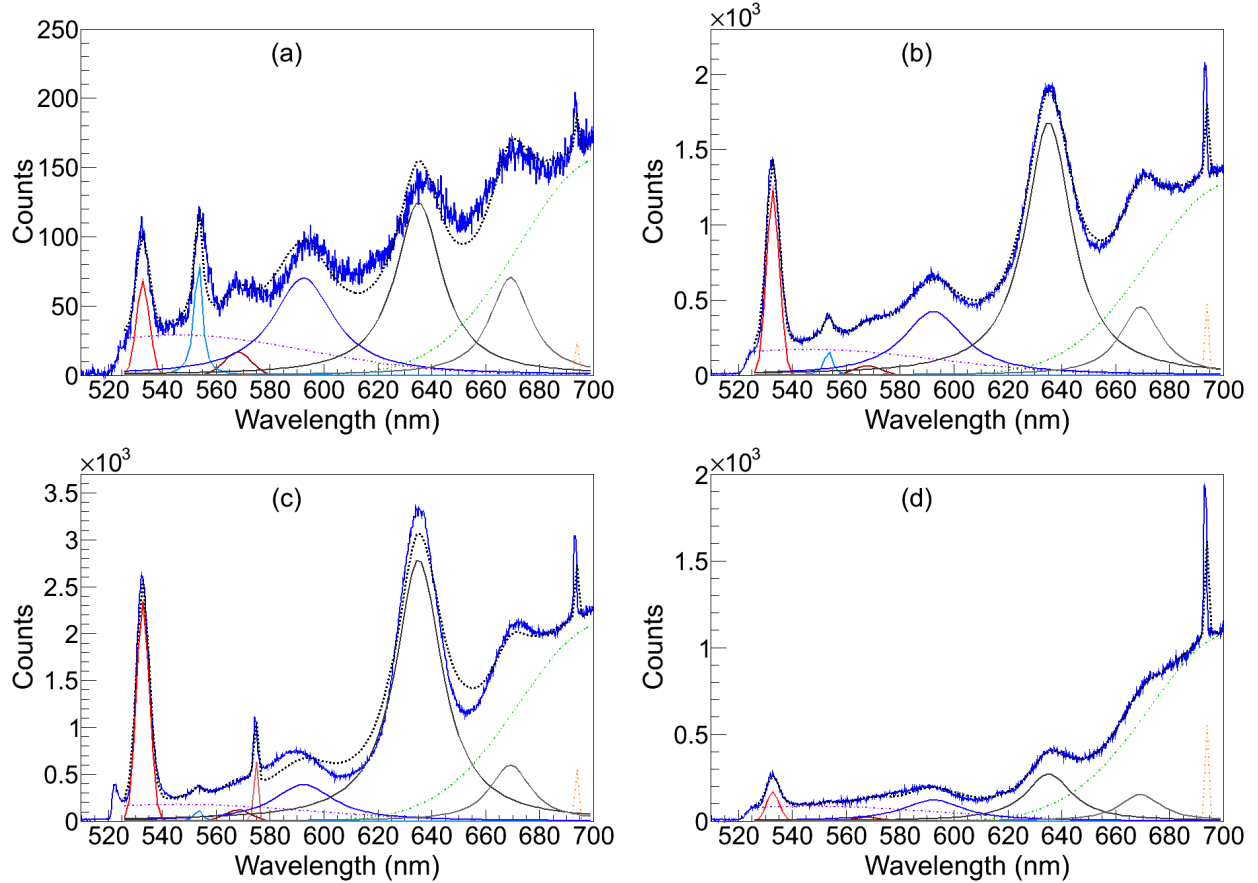


FIGURE 4.2. Example fits to spectra of  $\text{Ba}^+$  deposits with blue excitation at (a) 461.7 nm, (b) 468.2 nm, (c) 478.3 nm, and (d) 488.2 nm.

13.8 nm, 10.4 nm, and 9.1 nm, respectively. Similar to spectra with green excitation, the background components were fit with two broad Gaussians centered at 546.0 nm and 703.3 nm, with respective  $\sigma$  of 49.0 nm and 30.5 nm, as well as one sharp Gaussian centered at 693.4 nm peak with a  $\sigma$  of 0.5 nm. The fits for excitation around 478 nm (e.g., (c)) are not quite right, mainly due to a shift in the central value of the 592-nm peak. However, fit values still follow respective peaks heights well. The sharp 522- and 575-nm peaks are seen in (c), though the 522-nm peak is left out of the fitting range since it sits on the edge of the Raman filter cutoff. These spectra are discussed in Sec. 5.5.

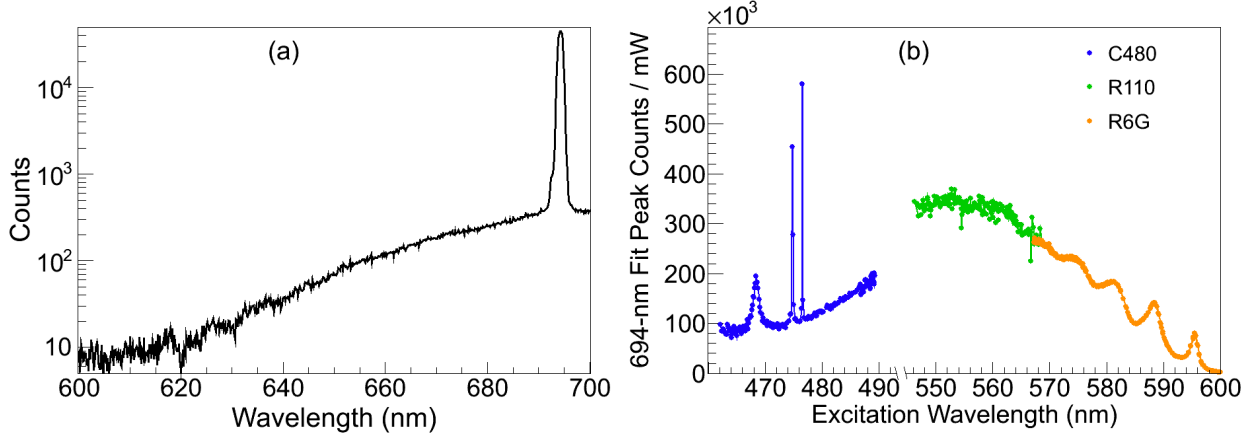


FIGURE 4.3. (a) Sapphire bulk emission with 562-nm excitation at 11 K, and (b) excitation spectrum of the sharp 693-nm emission peak using three different laser dyes. Due to different laser powers and exposure times, the R110 and R6G were scaled to match at their boundary.

#### 4.2. BACKGROUND SPECTRA

The sharp and broad background discussed in Sec. 4.1.1 is mainly due to  $\text{Cr}^{3+}$  impurity ions in the sapphire window. A spectrum of this fluorescence with 562 nm excitation is shown in Fig. 4.3a. The strong, sharp peak around 693 nm is a well-known  $^2E - ^4A_2$  emission in the  $d^3$  configuration of  $\text{Cr}^{3+}$  impurities in the sapphire bulk [43, 44]. An excitation spectrum for this peak is shown in Fig. 4.3b over the range all three dyes R6G, R110, and C480, using one of the sapphire windows with higher  $\text{Cr}^{3+}$  content. Multiple features are observed in the excitation spectrum, obtained by integrating the 693-nm peak fit (Sec. 4.1) vs. excitation wavelength. The broad absorption in the green/yellow, peaking around 550 nm, with vibrational peaks on the red tail, agree with well understood features in the spectrum of  $\text{Cr}^{3+}$  in sapphire, including three sharp peaks in the blue at 468.4, 474.8, and 476.5 nm [45, 46]. In addition to the 693-nm peak, a weaker and much broader emission is observed, along with three weak peaks in the 615-635 nm region. Excitation spectra for these fluorescence components are shown in Fig. 4.4 for the R6G dye range. In this experiment,

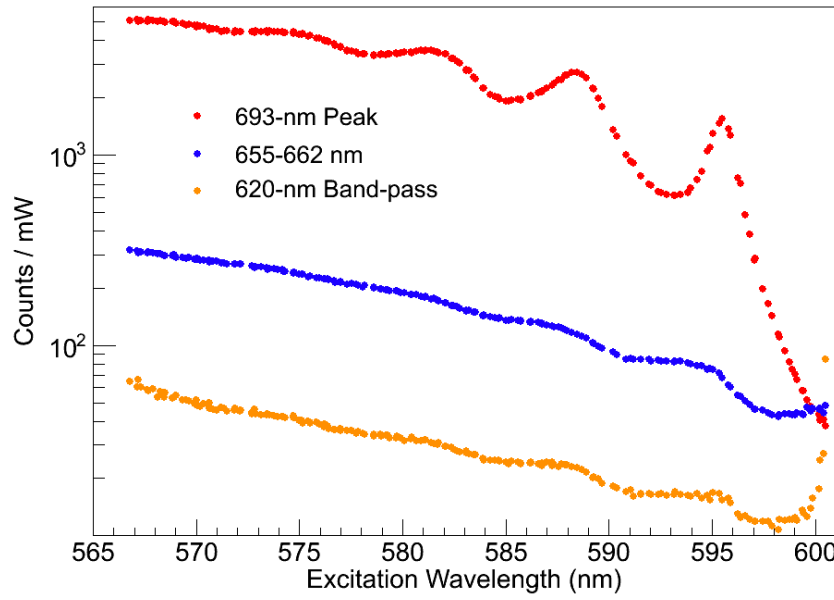


FIGURE 4.4. Excitation spectra for weaker sapphire bulk emissions (blue,orange) along with that of the strong 693-nm emission (red) at 11 K.

the laser was de-focused to about  $w = 200 \mu\text{m}$ , and the emission observed had contribution from an additional background emission from the surfaces of the window as well as from the bulk sapphire emission. The surface background is negligible for the prominent 693-nm peak. However, the rising features of the surface background excitation spectrum near 600 nm and 567 nm, discussed below, can be seen in the excitation spectra of the weaker components (blue, and especially orange curves in Fig. 4.4). Nonetheless, observation of the same vibrational peaks as in the 693-nm peak excitation spectrum demonstrates that the broad emission and weak peaks in the 620 band-pass (Fig. 4.3a) are also due to Cr<sup>3+</sup> in the sapphire. Commercially available c-plane quality sapphire windows contain low concentrations of Cr<sup>3+</sup>. Sample windows of 0.75" diameter and 0.02" thickness from a few companies were tested, and those from Meller Optics produced the lowest sapphire bulk emission in the 620-nm band-pass region.

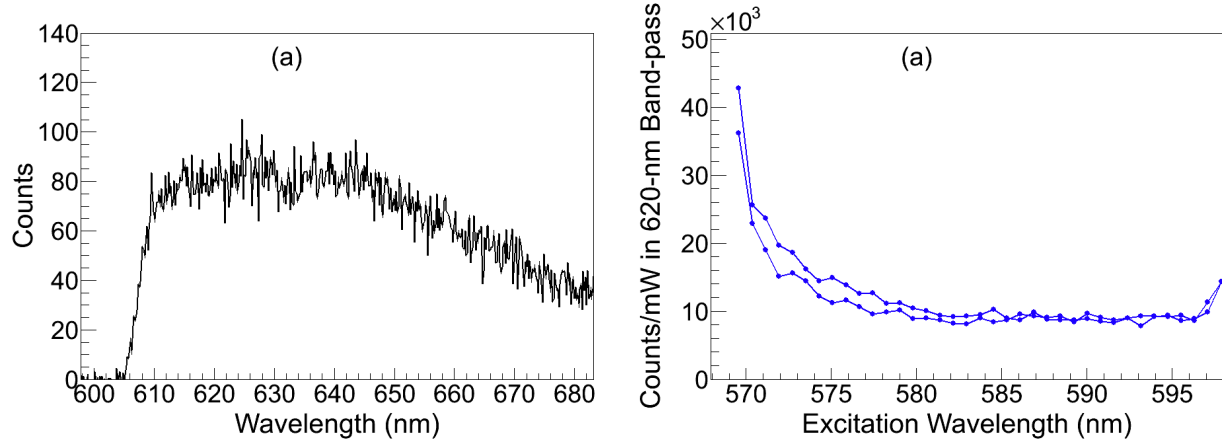


FIGURE 4.5. (a) Surface background emission spectrum w/ excitation at 570.5 nm, and (b) excitation spectrum in R6G dye range. The sharp drop in (a) around 608 nm is the Raman filter cutoff.

An additional background emission was observed from the surfaces of the window. Its broad fluorescence is shown in Fig. 4.5a with a 610-nm Raman filter cutoff and 570.4 nm excitation. Its excitation spectrum, obtained by integrating fluorescence counts in the 610–630 nm region, is shown in Fig. 4.5b over the R6G dye range. The nature of this emission has not been determined, however a few characteristics were identified. One was that the emission increased as the window temperature was decreased, down to about 100 K where it remained flat down to 11 K. This is shown in Fig. 4.6, where the “Surface + Sapphire” counts were determined by integrating a 3-pixel×3-pixel ( $15\mu\text{m}\times 15\mu\text{m}$ ) region centered on the laser spot in the image, where the laser illuminates the surface background, which includes some bulk sapphire emission as well, i.e. the broad  $\text{Cr}^{3+}$  emission passed by the 620-nm band-pass filter. “Sapphire” counts were determined by integrating a 3-pixel×3-pixel ( $15\mu\text{m}\times 15\mu\text{m}$ ) region near the center of the laser path through the sapphire bulk, thus representing the broad  $\text{Cr}^{3+}$  emission alone. This emission decreased as the window temperature was decreased, reaching a steady value below about 100 K. Another feature of the surface background is that it bleaches, i.e. is reduced during laser exposure. In order to reduce this background

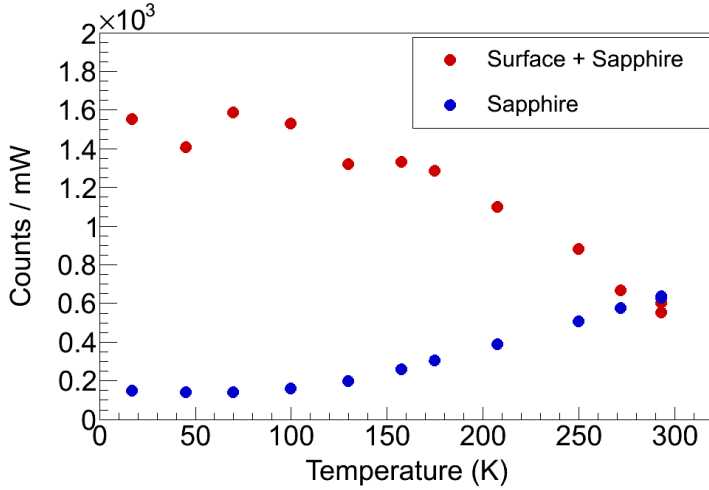


FIGURE 4.6. Temperature dependence of the surface background with some sapphire bulk contribution (red), and of the sapphire bulk emission alone (blue). Fluorescence is observed through a 620-nm band-pass filter.

in imaging experiments, as well as to reduce run-to-run variation in the background due to bleaching, the sapphire window was pre-bleached for at least half an hour at 100 K. Decay of the surface background emission from a focused laser region, with intermittent observation during a pre-bleaching process, is shown in Fig. 4.7. For efficient pre-bleaching, the dye laser was usually tuned to 580.5 nm for higher laser power ( $\sim 10$  mW), although the bleaching data in Fig. 4.7 were taken with the dye laser at 570 nm ( $\sim 0.1$  mW) with the same laser power used in typical Ba imaging experiments. During imaging experiments, frequent Xe-only deposits were made in order to track the surface background emission to establish proper background subtraction.

Consideration of signal-to-background ( $S/\sqrt{B}$ ) guided the choice of 570 nm for excitation of the 619-nm fluorescence. The signal, background, and  $S/\sqrt{B}$  passed by the 620-nm band-pass filter are plotted vs. excitation wavelength in Fig. 4.8 for both the surface background ( $B_{\text{surf}}$ ) and the sapphire bulk emission ( $B_{\text{sap}}$ ). The peak in  $S/\sqrt{B}$  represents the optimal excitation wavelength respective to each of the two background sources. Around 568.5 nm is

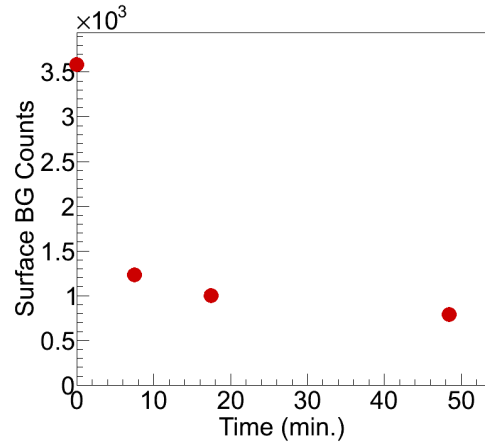


FIGURE 4.7. Decay of the surface background emission during pre-bleaching of the sapphire window.

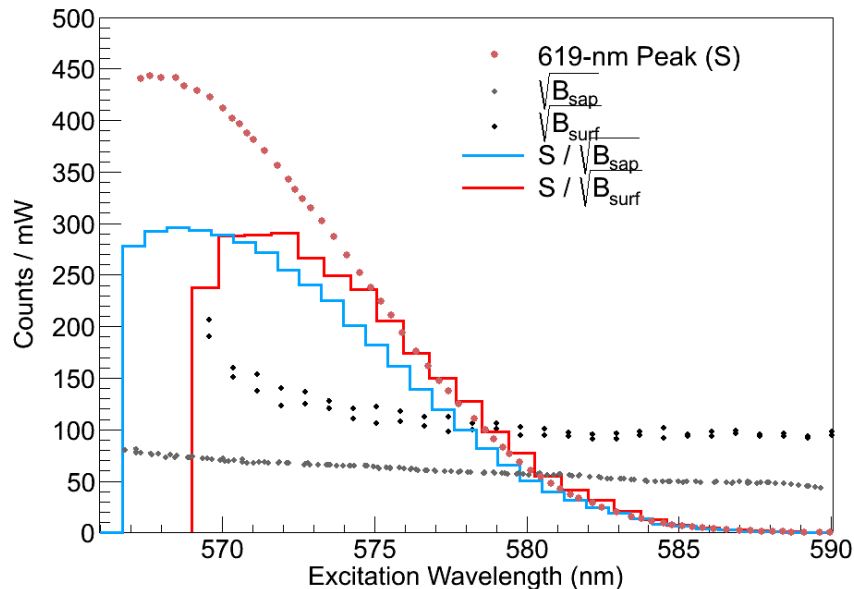


FIGURE 4.8. Optimization of signal to background with the 619-nm fluorescence signal (S) for the surface background emission ( $B_{\text{surf}}$ , red) and for the bulk sapphire emission ( $B_{\text{sap}}$ , cyan).

optimal vs. the sapphire emission, and around 571 nm is optimal vs. the surface background emission. 570 nm, which was used in sensitive imaging experiments, is nearly optimal in both cases, although 572 nm could have been used because the bulk sapphire background contribution was small in these experiments.

## CHAPTER 5

### RESULTS: SPECTROSCOPY

The spectroscopy of Ba in SXe is studied in detail beyond that reported in two previous theses [37, 38], with the goal of imaging single Ba atoms. Emission and excitation spectra are analyzed in Sec. 5.1, with particular interest in the 619-nm peak in Sec. 5.2. Studies of temperature and bleaching effects in Sections 5.3 and 5.4 aid in determining optimal conditions for observation of Ba in SXe. Finally, candidate emission lines for Ba<sup>+</sup> in SXe are discussed in Sec. 5.5.

#### 5.1. EXCITATION AND EMISSION OF BA IN SXE

Deposits of Ba in SXe absorb primarily between 540 nm and 570 nm. An absorption spectrum, obtained by observing absorption of white light by a large Ba deposit at 10 K, is shown in Fig. 5.1. Significant broadening, as well as a 4-nm redshift of the central peak, occur relative to the vacuum  $6s^2 \ ^1S_0 \rightarrow 6s6p \ ^1P_1$  absorption value of 553.5 nm. Initial absorption and emission spectra were taken with the Ba getter source [22, 37, 38], which is expected to produce neutral Ba with minimal Ba<sup>+</sup>. The emission spectrum in Fig. 5.1 was obtained by 557-nm excitation of a Ba<sup>+</sup> deposit, made at 45 K and observed at 11 K. Observation of the same 577- and 591-nm fluorescence peaks from Ba getter deposits demonstrates that these peaks are emission of neutral Ba. Therefore some neutralization of the ions takes place during the deposit [22, 37, 38]. The fraction of ions neutralized has not yet been determined.

Emission spectra, scaled by laser power, of a Ba<sup>+</sup> deposit made at 44 K and observed at 11 K are shown in Fig. 5.2a for a few different excitation wavelengths. The 577- and 591-nm peaks are clear at all three wavelengths, with varying strength. Peaks at 570 nm

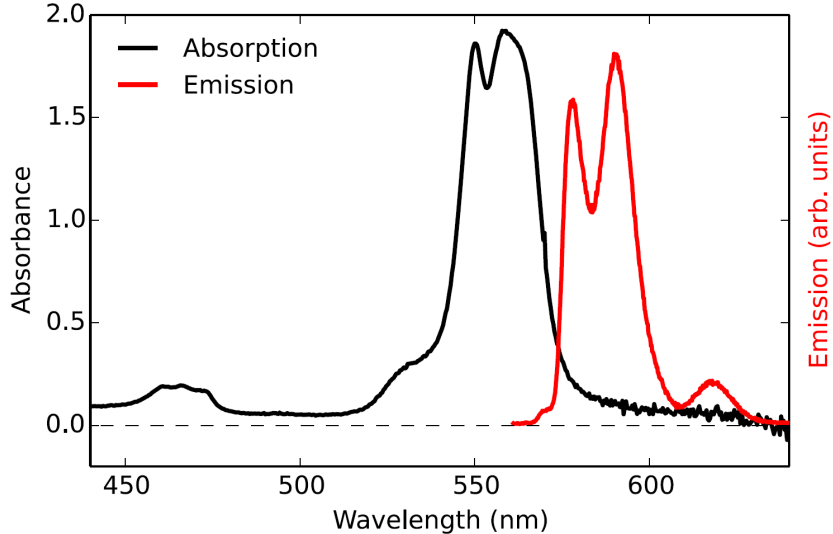


FIGURE 5.1. Absorption and emission spectra of neutral Ba in SXe. The absorption is of a Ba getter deposit at 10 K, and the emission is of a (neutralized)  $\text{Ba}^+$  deposit, deposited at 45 K and observed at 11 K with 557 nm excitation. From [22].

and 601 nm, first reported here, are both clear at 546-nm excitation. The 619-nm peak is stronger at higher wavelength, and the 670-nm peak is clear at 556-nm excitation.

Excitation spectra, shown in Fig. 5.2b, were produced by scanning the dye laser and measuring the magnitude of each fluorescence peak vs. excitation wavelength. For each frame, the spectrum was fit with a sum of peak-specific fit functions, where function shape parameters were fixed (centers and widths) and magnitudes were allowed to float. Fitting is described in Sec. 4.1.1. The dye laser power varies over the tuning range, and thus fluorescence counts at each excitation wavelength are scaled to the laser power in that frame. Since signal levels are dependent on the deposit size, the absolute scale is arbitrary. Thus, curves were scaled for visibility on the same plot. The discontinuity around 566 nm for the 619- and 670-nm peaks is the boundary between the scan range of different laser dyes. R6G dye was used for higher wavelengths and R110 for lower wavelengths. Bleaching, discussed in Sec. 5.4, was kept minimal in the 570-, 577-, 591-, and 601-nm peaks during excitation

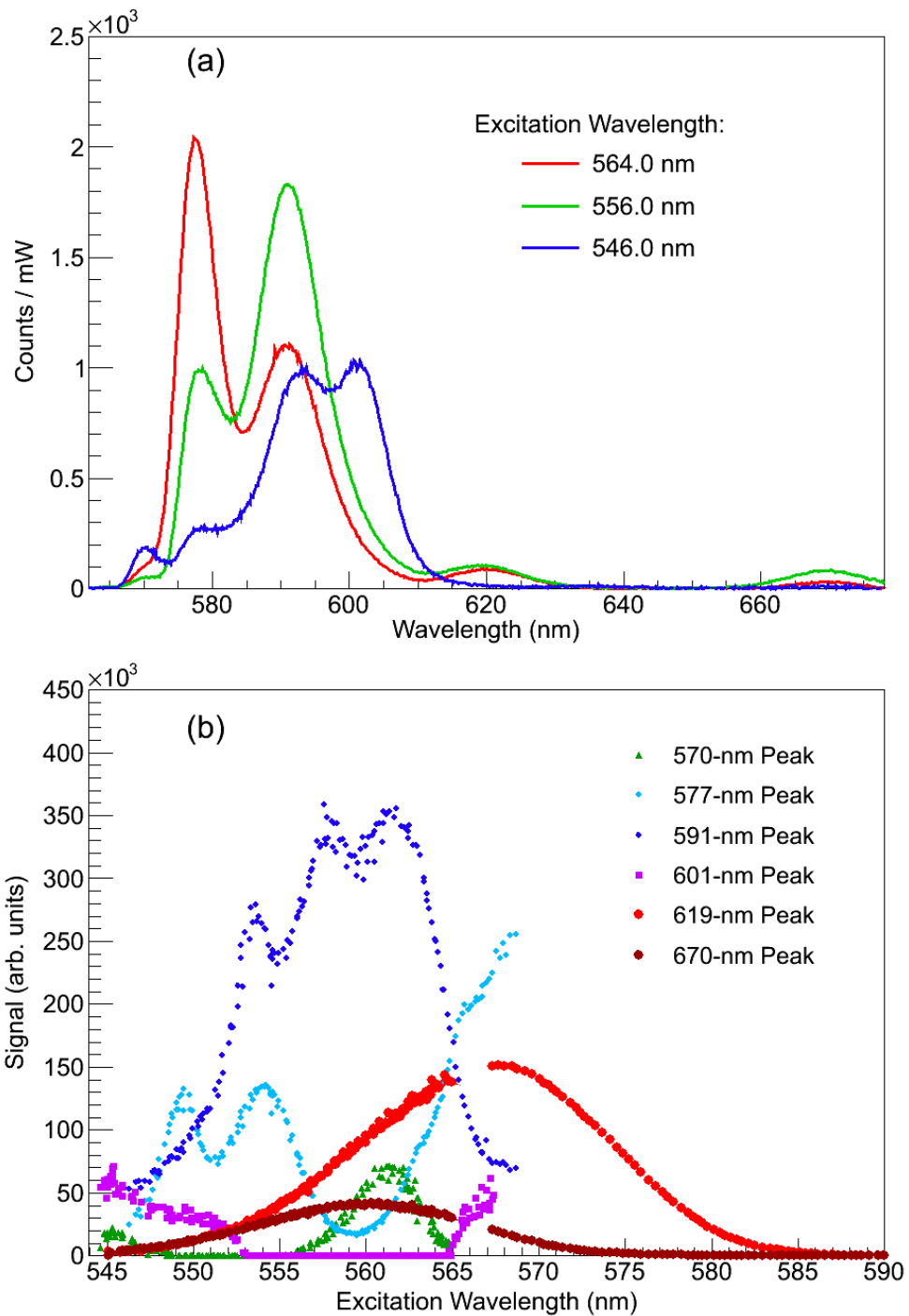


FIGURE 5.2. (a) Fluorescence spectra for a few different excitation wavelengths, and (b) excitation spectra for all observed Ba fluorescence peaks. Exposures are 1 s.

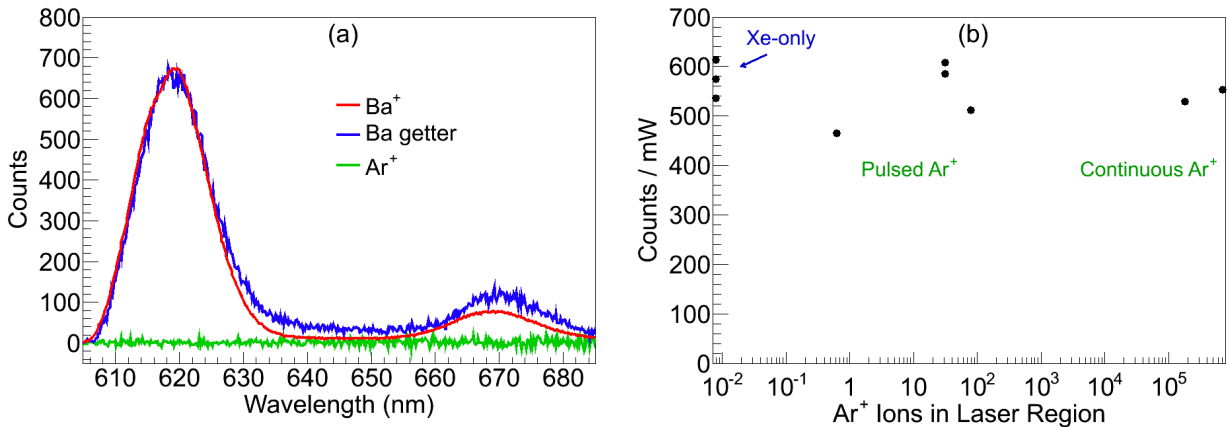


FIGURE 5.3. (a) Comparison of signal observed for deposits with the  $\text{Ba}^+$  ion beam (red), Ba getter (blue), and  $\text{Ar}^+$  ion beam (green); (b) signal through 620-nm band-pass from deposits of small to large numbers of  $\text{Ar}^+$  ions in SXe.

spectrum scans by using low laser intensities. For those peaks, maximal laser power was 0.1 mW, and the laser radius was  $w = 7$  mm with no focusing. The scans for the 619- and 670-nm peaks, which bleach only at much higher intensities, were done with the laser somewhat focused to radii of  $w = 1000 \mu\text{m}$  in the R110 dye range, and  $w = 200 \mu\text{m}$  in the R6G dye range, with maximal laser powers of 10 mW and 100 mW, respectively. Due to these different experimental conditions, the curves were scaled to match across the discontinuity.

## 5.2. 619-NM PEAK ASSIGNMENT

The 619-nm peak, as well as the 670-nm peak, was demonstrated to be related to neutral Ba by a few further tests. The spectra of a large  $\text{Ba}^+$  deposit and a deposit made with the Ba getter are compared in Fig. 5.3a. The 619-nm and 670-nm peaks are observed with both sources with similar shapes. Since the getter produces only neutral Ba, these peaks are attributed to neutralized  $\text{Ba}^+$  ions. Observation of a deposit of  $\text{Ar}^+$  of similar energy and charge in SXe is also shown in Fig. 5.3a. The lack of fluorescence in the  $\text{Ar}^+$  deposit eliminates a matrix-damage-related source of the fluorescence, such as color

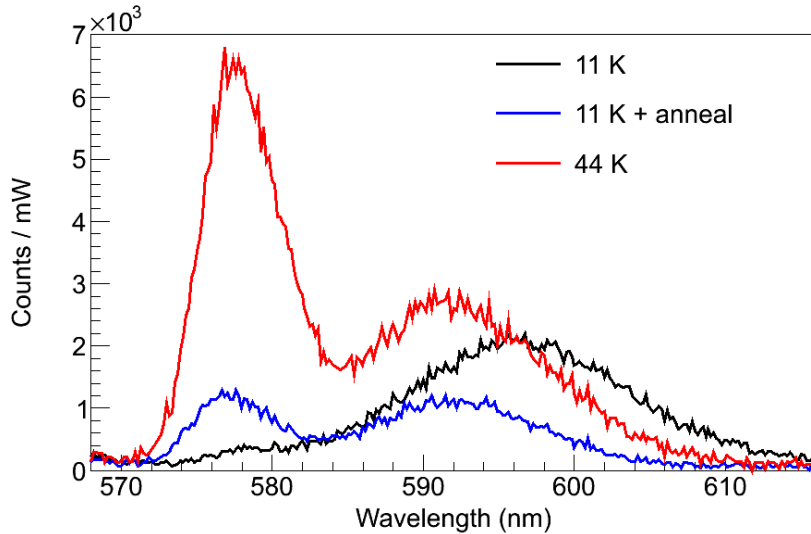


FIGURE 5.4. Spectra of peaks around 590 nm for a  $\text{Ba}^+$  deposit made at 11 K before and after annealing to 39.4 K, and one made at 44 K. All observations are at 11 K. Both  $\text{Ba}^+$  deposits are 15 s, however the 44 K deposit is scaled slightly to account for different ion current. The laser power was about 0.1 mW with an unfocused beam radius of  $w = 7$  mm, at 566 nm wavelength.

centers. Imaging experiments of  $\text{Ar}^+$  deposits were also performed, with both pulsing and continuous ion beams. Summed counts/mW from these deposits are shown to be consistent with background in Fig. 5.3b. The experimental conditions were similar to Ba imaging experiments discussed in Sec. 6.2, i.e., with focused dye laser at 570 nm, and a 620-nm band-pass filter on the fluorescence.

### 5.3. ANNEALING/TEMPERATURE DEPENDENCE

Emission spectra can depend on the thermal history of the deposit, such as the temperature at which it was made, and any annealing of the deposit (heating and re-cooling). Spectra observed at 11 K both before and after annealing are compared to that of a deposit made at 44 K and observed at 11 K in Fig. 5.4. Peak shapes in the annealed deposit look similar to those in the deposit made at 44 K. However, larger signal is observed in the deposit at 44 K. The broader emission peaking around 596 nm in non-annealed 11-K deposits may

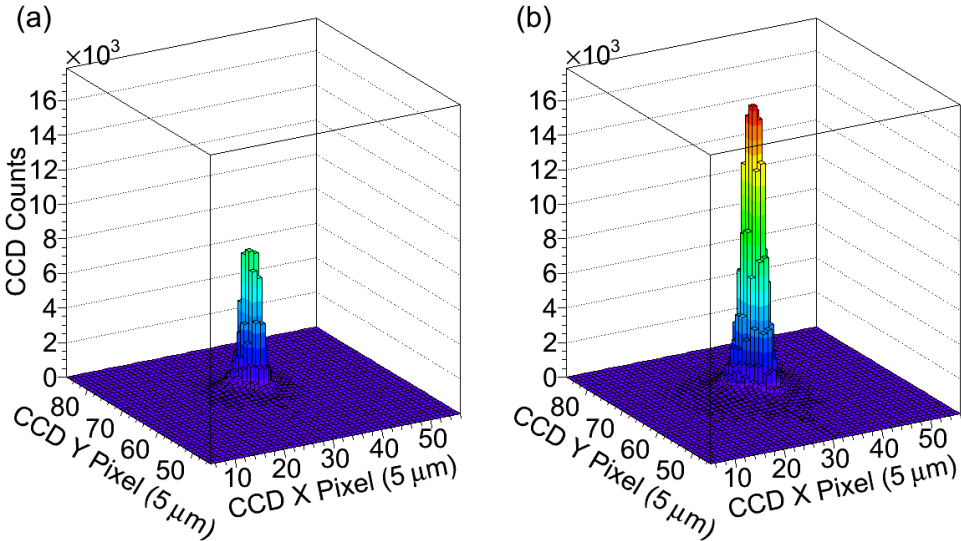


FIGURE 5.5. Images of 619-nm fluorescence with a focused 570-nm laser for deposits made at (a) 11 K and (b) 52 K. Deposits are 3 s of continuous  $\text{Ba}^+$  current. Exposures are 0.1 s. Observation was at 11 K.

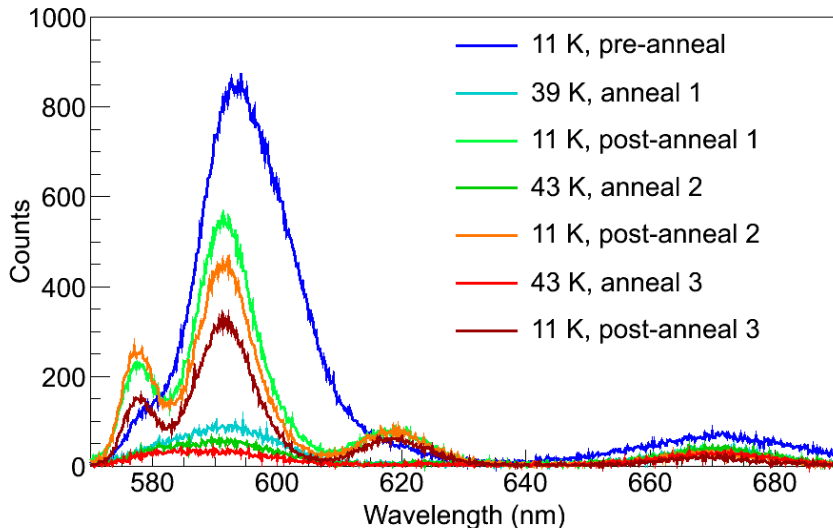


FIGURE 5.6. Spectra of a large  $\text{Ba}^+$  deposit through several annealing cycles. The initial deposit was at 11 K. The laser power was about 0.2 mW with an unfocused beam radius of  $w = 7$  mm, at 564 nm wavelength. [22]

be due to a higher population of the 601-nm peak, which is not resolved from the 591-nm peak. The deposit temperature dependence of the size of the 619-nm peak is illustrated by images comparing the fluorescence from a focused laser through the 620-nm band-pass filter, shown in Fig. 5.5. The level of 619-nm signal is about 3 times larger in deposits made at

52 K vs. 11 K. Imaging is described in detail in Chapter 6. These tests guided the standard of depositing at  $50\pm 5$  K when observing the 577-, 591-, and/or 619-nm peaks.

Fluorescence spectra with 564 nm excitation through several annealing cycles for a deposit made at 11 K are shown in Fig. 5.6. The initial exposure shows significant 591- and 601-nm (unresolved from one another) emission, with some 577-nm emission. All peaks are reduced at the high temperature ends of the anneal cycles. The return to lower temperatures results in an overall increase in the 577- and 619-nm peaks, and an overall loss of the 670-nm peak.

Fit peak counts (fitting is described in Sec. 4.1) vs. temperature are shown in Fig. 5.7. The 577- and 619-nm peaks gained significantly with the first anneal, suggesting that they are due to more stable matrix sites. Both of these peaks remained about the same after the second cycle (small gain in 577-nm), and both had loss after the third cycle, which reached the higher temperature of 48 K. The 591-nm had moderate loss with each cycle. The 601-nm peak had nearly complete loss in the first anneal cycle. The 670-nm peak had significant loss, with more loss after each succeeding anneal cycle, each of which reached higher a temperature than the last.

Aside from matrix site changes, the temperature dependence of fluorescence can be observed in the annealing cycles. The 577-, 591- and 619-nm peaks have their highest amplitude at 11 K. The 577-nm and 619-nm peaks reach a plateau at 11 K, while the 591-nm peak may benefit from even lower temperatures. This suggests that a probe in nEXO may need to be extracted from the liquid chamber and moved to a separate evacuated chamber in order to cool to 11 K or below for most efficient observation.

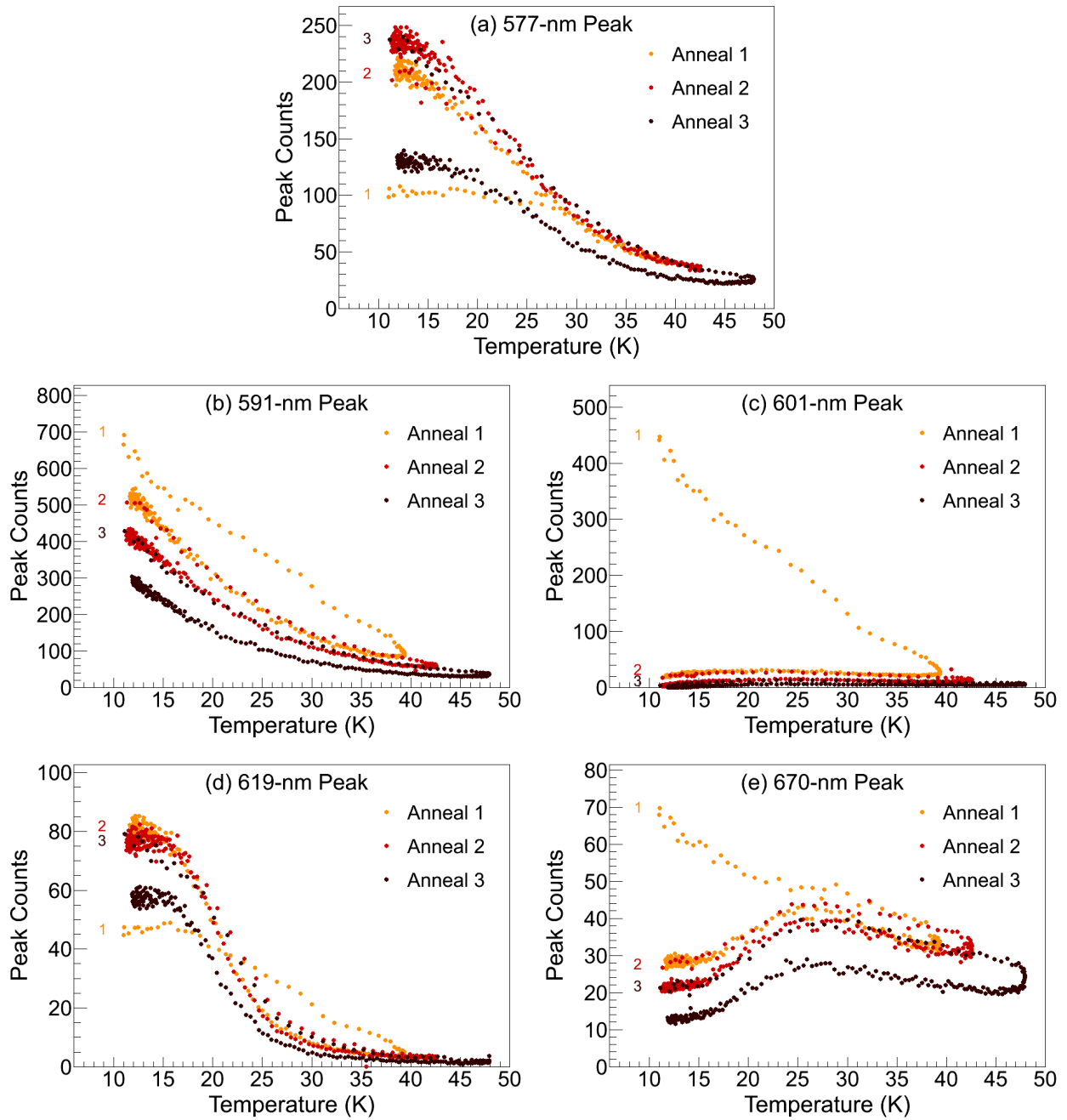


FIGURE 5.7. Fit peak counts for the (a) 577 nm, (b) 591 nm, (c) 601 nm, (d) 619 nm, and (e) 670 nm fluorescence peaks through three annealing cycles of the Ba<sup>+</sup> deposit made at 11 K. “1”, “2”, and “3” mark the beginning of each anneal cycle. The laser power was about 0.2 mW with an unfocused beam radius of  $w = 7$  mm at 564 nm wavelength.

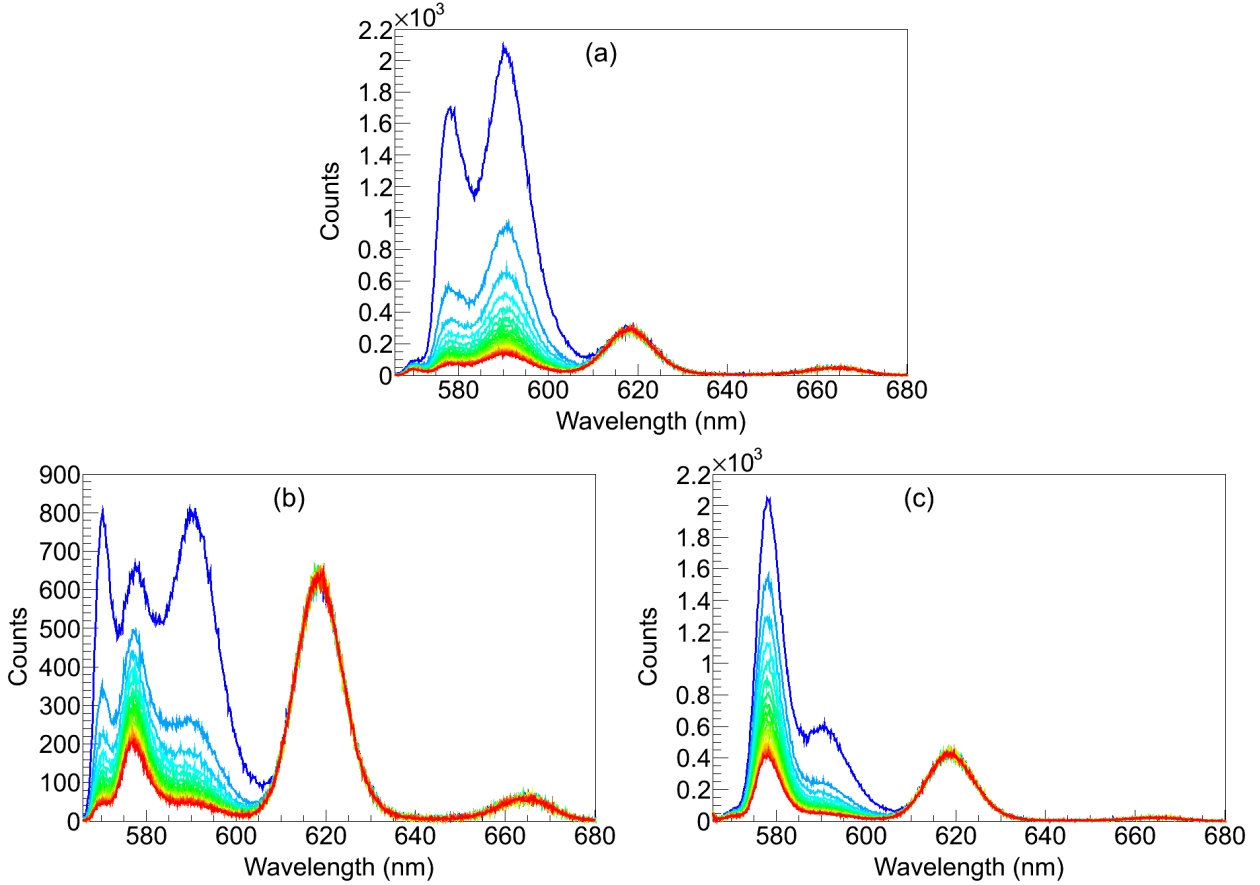


FIGURE 5.8. Bleaching of Ba spectra with excitation at (a) 556.9 nm, (b) 562.6 nm, and (c) 566.3 nm. Laser power and exposure times are (a) 1.3 mW and 1 s, (b) 7.5 mW and 0.2 s, and (c) 5.8 mW and 0.2 s. Every tenth exposure is shown, beginning with the 2<sup>nd</sup> in the darkest blue, ending with the darkest red. Each is a 5-s continuous Ba<sup>+</sup> deposit at 45 K, observed at 11 K. [22]

#### 5.4. BLEACHING

Loss of emission with laser exposure, or bleaching, was observed for all six Ba fluorescence peaks. Examples of bleaching spectra are shown in Fig. 5.8, with excitation at (a) 556.9 nm, (b) 562.6 nm, and (c) 566.3 nm, using a semi-focused laser of radius  $w = 1000 \mu\text{m}$ . Each curve is the Ba emission spectrum at different points in time. Bleaching is seen to be rapid for the 570-, 577-, 591-, and 601-nm peaks. Negligible bleaching is observed for the 619- and 670-nm peaks in Fig. 5.8. Nevertheless, even for these lines, some small bleaching was observed with the much higher intensity of a focused beam.

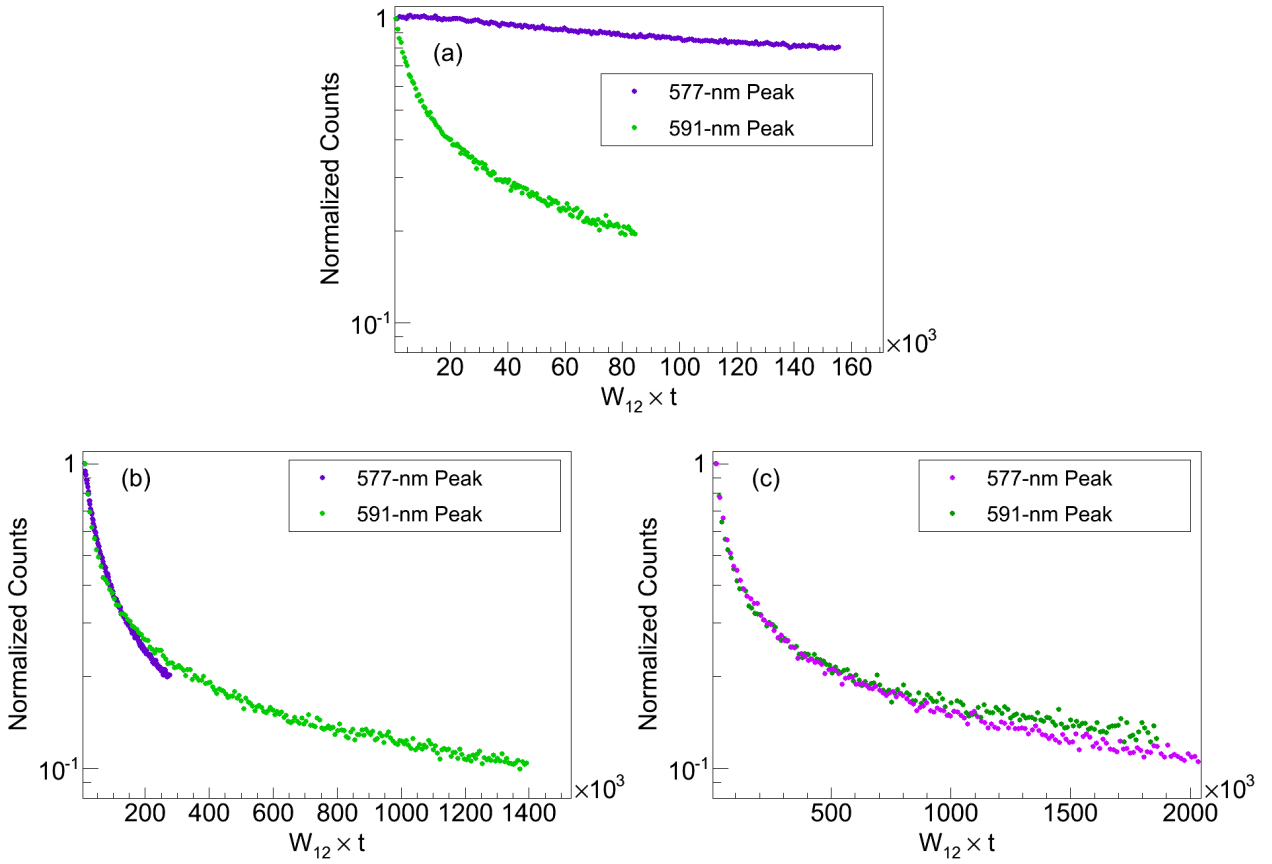


FIGURE 5.9. Normalized fluorescence vs. calculated number of excitations with laser intensity around (a) 0.3, (b) 3.7, and (c) 43 mW/mm<sup>2</sup>, for the 577-nm (purple) and 591-nm (green) fluorescence peaks. The excitation wavelength was 566.3(562.6) nm for the 577(591)-nm peak. The deposits were continuous Ba<sup>+</sup> beam at 45 K and observed at 11 K. The exposure times were 0.2 or 2 s.

#### 5.4.1. BLEACHING OF THE 577- AND 591-NM PEAKS

The integrated counts for different peaks in each spectrum were determined by fits to the spectra, as described in Sec. 4.1. Integrated counts, normalized to the initial points, vs. calculated number of excitations ( $W_{12} \times t$ ) are shown in Fig. 5.9 for both the 577-nm (purple) and 591-nm (green) fluorescence peaks, with laser intensities of about (a) 0.3 mW/mm<sup>2</sup>, (b) 3.7 mW/mm<sup>2</sup>, and (c) 43 mW/mm<sup>2</sup>. The excitation wavelengths used were 566.3 nm for the 577-nm peak and 562.6 nm for the 591-nm peak. Initially there is a more rapid exponential decay, which levels off to a slow decay after a few hundred thousand excitations. Bleaching

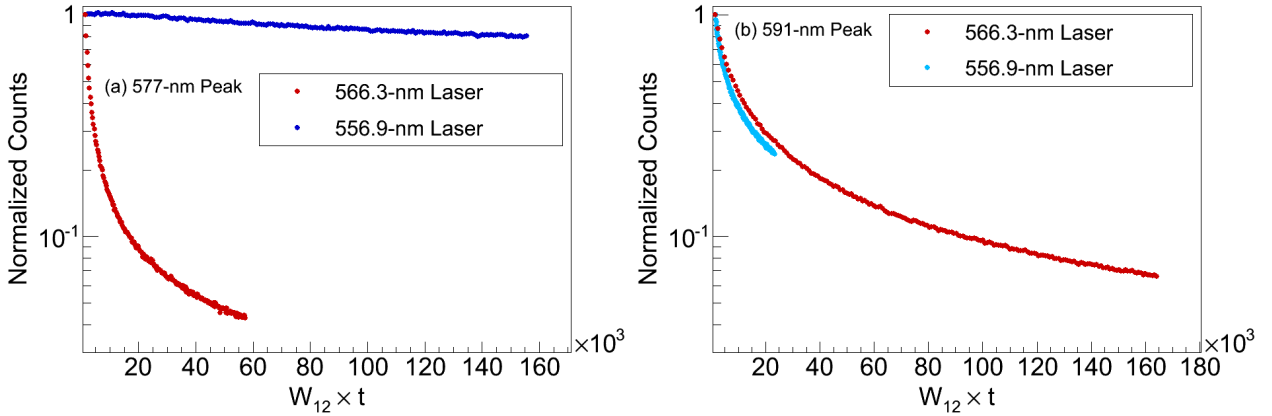


FIGURE 5.10. Normalized fluorescence vs. calculated number of excitations with different excitation wavelengths for (a) the 577-nm peak, and (b) the 591-nm peak. Deposits are continuous  $\text{Ba}^+$  at 45 K, observed at 11 K.

is more rapid in the 591-nm peak than the 577-nm peak when low intensity is used (a). For medium (b) and high (c) intensity, bleaching rates are similar. In order to calculate the excitation rate  $W_{12}$  for each run according to Eq. 8 (Chapter 2), the cross section  $\sigma(\nu)$  was calculated using the integral of the corresponding excitation spectrum (Fig. 5.2), as explained in Sec. 2.4. Peak excitation cross sections were calculated to be  $5.2 \times 10^{-15} \text{ cm}^2$  for the 577-nm emission peak, and  $3.4 \times 10^{-15} \text{ cm}^2$  for the 591-nm emission peak. Lower values of  $\sigma$  were used for off-peak excitation, according to the excitation spectra.

Comparisons of bleaching with different excitation wavelengths are shown in Fig. 5.10 for (a) the 577-nm peak, and (b) the 591-nm peak. In the case of the 577-nm peak (a), the excitation wavelengths (566.3 and 556.9 nm) correspond to different peaks in the excitation spectrum (Fig. 5.2). Very different bleaching rates were observed. In the case of the 591-nm peak (b), the excitation wavelengths (562.6 and 556.9 nm) correspond to neighboring peaks in the triplet structure of the excitation spectrum. The bleaching rates are similar, with a somewhat faster rate for the 556.9-nm excitation.

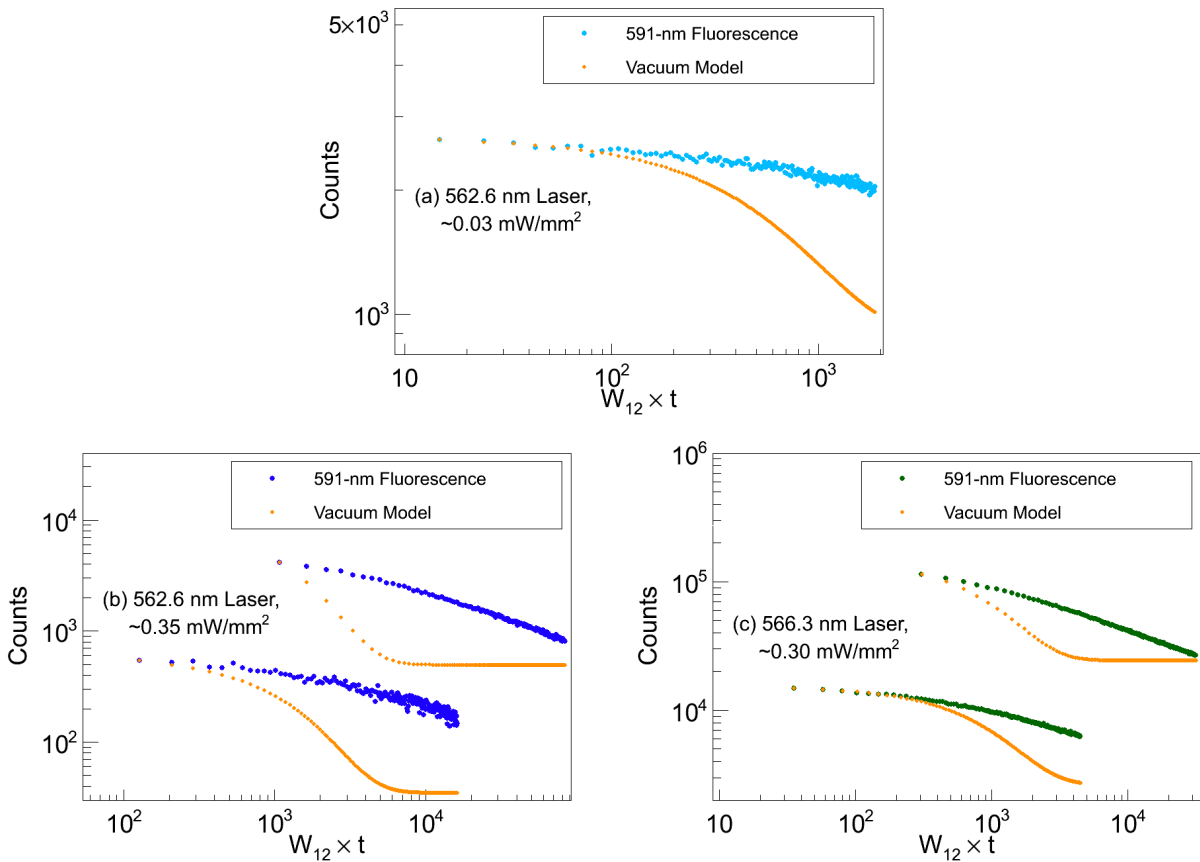


FIGURE 5.11. Vacuum model (orange) comparisons to 591-nm fluorescence with excitation at 562.6 nm (a,b), and 566.3 nm (c). Exposure times were (a) 0.2 s, (b) 0.2 and 2 s (two curves), and (c) 0.2 and 2 s (two curves). Deposits were continuous Ba<sup>+</sup> at 45 K, observed at 11 K.

Ultimately, these studies suggested that the 577-nm peak may be better than the 591-nm peak to use in imaging small numbers of atoms due to its lower bleaching rate, especially with excitation on the high-wavelength end of the range studied (Fig. 5.10a), and at low intensity (Fig. 5.9a). Imaging of Ba atoms using a combination of the 577- and 591-nm peaks with excitation at 566 nm, via a band-pass filter passing 573 - 599 nm FWHM, is discussed in Sec. 6.1.

A numerical model of fluorescence vs. time for a 5-level system of Ba in vacuum is described in Sec. 2.2. Using the Ba vacuum transition parameters given in Table 2.1, the model is compared to bleaching data of the 591-nm peak in Fig. 5.11. The  $W_{12}$  used in

each model is the same as described above. Each model is normalized to the beginning of its respective data set. Agreement between the model and data is observed for the first  $\sim 100$  excitations with on-resonance 562.6-nm excitation at low laser power (a), at which point the vacuum model begins more rapid decay. With the same 562.6-nm excitation and 10 times the laser power (b), where the first point is above 100 excitations, this deviation begins immediately. With the off-resonance excitation wavelength of 566.3 nm (c), the model agrees with data for the first  $\sim 200$  excitations. The less rapid decay in the data vs. the model between  $\sim 100$ -200 and  $\sim 5,000$  excitations indicates a lower optical pumping rate in the SXe vs. in vacuum. In the model, a steady state level is reached beyond  $\sim 5,000$  excitations. In contrast, data slowly decays, and some bleaching continues even beyond  $10^4$  excitations. Overall, the model with vacuum parameters describes the initial bleaching rate well, before substantial bleaching has occurred. Beyond this region, modification of rates is needed to accurately match the data.

The fluorescence efficiency  $\epsilon_f$  is the total number of photons emitted per photon absorbed (Sec. 2.4). It can be calculated by Eq. 13 (Chapter 2) if Ba density,  $W_{12}$ , and photon detection efficiency are known. This was measured in the first of exposure, before substantial bleaching has occurred, and is plotted vs.  $W_{12}$  in Fig. 5.12 for the 577- and 591-nm peaks. The fluorescence efficiency is fairly constant below  $W_{12} \approx 400 \text{ s}^{-1}$ , and begins to decline at higher  $W_{12}$ . This may be due to the effect of greater bleaching at higher  $W_{12}$  in the first exposure. Using the lowest values of  $W_{12}$ ,  $\epsilon_f$  is measured to be about  $3.1 \times 10^{-4}$  for the 591-nm peak with 562.6-nm excitation, and  $6.7 \times 10^{-5}$  for the 577-nm peak with 566.3-nm excitation. Modifications to the bleaching model have not been found which can explain

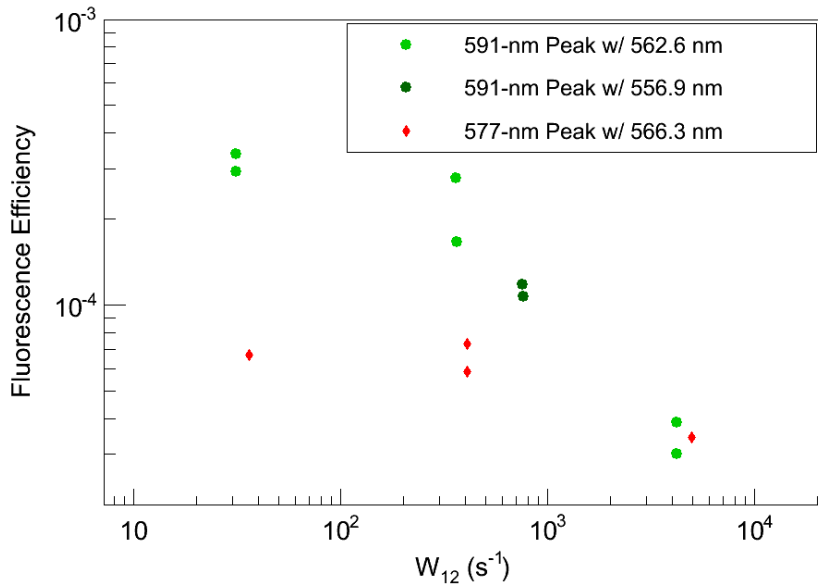


FIGURE 5.12. Fluorescence efficiency vs.  $W_{12}$  using the first exposure frame for the 577-nm (red) and 591-nm (green) peaks. The deposits are 5 s continuous  $\text{Ba}^+$  made at 50 K and observed at 11 K with laser radius  $w = 1000 \mu\text{m}$ .

such small fluorescence efficiency. However, these values assume that 100% of deposited  $\text{Ba}^+$  ions are observable as Ba atoms by these fluorescence peaks, which may not be the case.

#### 5.4.2. BLEACHING OF THE 619-NM PEAK

On the scale of the laser intensity in Fig. 5.8, the 619-nm peak does not bleach at all. Only at higher laser intensities does it bleach at noticeable levels, e.g. a few mW of focused 570-nm laser excitation. This indicates a significant deviation from the vacuum model for Ba atoms in this matrix site. In particular, to avoid optical pumping, decays from D states must be competitive with decays into D states. Bleaching curves for 619-nm fluorescence, where counts are integrated from the image of a focused laser region with  $w_x \times w_y = 2.06 \mu\text{m} \times 2.66 \mu\text{m}$ , are plotted vs. number of excitations in Fig. 5.13 for three laser powers. The excitation rate  $W_{12}$  incorporates the calculated cross section for the 619-nm peak,  $3.1 \times 10^{-15} \text{ cm}^2$ . Even with the higher laser power of 0.61 mW, 70% of the signal

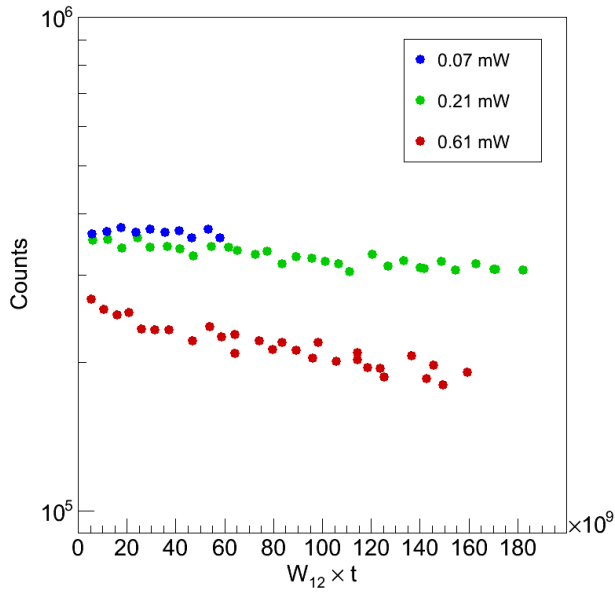


FIGURE 5.13. 619-nm fluorescence counts vs. number of excitations for three laser powers. Excitation is at 570 nm, focused to  $w_x \times w_y$  beam radii of  $2.06 \mu\text{m} \times 2.66 \mu\text{m}$ . All curves are for one deposit of 5 s continuous  $\text{Ba}^+$  at 50 K, observed at 11 K from low to high laser power. Exposure times are 3, 1, and 0.3 s for the 0.07, 0.21, and 0.61 mW laser powers, respectively, resulting in a similar number of excitations per frame.

remains after  $160 \times 10^9$  excitations, about nine orders of magnitude beyond the bleaching of the 577- and 591-nm peaks.

### 5.5. BLUE EXCITATION / CANDIDATE $\text{BA}^+$ LINES

Blue excitation of  $\text{Ba}^+$  in SXe was first explored in the thesis of Shon Cook. A set of sharp emission peaks were observed at 522, 575, 637, 712, and 814 nm, in decreasing emission strength. These peaks were attributed to emission from different vibrational states of a molecule composed of Ba and one or more H atoms, that is denoted as  $\text{BaH}_x$  [37]. This assignment is supported by two additional experiments in this thesis. First, a reduction of those peaks is observed in deposits made at 50 K, well above the  $\text{H}_2$  freezing temperature of 12 K, vs. deposits made at 11 K, as shown in Fig. 5.14a. Freezing of  $\text{H}_2$  along with the Xe will result in higher concentration of  $\text{H}_2$  in the matrix. Second, the peaks are much stronger

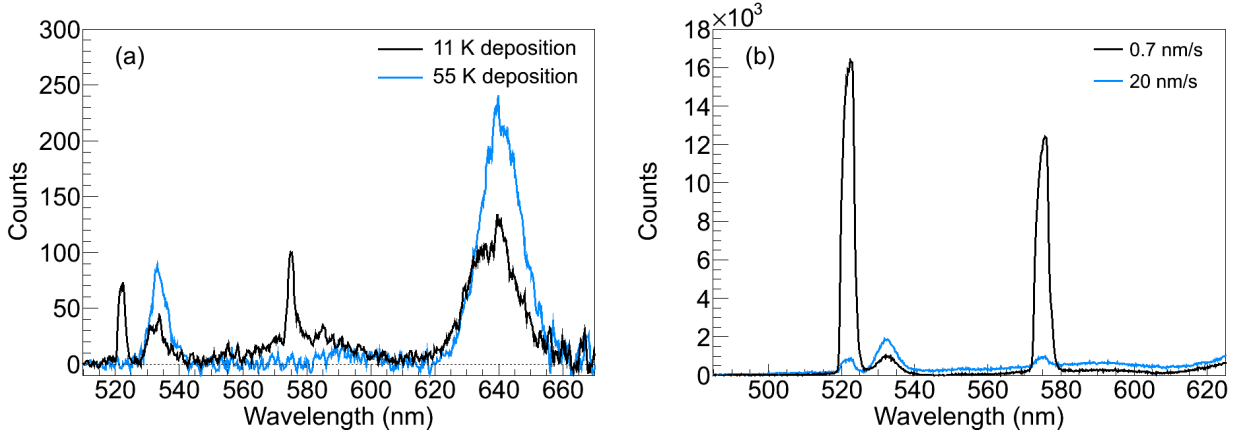


FIGURE 5.14. Comparison of Ba<sup>+</sup> deposits made at (a) 55 K vs. 11 K, and (b) SXe deposition rate 20 nm/s vs. 0.7 nm/s.[22]

in deposits made with lower leak rates, as shown in Fig. 5.14b, for deposits made at 11 K. The lower leak rate results in a higher relative concentration in the SXe matrix of H<sub>2</sub> from residual gas in the vacuum system. In both cases, with reduced H<sub>2</sub> concentration, the sharp peaks at 522 nm, etc. are reduced significantly.

Several additional emission peaks are prominent in deposits made at 50±5 K and observed at 11 K. Representative spectra at four blue excitation wavelengths are shown in Fig. 5.15a. Peaks at 532, 553, 568, 592, 635, and 669 nm are observed. Excitation spectra for these peaks are shown in Fig. 5.15b. The largest peaks at 532 nm and 635 nm have similar excitation spectra, indicating that they are due to the same excitation transition. One possible assignment is that the 532- and 635-nm peaks are emission from the P → S and P → D transitions, respectively, of matrix-isolated Ba<sup>+</sup> ions. However, matrix effects on the relative emission rates would need to be responsible for the higher number of counts observed in the 635nm peak vs. the 532-nm peak. In contrast, the P → S transition is about 4 times more likely than the P → D transition in vacuum. Further study of these emission peaks is needed to assign them to Ba<sup>+</sup>, e.g. by comparing Ba<sup>+</sup> deposits to deposits made with a Ba getter.

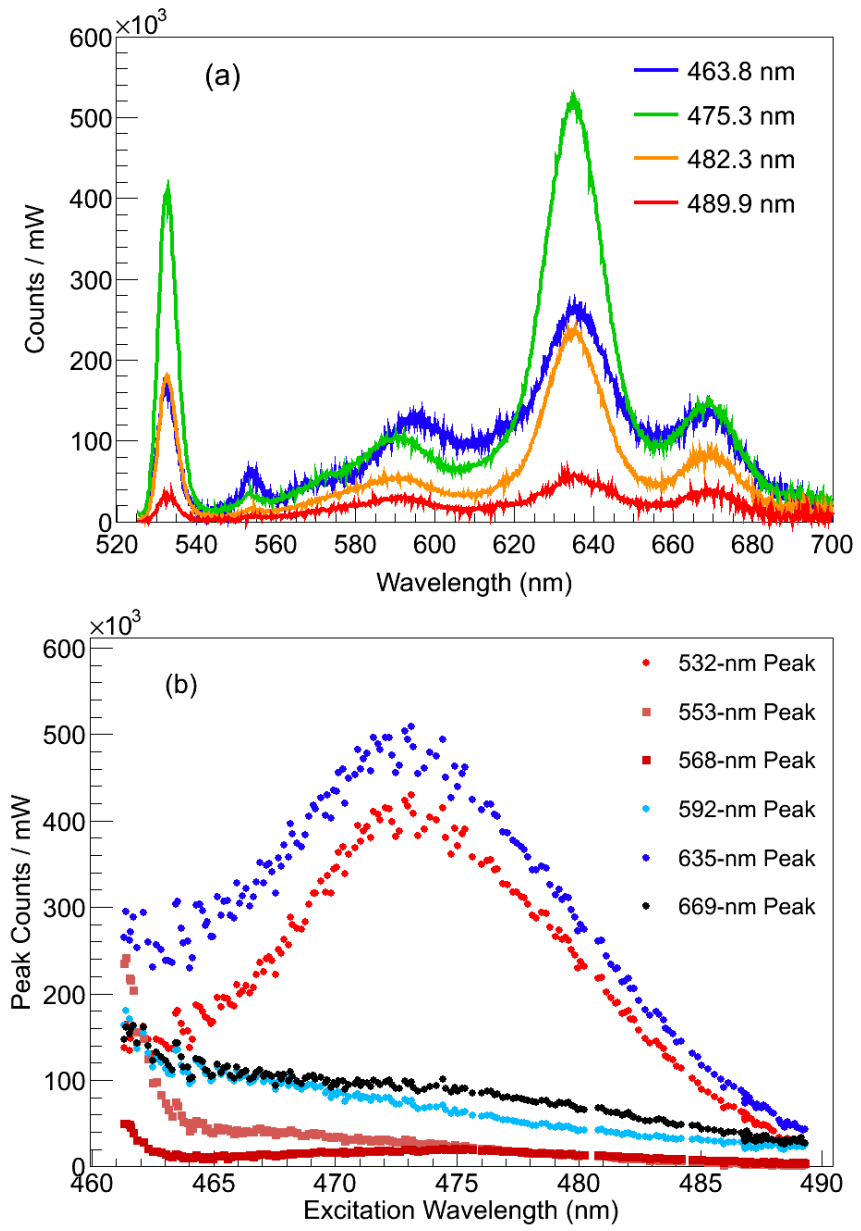


FIGURE 5.15. (a) Fluorescence spectra for several excitation wavelengths, and (b) excitation spectra for peaks observed through the C480 dye range. [22]

## CHAPTER 6

### RESULTS: IMAGING

Results from Ba spectroscopy presented in Chapter 5 were used to determine the best conditions for imaging small numbers of Ba atoms in SXe. Optimum excitation wavelengths were determined by studying the excitation spectra of the signal as well as the background. Bleaching studies determined optimum laser intensity to be used. Deposits made at  $50 \pm 5$  K produced more Ba fluorescence signal than those made at 11 K. Based on these considerations, an image of Ba atoms emitting at 577 and 591 nm is presented in Sec. 6.1 at the level of  $\leq 2200$  atoms instantaneously exposed. Images of Ba atoms emitting at 619 nm down to the single-atom level are then presented in Sec. 6.2.

#### 6.1. IMAGING 577- AND 591-NM FLUORESCENCE

First attempts at imaging small numbers of Ba atoms in a focused laser region were done with the 577- and 591-nm Ba fluorescence peaks together using a 586-nm band-pass filter, which passes 573 - 599 nm FWHM. This filter has a 2" diameter, resulting in a nominal collection efficiency of  $1.8 \times 10^{-2}$ , four times the efficiency given in Table 3.1. An image of  $\leq 2200$  atoms instantaneously in the laser region (see Sec. 3.1.5 for calibration of ion deposit) is shown in Fig. 6.1 for a 100-s exposure with  $0.03 \mu\text{W}$  of 566-nm excitation. The laser was focused by the bi-convex lens, resulting in a beam radius of  $5 \mu\text{m}$ , as discussed in Sec. 3.4. With this spot size, the factor between total and instantaneously exposed atoms is 3, as discussed in Sec. 3.7, resulting in  $\leq 6600$  total atoms exposed. At this low intensity, little bleaching was observed in the four frames observed (frame 1 is shown). Groups of 9 ( $3 \times 3$ ) CCD pixels have been binned in software to produce the peak shown. Detection of

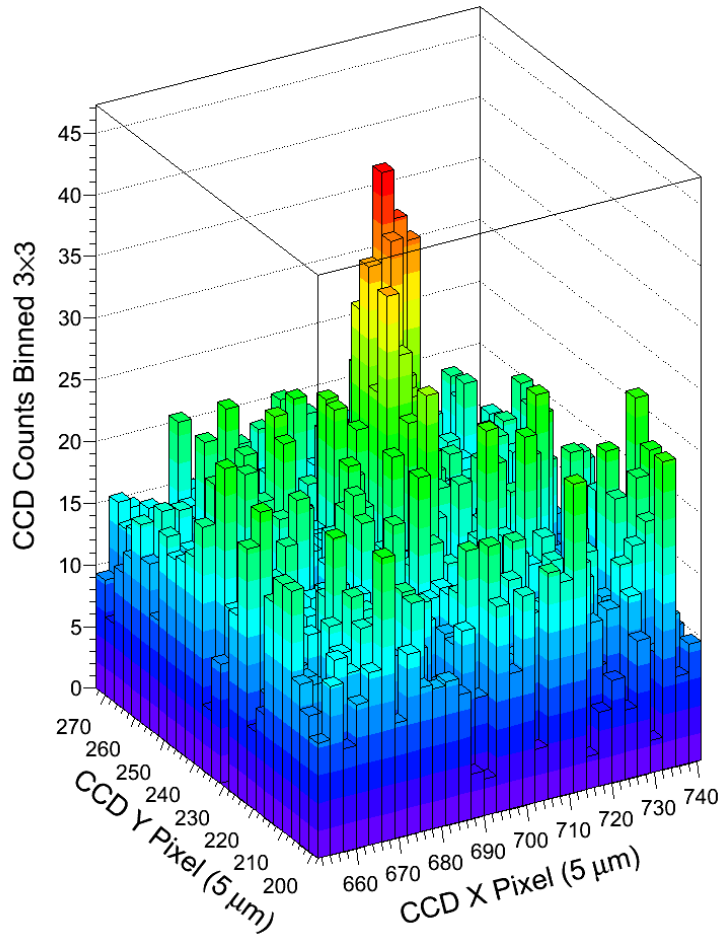


FIGURE 6.1. Image through a 586-nm band-pass filter of  $\leq 2200$  Ba atoms in SXe. The exposure was 100-s with  $.03 \mu\text{W}$  of 566 nm excitation, with a laser beam radius of  $w = 5 \mu\text{m}$ . The sample was deposited at 50 K and observed at 11 K.  $3 \times 3$  pixel binning was done with software.

single Ba atoms in these sites will require higher laser power to get more photons per atom. To overcome bleaching at higher intensity, several re-pump lasers may be needed. As a result of low total exposure, neither the sapphire nor the surface backgrounds are present in these images.

## 6.2. IMAGING 619-NM FLUORESCENCE

The 619-nm peak has orders of magnitude less bleaching than the 577- and 591-nm peaks. Thus imaging down to the single atom level is feasible because  $10^4$  higher laser intensity can

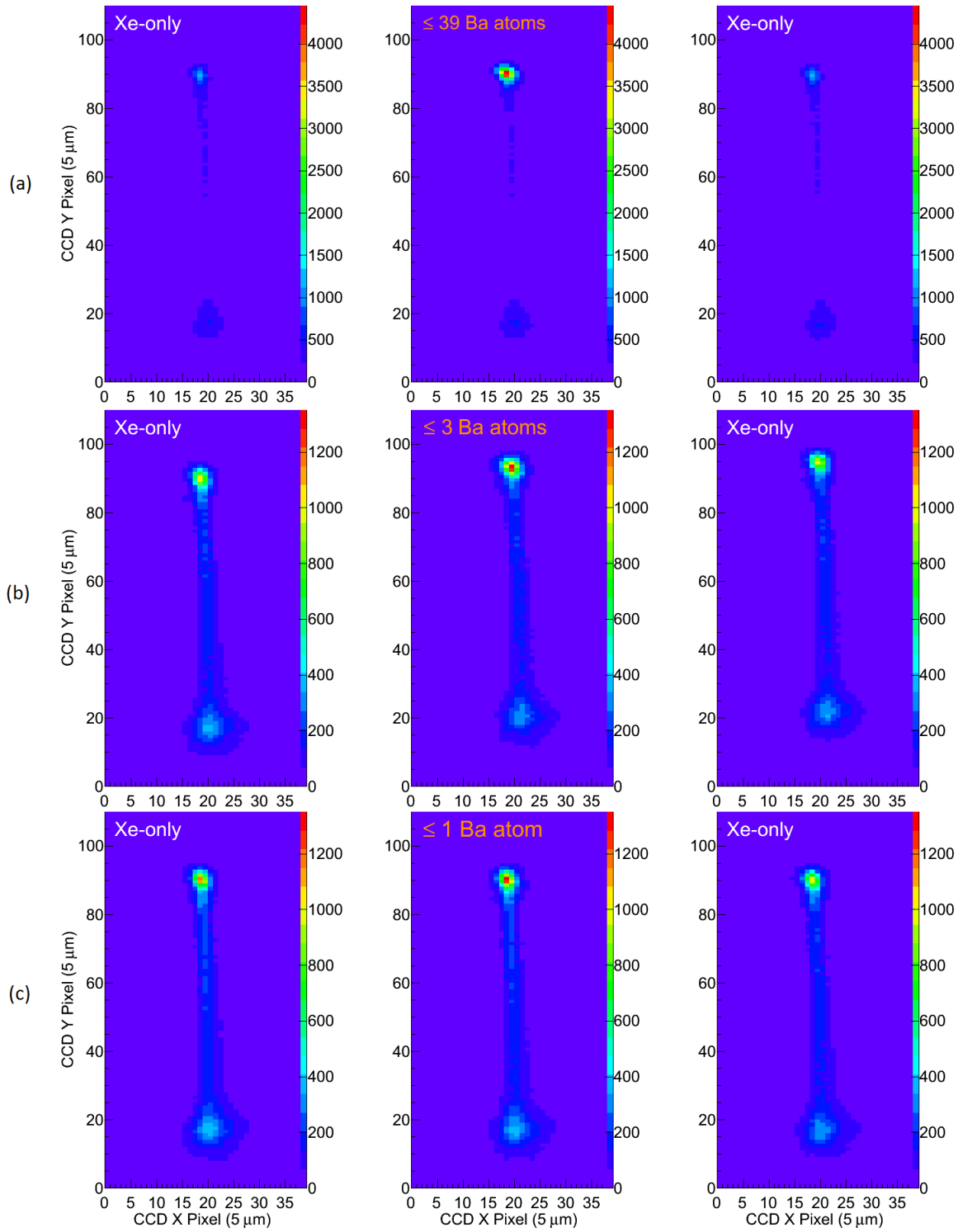


FIGURE 6.2. Raw images through a 620-nm band-pass filter of three  $\text{Ba}^+$  deposits yielding (a)  $\leq 39$ , (b)  $\leq 3$ , and (c)  $\leq 1$   $\text{Ba}$  atoms, with their preceding and succeeding Xe-only deposits. The samples were deposited at 50 K and observed at 11 K.

be used. Raw images of Ba atoms in  $\text{Ba}^+$  deposits and their preceding and succeeding Xe-only deposits are shown in Fig. 6.2 for deposits of (a)  $\leq 39$  ( $\leq 183$ ), (b)  $\leq 3$  ( $\leq 14$ ), and (c)  $\leq 1$  ( $\leq 5$ ) instantaneous (total) number of Ba atoms exposed (see Sec. 3.1.5 for calibration of ion deposit). The exposure time is 60 s with around 0.24 mW ( $10^4 \times$  that used in Fig. 6.1) of 570 nm excitation focused to  $w_x \times w_y = 2.06 \mu\text{m} \times 2.66 \mu\text{m}$  with the aspherical laser focusing lens and astigmatism compensator (Sec. 3.4). In this case the factor between total and instantaneously exposed atoms is 4.7 (Sec. 3.7). The signal is distinguishable from the background by eye, even with an instantaneous number of exposed atoms at the 1-atom level.

To determine the total 619-nm fluorescence signal level, counts were summed from of a 3-pixel $\times$ 3-pixel ( $15\mu\text{m} \times 15\mu\text{m}$ ) region centered on the laser spot in the image. The background was determined by averaging the 3-pixel $\times$ 3-pixel sum of the Xe-only runs before and after each  $\text{Ba}^+$  run. The signal and background were scaled to laser power, and then the background was subtracted.

The integrated 619-nm fluorescence signal is plotted vs. instantaneous number of ions (upper limit on atoms) exposed in Fig. 6.3 for many deposits in two experiments with two different laser focusing lenses: (a) asphere with astigmatism compensation, and (b) bi-convex lens. The laser and CCD exposures were (a) 60 s with 0.24 mW laser power, and (b) 3 s with 2 mW laser power, respectively. In (b), the open circles correspond to runs where the background was less certain due to movement of the laser on the sapphire window, which was correlated with variation in the surface background. The two experiments demonstrate a linear relationship between the signal and the number of ions exposed over more than two orders of magnitude. This is important evidence that the 619-nm peak arises from Ba

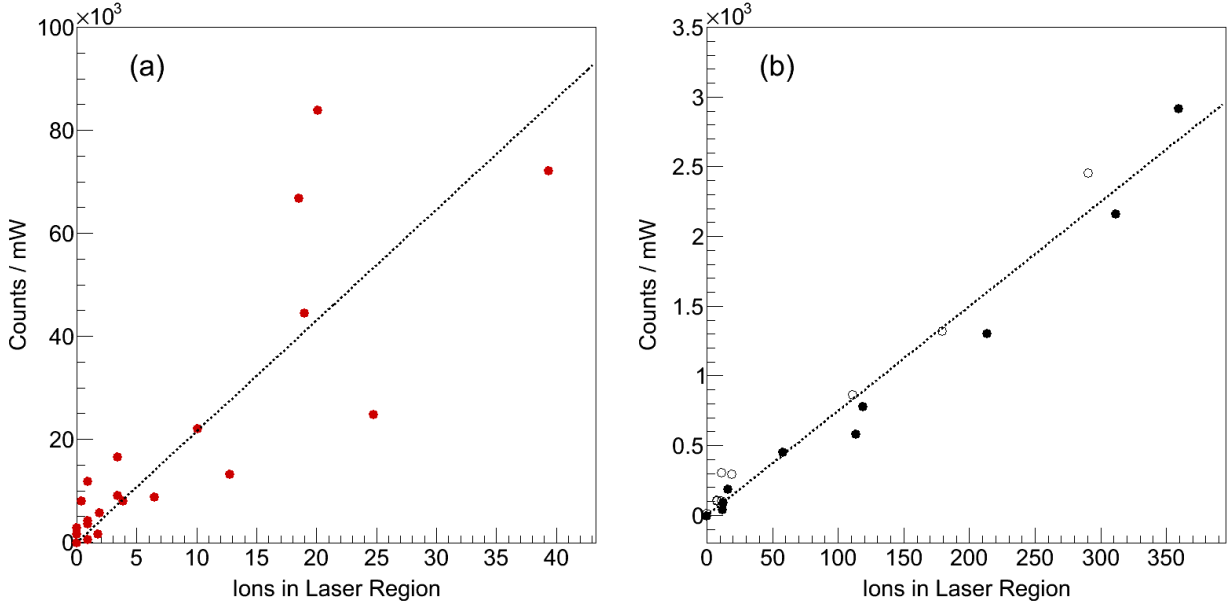


FIGURE 6.3. Total 619-nm signal, scaled by laser power, vs. instantaneous number of  $\text{Ba}^+$  ions deposited in the focal region of a laser at 570 nm for experiments with (a) aspherical, and (b) bi-convex laser focusing lenses. The exposure times are (a) 60 s, and (b) 3 s. In (b), the open circles correspond to runs where the surface background was less certain.

atoms and not, e.g.,  $\text{Ba}_2$  molecules, which would exhibit a quadratic relationship with ions deposited. Zero-ion deposits are produced by retracting the Faraday cup for 1 s without pulsing the ion beam. The linear fit in (a), which does not include a constant value, gives a slope of about  $2200 \pm 230$  counts/mW per atom with 60-s exposures in a  $w_x \times w_y = 2.06 \mu\text{m} \times 2.66 \mu\text{m}$  laser region. The slope is lower in Fig. 6.3b due to about 5 times larger laser region and 20 times lower exposure time, however signal levels are similar between the two experiments when counts are scaled by time and laser intensity.

Images of 619-nm Ba fluorescence are shown in Fig. 6.4 for a few deposits near the linear trend line in Fig. 6.3a. In each case the image of the preceding Xe-only deposit is subtracted so that only the Ba fluorescence is seen. Clear, sharp peaks are observed from an instantaneous number of atoms all the way down to the single-atom level. This result is a significant advance beyond the sensitivity reported in [22], and a major step toward

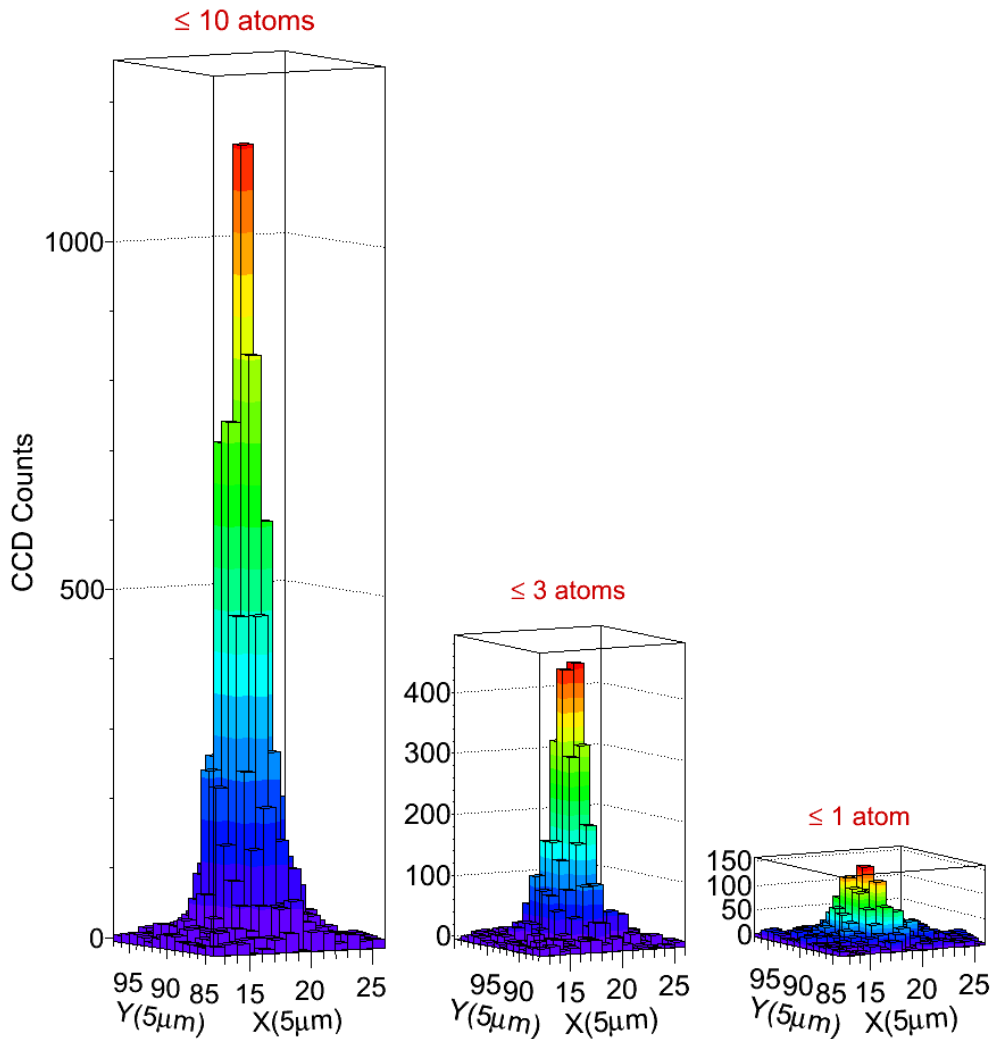


FIGURE 6.4. Subtracted images of 619-nm fluorescence in the focused laser region for runs near the linear trend line in signal vs. ions deposited. Exposures are 60 s with around 0.24 mW of 570 nm excitation focused to  $w_x \times w_y = 2.06 \mu\text{m} \times 2.66 \mu\text{m}$ .

the ultimate success of Ba tagging. It is generating excitement and interest in the nEXO collaboration.

Another very significant observation is the lack of Ba fluorescence in Xe-only deposits made after evaporating the matrix, even for large Ba<sup>+</sup> deposits. This is demonstrated in Fig. 6.2, where no Ba fluorescence is present in the Xe-only runs following each of the deposits. This is shown further for a  $\leq 61,000$  Ba atom deposit in Fig. 6.5. The lack of a history

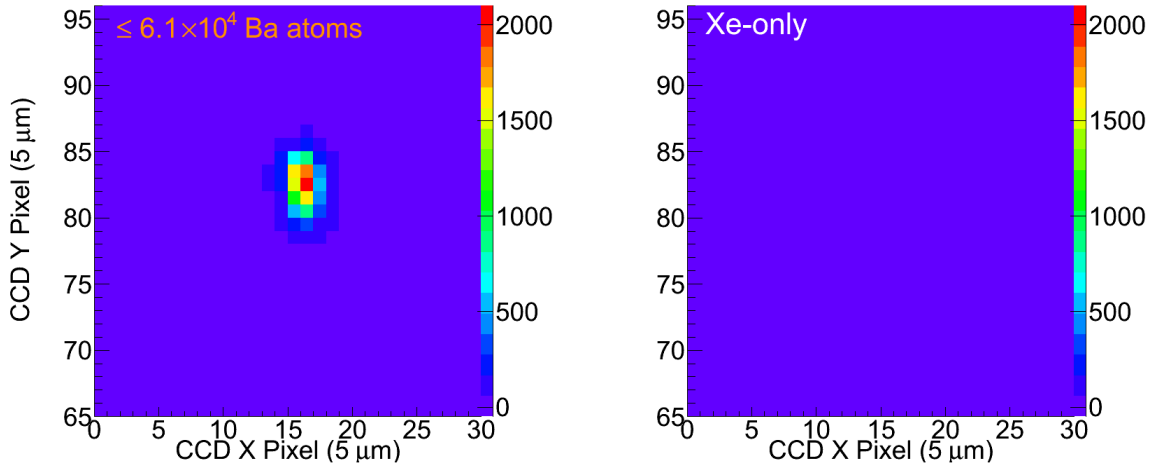


FIGURE 6.5. Raw images through a 620-nm band-pass filter of a  $\text{Ba}^+$  deposit yielding  $\leq 6.1 \times 10^4$  Ba atoms, with its succeeding Xe-only deposit. Exposures are 0.5 s with 0.6 mW of 572 nm excitation focused with the aspherical lens and astigmatism compensator.

effect after evaporation of each sample is important for the implementation of this method of Ba tagging on a probe in nEXO. Once a Ba daughter has been identified in SXe on a cold probe, the sample can be evaporated without the Ba atom or ion giving false positives in Ba tagging procedures on subsequent  $0\nu\beta\beta$  candidate events.

## CHAPTER 7

# CONCLUSIONS

Imaging of Ba atoms in SXe at the single-atom level has been demonstrated with deposits of small numbers of  $\text{Ba}^+$  ions in a focused laser region. The 619-nm fluorescence peak, which has minimal bleaching, was used with around 0.2 mW of 570-nm excitation, over tens of seconds of exposure. This achievement is a major step toward the ability to tag Ba daughters in the nEXO neutrinoless double beta decay experiment. Ba tagging is perhaps the only experimental method on the horizon with sensitivity to Majorana neutrino mass below 10 meV.

Studies of the spectroscopy of Ba and  $\text{Ba}^+$  in SXe are presented and have been published recently in [22]. Thermal history effects and temperature dependence of fluorescence have been discussed. Bleaching of the fluorescence was studied at various excitation wavelengths and intensities, with comparison to a model of the rate equations. These studies determined optimum conditions for single-atom level imaging with the 619-nm fluorescence, as well as in imaging the 577- and 591-nm fluorescence at the  $\sim 10^3$ -atom level. Blue excitation of  $\text{Ba}^+$  deposits in SXe has revealed several newly reported emission peaks which are candidates for matrix-isolated  $\text{Ba}^+$  ions.

### 7.1. FUTURE WORK

The next step in the demonstration of Ba tagging in SXe will be imaging separate Ba atoms in SXe by a raster of the focused laser beam across an area of the sample. To achieve good scanned images, overcoming the surface background emission is the first priority. In first attempts at scanned images, pre-bleaching of the sapphire window has been done with

a raster pattern, though further study is needed to perfect the procedure. Ba emission could possibly be separated from background by different emission lifetimes, as is done in single molecule studies [47]. Fluorescence lifetimes of the 619-nm signal vs. the background using a  $< 1$  ns pulsed laser and a photomultiplier tube for fast detection could be explored, in order to determine whether a fluorescence time gating technique may remove background. One exciting outcome of the atom counting inherent in scanned images is that they will provide the first measurement of the percentage of deposited  $\text{Ba}^+$  ions that neutralize in the SXe matrix and are visible as Ba atoms via the 619-nm fluorescence.

To improve Ba tagging efficiency, it would be good to be able to image Ba atoms in other matrix sites. Exploration of re-pumping wavelengths for the 577- and 591-nm peaks may be done using tunable lasers in the infrared. The ability to count atoms emitting with these different wavelengths would be very valuable. It is not yet known if daughter  $\text{Ba}^+$  ions captured from LXe will remain as  $\text{Ba}^+$  or neutralize to Ba in SXe. The ability to count  $\text{Ba}^+$  ions is also important and will be pursued by continuing study of the candidate  $\text{Ba}^+$  emission peaks with blue excitation.

Plans for ultimate demonstrations of Ba tagging in SXe include grabbing out of LXe on cold probes. Construction of an apparatus is occurring simultaneously in our laboratory, in which a cold probe can be lowered into a LXe cell. Initial tests of freezing LXe on Joule-Thompson probes have been successful.  $\text{Ba}^+$  can be produced by laser ablation of Ba metal and drifted into the LXe, a process demonstrated in [20], and onto the cold probe by electrodes. In order to reach temperatures around 10 K, where the Ba fluorescence is strong, the probe can be raised to an isolated pumping region for further cooling and observation.

---

The next breakthrough in particle/nuclear physics may lie in the discovery of Majorana neutrino mass, and the search for  $0\nu\beta\beta$  is of key importance in this discovery. Extreme sensitivity in experimental technique is required, and ingenious techniques, including Ba tagging, must be invented and demonstrated to reduce competing backgrounds to zero over operating times of many years. It is expected that unprecedented sensitivity in neutrinoless double beta decay will be reached in the second phase of nEXO, sufficient to cover the complete possibilities for the inverted neutrino mass hierarchy. Based on progress that has been made, including this work, the future of Ba tagging is bright.

## BIBLIOGRAPHY

- [1] C.D. Ellis and W.A. Wooster, “The average energy of disintegration of radium e,” *Proceedings of the Royal Society (London)* **A117** 109-123 (1927).
- [2] F. Wilson, *American Journal of Physics* **36**, 12 (1968).
- [3] Y. Fukuda *et al.* (Super-Kamiokande Collaboration), *Phys. Rev. Lett.* **81** 1562 (1998).
- [4] S.T. Petcov, W. Rodejohann, T. Shindou, Y. Takanishi, *Nuclear Physics B* **739**, 208-233 (2006).
- [5] M. Danilov *et al.*, *Physics Letters B* **480**, 12-18 (2000).
- [6] K.A. Olive *et al.* (Particle Data Group), “14. Neutrino Mass, Mixing, and Oscillations,” *Chin. Phys. C* **38**, 090001 (2014) (<http://pdg.lbl.gov>)
- [7] P.A.R. Ade *et al.* (Planck Collaboration), *Astronomy and Astrophys.* **571**, A16 (2014).
- [8] N. Steinbrink *et al.*, *New Journal of Physics* **15**, 113020 (2013).
- [9] J. Albert *et al.* (EXO-200 Collaboration), *Phys. Rev. C* **89**, 015502 (2014).
- [10] M. Moe, *Phys. Rev. C* **44**, R931 (1991).
- [11] M. Auger *et al.*, *JINST* **7**, P05010 (2012).
- [12] R. Nielson *et al.*, *Nuclear Instruments and Methods in Physics Research A* **608**, 68 (2009).
- [13] J. Albert *et al.* (EXO-200 Collaboration), *Phys. Rev. C* **92**, 045504 (2015).
- [14] E. Conti *et al.*, *Phys. Rev. B* **68**, 054201 (2003).
- [15] M. Auger *et al.*, *Phys. Rev. Lett.* **109**, 032505 (2012).
- [16] J. Albert *et al.* (EXO-200 Collaboration), *Nature* **510**, 229 (2014).
- [17] A. Gando *et al.* (KamLAND-Zen Collaboration), *Phys. Rev. Lett.* **110**, 062502 (2013).
- [18] N. Ackerman *et al.* (EXO-200 Collaboration), *Phys. Rev. Lett.* **107**, 212501 (2011).
- [19] A. Gando *et al.* (KamLAND-Zen Collaboration), *Phys. Rev. C* **85**, 045504 (2012).

- [20] K. Hall, *In-situ Laser Tagging of Barium Ions in Liquid Xenon for the EXO Experiment*. Colorado State University Thesis/Dissertation (2012).
- [21] K. Twelker *et al.*, *Review of Scientific Instruments* **85**, 095114 (2014).
- [22] B. Mong *et al.*, *Phys. Rev. A* **91**, 022505 (2015).
- [23] J. J. Curry, *Journal of Physical and Chemical Reference Data* **33**, 725 (2004).
- [24] J. Migdalek and W. E. Baylis, *Phys. Rev. A* **42**, 6897 (1990).
- [25] V. A. Dzuba and J. S. M. Ginges, *Phys. Rev. A* **73**, 032503 (2006).
- [26] A. Mohanty *et al.*, *Hyperfine Interactions* **233**, 113-119 (2015).
- [27] N. Yu, W. Nagourney, H. Dehmelt, *Phys. Rev. Lett.* **78**, 26 (1997).
- [28] S. De, U. Dammalapati, K. Jungmann, L. Willmann, *Phys. Rev. A* **79**, 041402(R) (2009).
- [29] W. Neuhauser, M. Hohenstatt, P. Toschek, and H. Dehmelt, *Phys. Rev. Lett.* **41**, 233 (1978).
- [30] M. Green *et al.*, *Phys. Rev. A* **76**, 023404 (2007).
- [31] E. Whittle, D. Dows, G. Pimentel, *The Journal of Chemical Physics* **22**, 1943 (1954).
- [32] C. Crepin-Gilbert and A. Tramer, *Int. Reviews in Physical Chemistry* **18**, No. 4, 485-556 (1999).
- [33] H. A. Jahn and E. Teller, *Proceedings of the Royal Society of London A* **161**, 220-235 (1937).
- [34] M. Ryan *et al.*, *J. Phys. Chem. A* **114**, 3011-3024 (2010).
- [35] Now Beam Imaging Solutions, 1610 Pace St., Unit 900, #303, Longmont, CO 80504.
- [36] L. W  hlin, “The Colutron, a Zero Deflection Isotope Separator,” *Nuclear Instruments and Methods* **27** 55-60 (1964).

- [37] S. Cook, *Detection of Small Numbers of Barium Ions Implanted in Solid Xenon for the EXO Experiment*. Colorado State Universtiy Thesis/Dissertation (2012).
- [38] B. Mong, *Barium Tagging in Solid Xenon for the EXO Experiment*. Colorado State Universtiy Thesis/Dissertation (2011).
- [39] A. C. Sinnock, *J. Phys. C: Solid St. Phys.* **13**, 2375-91 (1980).
- [40] D. Fairbank (private communication, 2015).
- [41] J.-P. Tache, *Applied Optics* **26**, 429 (1987).
- [42] Measured by Princeton Instruments (New Jersey) prior to shipment (2004).
- [43] D. F. Nelson, M. D. Sturge, *Physical Review* **137**, 4A (1965).
- [44] C. Guguschev, J. Gotze, M. Gobbels, *American Mineralogist* **95**, 449-455 (2010).
- [45] R. A. Ford, O. F. Hill, *Spectrochimica Acta* **16**, 493-496 (1960).
- [46] D. S. McClure, *Solid State Phys.* **9**, 399-525 (1959).
- [47] W. Patrick Ambrose *et al.*, *Chem. Rev.* **99**, 2929-2956 (1999).